Use of Time Domain Capacitance Spectroscopy in the Study of Tunneling into Two-Dimensional GaAs/AlGaAs Heterostructures with an in-Plane Magnetic Field

by

Aleem Siddiqui

Submitted to the Department of Electrical Engineering and Computer Science
in partial fulfillment of the requirements for the degree of

Master of Engineering

at the

MASSACHUSETTS INSTITUTE OF TECHNOLOGY

February 2003

© Aleem Siddiqui, MMIII. All rights reserved.

The author hereby grants to MIT permission to reproduce and distribute publicly paper and electronic copies of this thesis document in whole or in part.

MASSACHUSETTS INSTITUTE
OF TECHNOLOGY
JUL 3 0 2003
LIBRARIES

Author ....
Department of Electrical Engineering and Computer Science
February 3, 2001

Certified by ....
Raymond Ashoori
Professor
Thesis Supervisor

Accepted by .
Arthur C. Smith
Chairman, Department Committee on Graduate Theses

BARKER

Use of Time Domain Capacitance Spectroscopy in the Study of Tunneling into Two-Dimensional GaAs/AlGaAs Heterostructures with an in-Plane Magnetic Field

by

Aleem Siddiqui

Submitted to the Department of Electrical Engineering and Computer Science
on February 3, 2001, in partial fulfillment of the
requirements for the degree of
Master of Engineering

Abstract

This thesis is concerned with the use of the technique of Time Domain Capacitance Spectroscopy (TDCS) to study the effects of tunneling between a two-dimensional electronic system and a three-dimensional contact in the presence and absence of an in-plane field. We use the TDCS technique to attempt to measure the tunneling process in an equilibrium and an out of equilibrium configuration. We are able to present data which is successfully described by equilibrium tunneling for the zero-field and in-plane field situations. We were also successful in measuring out of equilibrium behavior in the zero-field regime. However, more experimental work needs to be done for the out of equilibrium tunneling in the in-plane field regime in order for the results to be satisfactory.

We also present theoretical models to describe zero-field tunneling and in-plane field equilibrium tunneling. Furthermore, we extend this model to include the effects associated with out of equilibrium tunneling and in the case of in-plane field tunneling present simulated results.

Thesis Supervisor: Raymond Ashoori
Title: Professor

Acknowledgments

There are many people to whom I owe gratitude for their help through the course of this experiment. I would like to thank my advisor Prof. Raymond Ashoori, Oliver Dial, Gary Steele, and Dmitri Pouchine for their tireless efforts and advice.

Contents

1 **Introduction[1]** 15

1.1 Introduction to Two-Dimensional Electronic Systems 16

1.2 Thermodynamic and Single-Particle Density of States 18

1.3 Single-Particle DOS and Double Pulsing Current[2] 19

2 **Overview of Time Domain Capacitance Spectroscopy[3]** 23

2.1 Overview of TDCS 23

2.2 Sample Construction 26

2.3 Capacitance Bridge Circuit 26

2.3.1 Setting up Voltage Sequence Across Sample 28

2.3.2 Sensing Circuit 31

2.3.3 Experimental Setup 34

2.4 Sample Holder 37

2.5 Typical Results: Shubnakov De Haas Oscillations 37

3 **Results for Zero-Field Tunneing** 45

3.1 Zero Field Momentum Selection 45

3.2 Equilibrium Tunneling 47

3.3 Out of Equilibrium Tunneling 49

3.3.1 Positive Excitations 50

3.3.2 Negative Excitations 52

3.4 Data and Interpretation 54

4 **Results for In-Plane Field Tunneling** **59**
4.1 Basic Theoretical Picture 59
4.2 Analytical Presentation: Dispersion Relations 65
4.3 Energy Contours in Momentum Space 69
4.4 Effect of varying field and density on tunneling conductance 72
4.5 Effects of Tunneling out of Equilibrium 74
4.6 Tunneling Conductance as a function of Excitation Height 78
4.7 Experimental Results 78

5 **Conclusion and Future Work** **89**

A **Pulse Shaper** **91**
A.1 Pulse-Shaper as the New Generator of Excitations 91
A.2 Explanation of the Circuit Implementation 93
A.3 Incorporation of the HP11713A Variable Attenuators 95
A.4 Printed Circuit Board 99

List of Figures

1-1 Band structure of two systems of different chemical potentials separated by a thin tunneling barrier. (Figure taken from Chan [2].) . . . 19

1-2 Tunneling in the presence of an in-plane magnetic field. The upper figure is a schematic representation in energy and the lower figure is a schematic representation in momentum. 21

2-1 Tunneling experiment setup with contact made to the 2DEG. (Figure taken from Chan [2].) 24

2-2 Tunneling experiment setup for TDCS. (Figure taken from Chan [2].) 25

2-3 a) Physical sample structure. A top electrode is made to the cap layer and a bottom electrode is made to the substrate. b) Band diagram of sample. c) Circuit Model of sample. (Figure taken from Chan [2].) . . 27

2-4 Effect of a voltage bias on the Fermi level of the well. Inset a) shows the system in equilibrium and the well has a Fermi energy of E_o. Inset b) shows that when a bias V_{gate} is applied, the Fermi level of the well increases by ΔU_w rather than eV_{gate}. As shown above, $\Delta U_w = \Delta\sigma_w/g$ where $\Delta\sigma_w$ is the charge increase and g is the density of states. The effect of a finite density of states g is that the bottom electrode is not perfectly screened from the top electrode. 29

2-5 Detailed evolution of the sample band structure during a step excitation. (Figure taken from Chan [2].) 30

2-6 Sensing circuit used in the experiment. (Figure taken from Chan [2].) 32

2-7 Typical input and output wave forms of the sensing circuit. 33

2-8 Data for the low frequency capacitance of the sample revealing the Landau levels in the DOS for a 2DEG in a perpendicular magnetic field. 35

2-9 Complete experimental setup. (Figure taken from Chan [2].) 36

2-10 Photograph of the sample, sensing circuit, and hall sensor in the sample space mount. 38

2-11 Explanatory diagram of the elements in the sample mount. 39

2-12 The gate of the transistor must be aligned in the plane of the field so that gain of the transistor remains independent of the field. 40

2-13 Typical output waveform. 41

2-14 Low frequency capacitance as a function of perpendicular field. 42

2-15 Low frequency capacitance as a function of 1/B indicating the conductivity is periodic in 1/B. This is a signature of Shubnakov De Hass oscillations. 43

3-1 Zero field tunneling process in energy and momentum spaces. The insets show that as the bias is increased the tunneling circle in the contact is drawn toward the origin. 46

3-2 Beyond the critical bias momentum conservation no longer holds. Tunneling occurs via scattering off impurities and the tunneling conductance falls off as bias is increased. 47

3-3 Inset a) shows how the cross section of interest in the 3D momentum space of the contact shits out during a positive excitation. Tunneling then proceeds from the well to the contact as indicated in the diagram. Inset b) shows the critical point where momentum is still able to be conserved. 51

3-4 Inset a) shows how the cross section of interest in the 3D momentum space of the contact shits inward during a negative excitation. Tunneling then proceeds from the contact to the well as indicated in the diagram. Inset b) shows the critical point where momentum is still able to be conserved. 53

3-5 Beyond the critical point for negative excitation, tunneling process cannot conserve momentum. As indicated in the figure, processes that conserve energy require tunneling from a sphere of smaller radius in the contact to a circle of larger radius in the well. Thus no projection of the k-vector on the sphere can overlap with a k-vector on the disk and momentum cannot be conserved. 54

3-6 Equilibrium tunneling data. 55

3-7 Tunneling out of equilibrium data. The excitation is applied to the substrate of the sample and the excitation is applied across the entire sample structure. The curve at the base of the two arrows pointing away from the horizontal axis correspond to the sample biased in depletion. The arrows indicate curves corresponding to increasing well densities. 56

4-1 Effect of an in-plane field on tunneling conductance as a function of well density. (Figure taken from Lebens [3].) 60

4-2 Effect of an in-plane field on tunneling conductance. Oscillations are seen. (Figure taken from Snell [6].) 60

4-3 Dependence of the frequency of the two sets of oscillations on well density. (Figure taken from Snell [6].) 61

4-4 Coordinate system used. z is in the direction of the field, x is along the growth direction of the sample, and y is in the sample plane but perpendicular to the field. 62

4-5 Energy vs. orbit center, x_o, dispersion relation. (Figure taken from Lebens [3].) 63

4-6 Calculations for the energy of the well and contact at x'_o. Only the first sub-band in the well is occupied so there is only one relevant energy for the well while there may be multiple levels for the contact. 64

4-7 Analytical solution presented in normalize coordinates. The vertical axis is normalized energy ϵ, and the horizontal axis is κ_y, which is proportional to orbit center x_o. (Figure taken from Snell [6].) 67

4-8 Constant energy contours for the electrons in the well for different biases, and for the electrons in the contact for different Landau levels. The horizontal axis κ_y is proportional to orbit center position, x_o, and the vertical is κ_z, where z is along the field direction. 71

4-9 The arrows indicate the effect of sweeping the in-plane field in the momentum contour space. The horizontal axis κ_y is proportional to orbit center position, x_o, and the vertical is κ_z, where z is along the field direction. 73

4-10 Inset a) indicates the band structure of the sample at equilibrium, inset b) shows the sample after a positive excitation, and inset b) shows the sample after a negative excitation. The upper bound and lower bound states of interest are shown. 74

4-11 Response to a positive excitation in momentum space. The lines formed by the + signs were generated by simulation and indicated the momentum of electrons that tunnel from the well to the contact with the band of energies made available by the excitation. In other words, electrons in states located on the vertical line represent all the allowed tunneling transitions between the well and the contact. Each point indicated by a + was computed by finding the intersection between a circular contour (well) and a set of U-shaped contours (contact) for the energies between the lower bound and upper bound states indicated in Figure 4-10 b. See text for further explanation of the figure. 76

4-12 Response to a negative excitation in momentum space. The lines formed by the + signs where generated by simulation and indicated the momentum of electrons that tunnel from the contact to the well with the band of energies made available by the excitation. In other words, electrons in states located on the vertical line represent all the allowed tunneling transitions between the well and the contact. Each point indicated by a + was computed by finding the intersection between a circular contour (well) and a set of U-shaped contours (contact) for the energies between the lower bound and upper bound states indicated in Figure 4-10 c. See text for further explanation of the figure. 79

4-13 There is no overlap between contours of the well and contact as no tunneling occurs. 80

4-14 Large positive excitations open up overlap to allow tunneling to occur. Electrons in states located on the vertical line represent all allowed tunneling transitions between the well and the contact. 81

4-15 Large negative excitations open up overlap to allow tunneling to occur. Electrons in states located on the vertical line represent all allowed tunneling transitions between the well and the contact. 82

4-16 Relative conductance vs. field (Tesla) for different biases. The biases across the sample are shown in the legend. The excitation amplitude across the sample is 120mV. The arrow shows how the curve changes as we go from depletion (-6.52mV) to accumulation (6.52mV). 84

4-17 Relative conductance vs. bias (V) for different fields and from the data taken from Figure 4-16. The fields are indicated in the figure and are reported in Tesla. The excitation amplitude across the sample is 120mV. The arrow shows how the curve changes as we vary the field from 0 Tesla to 5 Tesla. 85

4-18 Relative conductance vs. bias (V) for different fields. The excitation height applied across the sample is 10mV. The steps in the above data are due to bit errors in the voltage box applying the bias voltage. The error was fixed immediately after this data was collected and so doesn't appear for subsequent data. In previous data we fitted a line to the initial points of the data to extract the initial slope. In this data we fitted least squared exponentials and thus greatly improved the fits as can be seen by comparing the noise in the above data to that of Figure 4-16. 86

4-19 Relative conductance vs. bias (V) for different fields. The excitation height across the sample is 2mV. A second bulge is observed in the data. 87

4-20 Relative conductance vs. bias (V) for different excitation heights. The excitation heights and pulse directions are indicated in the figure. . . 88

A-1 Schematic for the pulse generation for the standard capacitor excitation. 92

A-2 Schematic for the pulse generation for the sample excitation. 92

A-3 Schematic for the Pulse Shaper circuit used to adjust pulse heights. . 96

A-4 Schematic for the printed circuit board of the pulse shaper. 97

A-5 Schematic for the printed circuit board of the pulse shaper. 98

Chapter 1

Introduction[1]

The advent of semiconductor technology and the development of the MOS field effect transistor has had a significant impact on the on the field of condensed matter physics. In particular the MOS devices have made possible the study of previously unattainable systems and enabled experimental verification of existing theories. The type of two-dimensional systems associated with MOS technology have lead to the demonstration of a wide range of notable effects and phenomena including the acclaimed integer and fractional Hall Effect (QHE), the proposed existence of a Wigner Crystal, and the recently discovered two-dimensional metal insulator transition (MIT).

Although there has been a great deal of success, studies of transport properties in two-dimension electronic systems (2DES) have, until recently, suffered from a number of limitations. As will be discussed, the most significant of these is the need in traditional transport measurements to form a direct ohmic contact to the underlining two-dimensional electron gas (2DEG). This limits sets a limit on the overall experimental sensitivity that is capped by the in-plane conductivity of the 2DEG and the ohmic contact. In this thesis we discuss and apply a measurement technique developed in the works of Chan [2] that provides an alternate to the traditional scheme and overcomes this limitation. The technique, coined Time Domain Capacitance Spectroscopy (TDCS), circumvents the ohmic contacts, but employing remote capacitive sensing of all tunneling phenomena. The merit of the technique was proven by Chan's measurements on Skirmion tunneling events, and in this thesis we wish to extend TDCS to measurement of the in-plane field dependence of the tunneling conductance.

---

[1] Much of the information in this chapter was taken from Chan's thesis [2] since the Double Pulsing Experiment builds off of Chan's work.

Although the main body of work on tunneling in 2DES has focused on the effect of perpendicular field, the study of in-plane, parallel field is equally as fascinating and important. From the point of view of energy and momentum conservation, the application of an in-plane field effectively provides a means to control the final momentum states of tunneling events and, in a sense, enables us to probe electronic states of a particular energy and momentum. The additional degree of control on tunneling events may prove useful in unraveling process as a function of momentum as well as energy. In this work we are concerned with presenting the basic tunneling process of in-plane tunneling form the point of view of conservation of energy and momentum as well as presenting preliminary results.

This thesis is organized in the following manner. The rest of this chapter present an overview of the basic physical concepts of the 2DEG system. The next chapter provides an overview of the TDCS technique and discusses the technique in the context on in-plane measurements. In the third chapter we present a theoretical picture of in-plane tunneling and present preliminary results. And in the final chapter we conclude with a discuss of the future prospects of the technique.

1.1 Introduction to Two-Dimensional Electronic Systems

Two-dimensional electronic systems (2DES) are typically formed within GaAs/AlGaAs quantum well heterostructures grown via molecular beam epitaxy (MBE). Band mismatch between intrinsic GaAs and AlGaAs causes band bending at layer interfaces, and thus draws ionized electrons from doped regions into accumulation into the defined well structure. In this way a 2DEG can be achieved.

For our structures, typical well parameters include densities of $1.0 \times 10^{11} cm^{-2}$, and thicknesses of 150Å which results in a Fermi energy of $3.6 meV$ and an interband separation of $50 meV$. This places the Fermi level well below the second sub-band, and since we operate at less than $1K$, thermal excitations into the second sub-band can be ignored. Thus our samples can be treated as truly two-dimensional without worrying about complexities arising from second sub-band occupation.

In the absence of a magnetic field the density of states (DOS) of the 2DES is constant, but when a magnetic field is applied perpendicular to the 2DES the density of states becomes highly degenerate. The magnetic field confines the 2DES laterally and, without disorder, causes the DOS to consist of a series of delta functions in energy called *Landau levels* which correspond to classical orbiting states. Disorder within the system causes the Landau spikes in the DOS to be broaden. Thus the Landau spikes take on particular shapes. Electrons will fill all Landau levels for energy less then the Fermi energy, and the number of filled Landau levels is referred to as the filling factor ν. The filling factor ν can be modified in two ways: by changing the Fermi level or changing the magnetic field. By increasing the Fermi level one can increase the filling factor ν, and by increasing the magnetic field one can decrease the filling factor ν since the separation between Landau levels is proportional to the magnetic field.

Tunneling in the presence of a perpendicular magnetic field has been the main focus research in 2DES. In this thesis, however, we are interested with the effect that an in-plane or parallel field has on the tunneling conductance between a 2DEG and a three-dimensional contact. We are thus concerned with the effect that parallel fields have on electrons in the quantum well and contact.

When a magnetic field is applied parallel to the well, the electrons are classically pressed to the left and right walls do to the Lorenz force. In quantum mechanics we visualize this as a shifting a gauge potential, where a larger shift corresponds to electrons with greater transverse momentum and which are more tightly pressed. In a three dimensional contact, while bulk states occupy Landau levels, interfacial states at the contact edge are confined by the effect of the edge and gauge potential and correspond to classical skipping orbits.

Tunneling occurs from pressed two-dimensional states of the well and the skipping orbitals of the contact and because of the Lorenz force depends on electron velocity, tunneling processes from the 2DES to the 3D contact must conserve both momentum and energy. In the scope of this thesis, it is our aim to discuss the details of the tunneling mechanism based on the conservation rules and to present data representing our attempt to measure the process.

1.2 Thermodynamic and Single-Particle Density of States

As mentioned before the chosen experimental technique to study in-plane tunneling is Time Domain Capacitance Spectroscopy (TDCS). The technique of TDCS involves rapidly exciting a sample and recording the resulting transients to equilibrium. As such, the transients involved in TDCS contain observations of out of equilibrium phenomena on the short time scale and equilibrium phenomena on the long time scale. Thus, TDCS provides a window into the full time evolution of tunneling processes within the sample.

Tunneling measurements are naturally designed to probe the density of states (DOS) of electronic systems. Thus, at this point it is useful to distinguish between the thermodynamic DOS and the single-particle DOS. The thermodynamic DOS, $\partial N \partial \mu$, is the change in particle density N for a change in chemical potential μ after sufficient time has elapsed so that the system can equilibrate and is associated with long time scales in TDCS. The single-particle DOS, however, is relevant when the DOS is measured on fast time scales. Thus, when injecting current electrons across a tunneling barrier, for example, the single-particle DOS is the relevant DOS.

In the TDCS experiments we are primarily concerned with the single-particle DOS as will be shown in the next section. As the discussion of TDCS proceeds, it is important to keep in this in mind the distinction between the equilibrium and out of

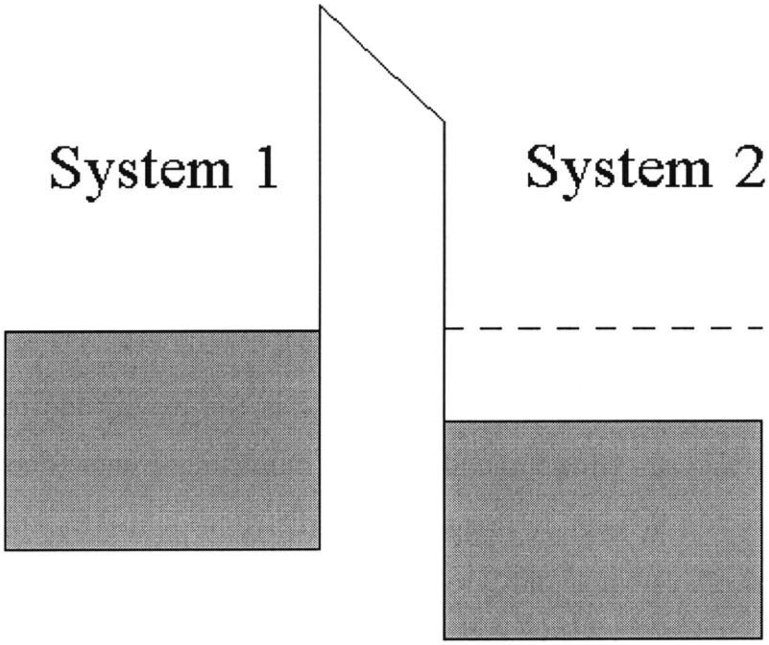

Figure 1-1: Band structure of two systems of different chemical potentials separated by a thin tunneling barrier. (Figure taken from Chan [2].)

equilibrium situations.

1.3 Single-Particle DOS and Double Pulsing Current[2]

As mentioned above, the TDCS technique is concerned with measuring the overall transient response of a tunneling sample to a rapid initial excitation. The sample generally consists of two systems seperated by a thin tunneling barrier. Immediately after such an excitation before any tunneling has occurred, the two systems are at different chemical potentials as shown in Figure 1-1.

In order for there to be a tunneling current, an electron occupying a state in system 1 must tunnel through the barrier into an unoccupied state of the same energy in system 2. Integrating over all energies we see that the following expression can adequately describe the tunneling current right after the initial excitation:

---

[2] The equations and derivations in this section are taken from Chan's thesis [2].

$$\begin{aligned}
I_{tunnel} &= I_{12} - I_{21} && (1.1)\\
&\propto -\frac{e}{\tau}\int_{-\infty}^{\infty} n_1(E-eV)f(E-eV)n_2(E)(1-f(E))dE && \\
&\quad +\frac{e}{\tau}\int_{-\infty}^{\infty} n_1(E-eV)(1-f(E-eV))n_2(E)f(E)dE && (1.2)\\
&= \frac{e}{\tau}\int_{-\infty}^{\infty} n_1(E-eV)n_2(E)[f(E)-f(E-eV)]dE && (1.3)
\end{aligned}$$

where I_{12} is the current from system 1 to 2, e is the magnitude of the electronic charge, τ is the average time interval between tunneling events (determined by the barrier thickness and height), f(E) is the Fermi distribution, $n_1(E)$ and $n_2(E)$ are the density of states of system 1 and 2 respectively.

For our experiment, system 2 corresponds to the quantum well, while system 1 corresponds to a highly doped 3D semiconductor that has a featureless DOS for small voltages. Thus we consider $n_1(E)$ to be constant over our range of interest. The differential conductance G then becomes:

$$G = \frac{dI_{tunnel}}{dV} \propto \frac{e^2}{\tau} n_1 \int_{\infty}^{\infty} n_2(E)\frac{df(E-eV)}{E}dE \qquad (1.4)$$

Considering the fact that the derivative of the Fermi function becomes an impulse as T approaches zero, we can arrive at the following expression for the differential conductance:

$$\frac{dI_{tunnel}}{dV} \propto n_2(eV) \qquad (1.5)$$

Thus, we see that the initial differential conductance is proportional to the single particle DOS for low temperatures. The utility of the TDCS technique is in its ability to measure the initial current and allow a direct probe of the single particle DOS of the quantum well as a function of energy.

This thesis builds off the notion of pulsing as a density probe in energy. In our experiment the application of an in-plane field provides us with a control on momentum as well. We can see this by considering that classically as a tunneling

Tunneling in a Transverse Field at Low Densities Allows Us to Probe the Fermi Sphere with Respect to Energy and Momentum

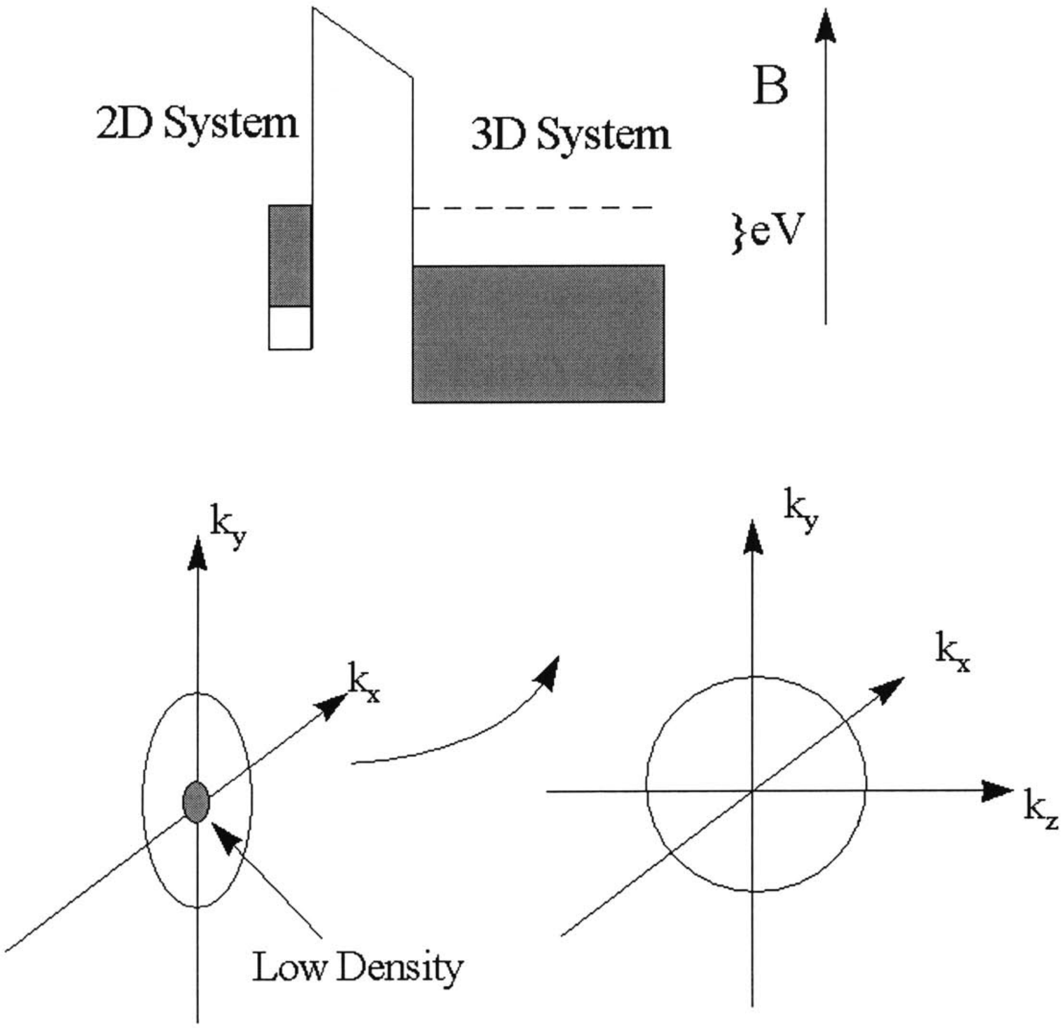
2D System
3D System
B
}eV
k_y
k_x
Low Density
k_y
k_x
k_z

Figure 1-2: Tunneling in the presence of an in-plane magnetic field. The upper figure is a schematic representation in energy and the lower figure is a schematic representation in momentum.

electron traverses the barrier, it picks up from the field a transverse momentum of $\delta k = \frac{eB}{s} * \tau$, where s is the tunneling barrier length and τ is the tunneling time constant. For a particular magnetic field we can select the momentum increase. Thus if the initial states have the same momentum we can select the final momentum of the electrons and thereby decompose the tunneling current as a function of momentum and energy. Figure 1-2 depicts a schematic representation of this.

Chapter 2

Overview of Time Domain Capacitance Spectroscopy[1]

The experimental findings of this thesis build upon of the Time Domain Capacitance Spectroscopy (TDCS) experiments performed by Chan [2]. Chan was able to use the TDCS technique to avoid limitations associated with in-plane conductivity and probe localized states which were previously difficult to measure. This opened the possibility of exploring new physics through the technique. The aim of this chapter is to describe how the TDCS and the parallel field pulsing experiment are carried out. We achieve this by discussing issues related to sample construction and sample evolution under a step excitations. This then enables us to describe the circuit scheme utilized to detect the sample response. We then discuss complexities associated with the parallel field and how alignment of the sample in the field was established. Finally we present data representing typical perpendicular field measurements to establish the applicability of the scheme.

2.1 Overview of TDCS

The main limitation of conventional tunneling experiments is that ohmic contacts are required to be made to the 2DEG as indicated in Figure 2-1. A measurement of the tunneling current across the barrier is achieved by detecting the current drawn

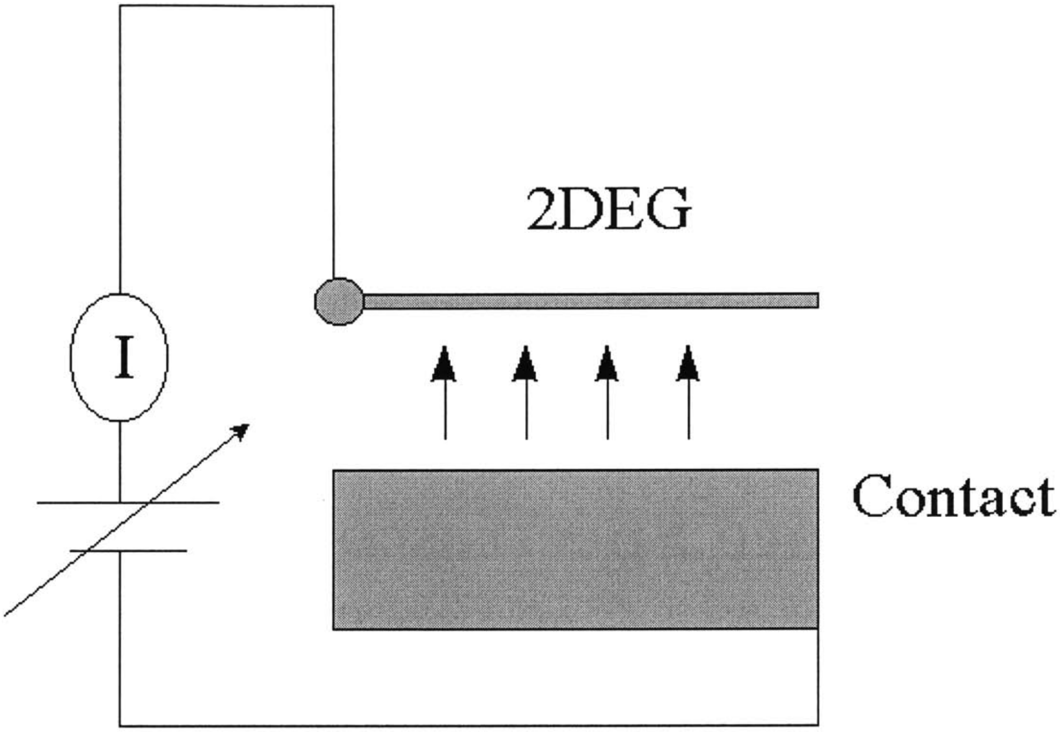

Figure 2-1: Tunneling experiment setup with contact made to the 2DEG. (Figure taken from Chan [2].)

from the contact. To ensure the reliability of the tunneling current measurement, the in plane conductivity of the 2DEG must be much greater than the tunneling conductance. Otherwise measurements would be dominated by scattering within the 2DEG and the desired tunneling conductance would not be detectable. Furthermore, the conventional scheme is limited to detection of tunneling into extended states of the 2DEG as these are the only states from which electrons can be extracted via the contact. Tunneling measurements into localized states cannot be observed.

The main feature of TDCS is that tunneling is measured without direct ohmic contacts to the 2DEG and therefore tunneling into localized states can be observed in real time. As shown in Figure 2-2, rather than having a direct ohmic contact, the 2DEG is separated from the top electrode via a blocking barrier, a thick barrier which inhibits tunneling. Tunneling events into 2DEG are sensed remotely across the

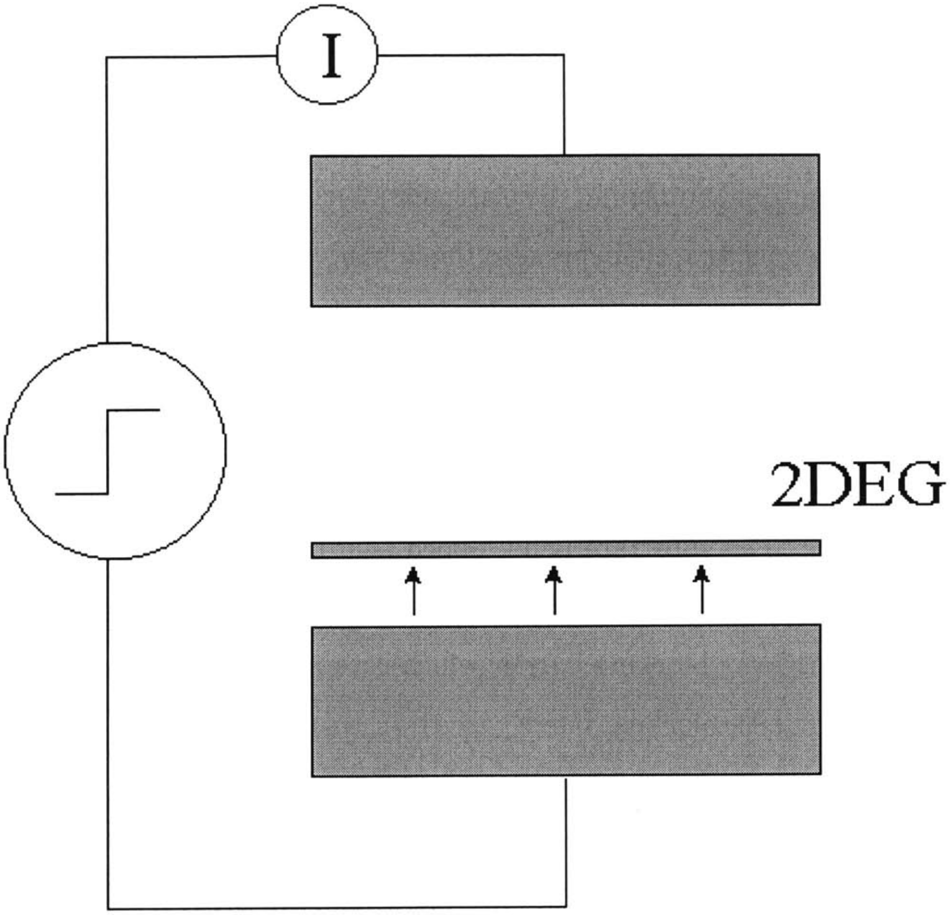

Figure 2-2: Tunneling experiment setup for TDCS. (Figure taken from Chan [2].)

blocking barrier via the electrode located on top of the sample. When electrons tunnel into the 2DEG from the bottom electrode, they push electrons in the top electrode causing a displacement current which can be sensed externally. In this manner, one can detected tunneling into the entire 2DEG even when the in-plane conductance is low. This represents a significant improvement over conventional measurement schemes.

2.2 Sample Construction

The thick blocking layer required in the TDCS technique constitutes a well defined capacitance and there is also a capacitance associated with the tunneling barrier. Thus while conventional tunneling measurements focus on resistive elements, TDCS also incorporates capacitive elements into the measurement model. In this section we introduce the sample construction and circuit model.

As shown in Figure 2-3, the sample consists of a 2DEG sandwiched between to capacitor plates. In Figure 2-3a we show the layered composition of the GaAs/AlGaAs heterostructure which was used as the sample. All the layers were grown with molecular beam epitaxy. The substrate is n+ doped. On top of this we grow an AlGaAs tunneling barrier, followed by a GaAs which defines the quantum well. The next layer is a doped AlGaAs blocking barrier which is topped off with an undoped GaAs cap layer. The AlGaAs blocking barrier is grown thick enough to prevent tunneling between the cap layer and the quantum well, and the dopants in the blocking barrier provide electrons which reside in the quantum well.

In Figure 2-3b and 2-3 c we show the band diagram and circuit model for the sample respectively. The circuit model for the sample consist of the capacitance C_{block} of the blocking barrier in series with the parallel resistance $R_{tunnel}(V)$ and capacitance C_{tunnel} of the tunneling barrier. The nonlinear tunneling resistance $R_{tunnel}(V)$ was the primary component of study in Chan's thesis [2]. In this experiment we investigate the dependence of R_{tunnel} on parallel field.

2.3 Capacitance Bridge Circuit

This study is primarily concerned with measuring the step response of a small dissipative capacitor. Thus input and output waveforms generally take on the forms shown in Figure 2-7. Furthermore, the voltage changes across the capacitor are small. Thus the capacitance bridge show in Figure 2-6 can be optimally used for signal detection. In this subsection we further discuss the sample response from the point of view of

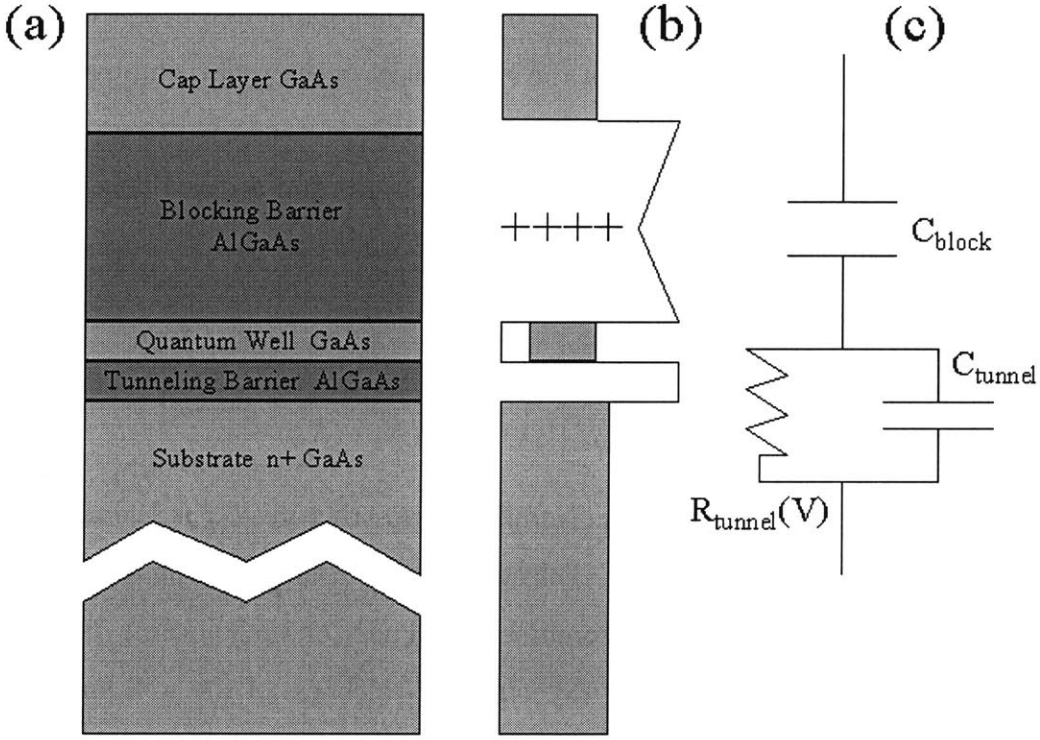
(a)
Cap Layer GaAs
Blocking Barrier AlGaAs
Quantum Well GaAs
Tunneling Barrier AlGaAs
Substrate n+ GaAs
(b)
++++
(c)
C_{block}
C_{tunnel}
$R_{tunnel}(V)$

Figure 2-3: a) Physical sample structure. A top electrode is made to the cap layer and a bottom electrode is made to the substrate. b) Band diagram of sample. c) Circuit Model of sample. (Figure taken from Chan [2].)

TDCS, and we describe the sensing circuit employed in the parallel field experiment. We begin this section by discussing how AC and DC voltages are set up across the sample.

2.3.1 Setting up Voltage Sequence Across Sample

When applying a DC or step voltage of the form in Figure 2-7 the actual voltages felt by the well are divided down by a *lever arm* factor, which is different for the DC biases and step excitations. Figure 2-4[2] depicts what happens when a DC biases is applied across the sample. Instead of the Fermi level in the well rising by the applied voltage, eV, the Fermi level rises by a fraction of that voltage. This happens because the electrons in the well have a finite density of states and are not able to perfectly screen the bottom electron from the electric field from the top electron. The scaling factor was determined by Ashoori [1] to be given by,

$$lever\ arm = \frac{U_w}{e\delta V_{gate}} = \left(\frac{-\epsilon X_w}{e^2 g X_w (X_g - X_w) + \epsilon X_w}\right) \tag{2.1}$$

where V_{gate} is the voltage across the sample heterostructure, U_w is the actual rise of the Fermi level in the well, ϵ is the dielectric constant, and e is the electron charge. Also X_g can be taken to be the combined thickness of the blocking barrier, well, and tunneling barrier, while X_w is the combined thickness of the well and tunneling barrier. This factor was calculated to be 0.03 for our sample.

The evolution of the sample to a voltage step is shown in Figure 2-5. Immediately after the excitation, the voltage is linearly dropped across the entire sample as charge has not yet had time to tunnel into the well(See Figure 2-5a). Rather than the entire excitation being felt across the well, only a fraction due to geometrical considerations is felt. Thus a voltage drop of $V_{step}\frac{X_w}{X_w+X_g}$ is thus set up across the tunneling barrier (see Figure 2-5b). The AC lever arm factor, $\frac{X_w}{X_w+X_g}$, was determined to be .3 for our sample.

As time approaches infinity, however, electrons in the contact tunnel into the quan-

---

[2] Reference to Gary Steele for providing this physical picture.

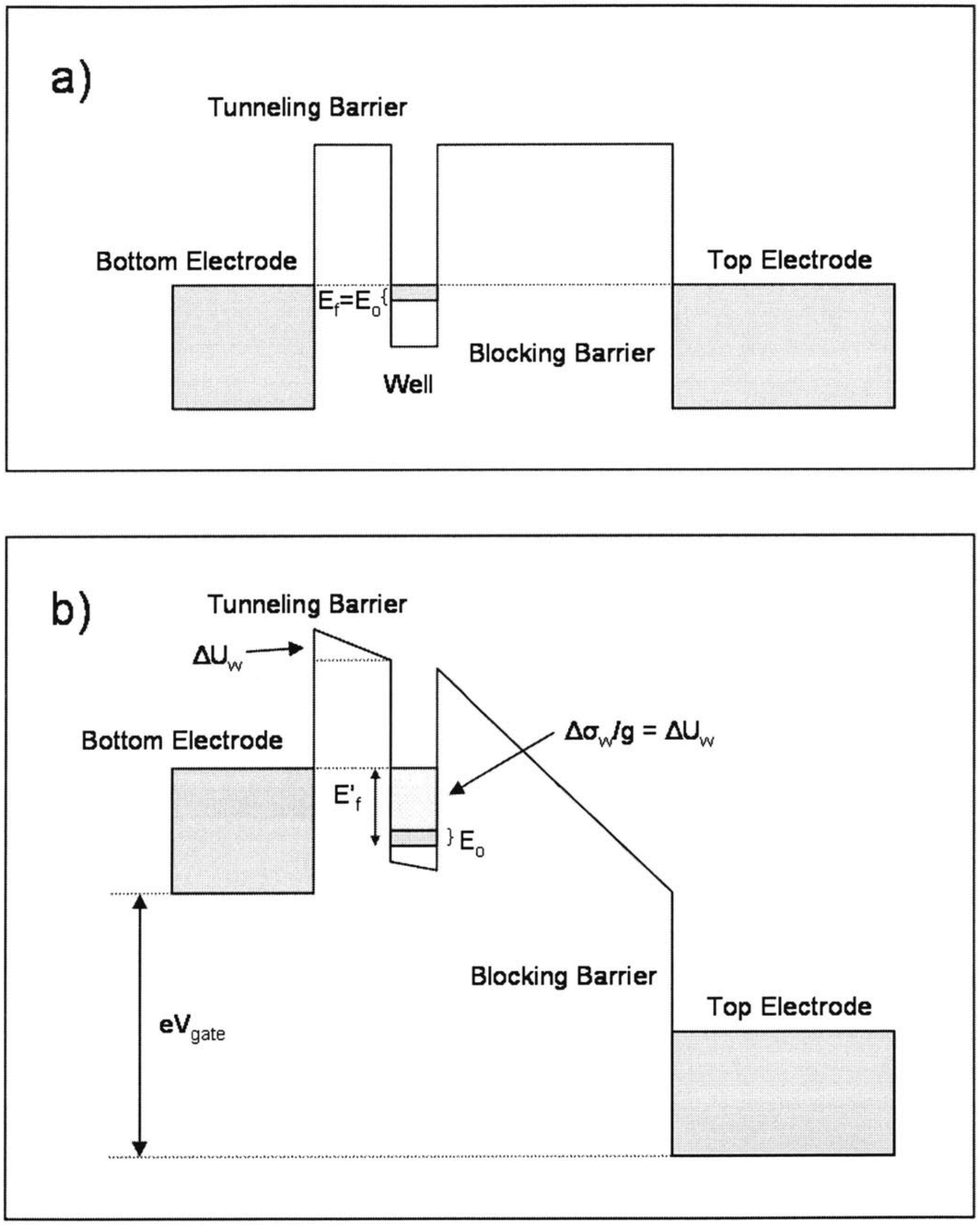
a)
Tunneling Barrier
Bottom Electrode
Top Electrode
$E_f = E_o$
Blocking Barrier
Well
b)
Tunneling Barrier
ΔU_w
Bottom Electrode
$\Delta\sigma_w/g = \Delta U_w$
E'_f
E_o
Blocking Barrier
Top Electrode
eV_{gate}

Figure 2-4: Effect of a voltage bias on the Fermi level of the well. Inset a) shows the system in equilibrium and the well has a Fermi energy of E_o. Inset b) shows that when a bias V_{gate} is applied, the Fermi level of the well increases by ΔU_w rather than eV_{gate}. As shown above, $\Delta U_w = \Delta\sigma_w/g$ where $\Delta\sigma_w$ is the charge increase and g is the density of states. The effect of a finite density of states g is that the bottom electrode is not perfectly screened from the top electrode.

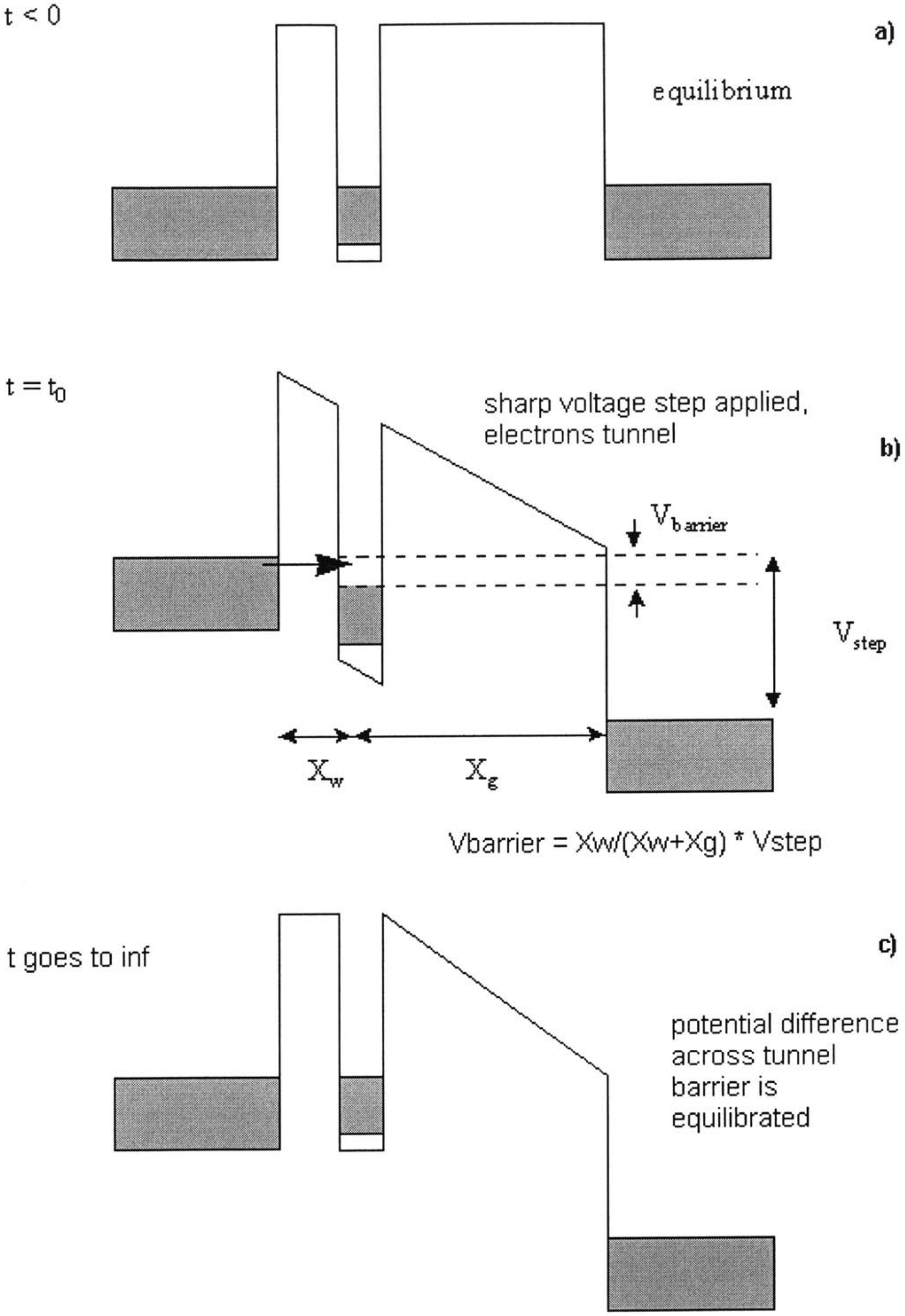
t < 0
a)
equilibrium
t = t0
sharp voltage step applied,
electrons tunnel
b)
Vbarrier
Vstep
Xw
Xg
Vbarrier = Xw/(Xw+Xg) * Vstep
t goes to inf
c)
potential difference
across tunnel
barrier is
equilibrated

Figure 2-5: Detailed evolution of the sample band structure during a step excitation. (Figure taken from Chan [2].)

tum well until the chemical potentials are equal and the applied voltage is dropped across the blocking barrier (see Figure 2-5c). The transient current would be detected via the gate across the blocking barrier. From the transient current, parameters such as $R_{tunneling}(V)$ can be extracted and analyzed.

2.3.2 Sensing Circuit

The sensing circuit used in the experiment is a capacitance bridge show in Figure 2-6. The top electrode of the sample (cap layer) is attached to a reference capacitor and the gate of a transistor. The common node is known as the balance point. Two separately scaled versions of a voltage excitation with opposite polarities are applied to the bottom electrode of the sample (substrate) and the free lead of the reference capacitor. The voltage output at the balancing point V_B is inputted into a HEMPT transistor for amplification. The output data is taken from after the amplification stage. The tunneling current can be determined by:

$$I_{tunneling} = -C_\sigma \frac{dV_s}{dt} \tag{2.2}$$

The proportionality constant C_σ depends on the thickness of the layers in the sample. For an explanation see Chan's thesis, appendix A [2].

The voltage to be applied to the reference capacitor V_s and to the sample V_{sample} is applied such that after the transient has decayed away the voltage from the excitation at the balance point V_B is zero. Some elementary circuit analysis of the bridge shows that this occurs when:

$$V_s \times C_s = -V_{sample} \times C_{sample} \tag{2.3}$$

Thus if V_{sample} takes on the typical form show in Figure 2-7a, then V_s will have the same form but scaled by $-C_{sample}/C_s$ as shown in Figure 2-7b. Thus by applying the wave forms in Figure 2-7a and 2-7b to the sample and the standard capacitor respectively, we eliminate any offset from the excitation as shown in 2-7c, and thereby gain in measurement sensitivity.

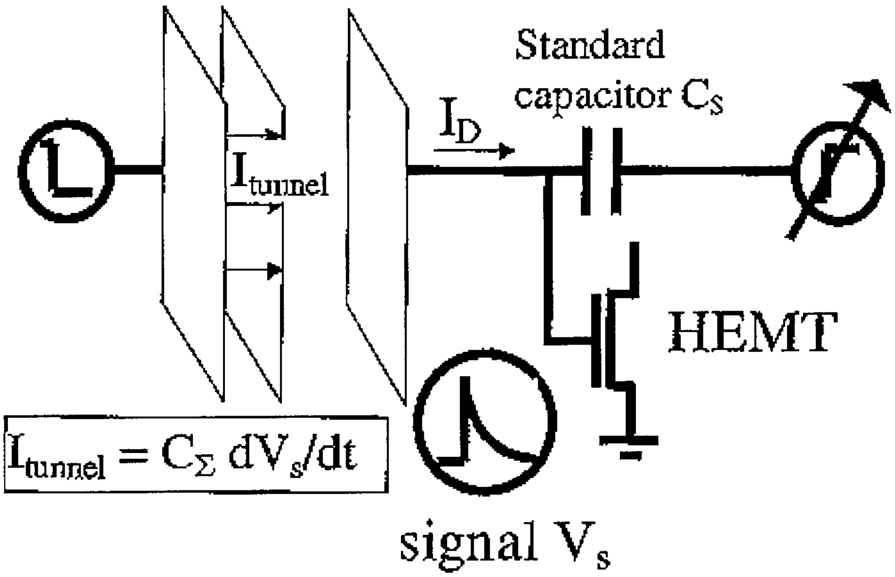

Figure 2-6: Sensing circuit used in the experiment. (Figure taken from Chan [2].)

The voltage amplitude that we apply to the standard capacitor has the opposite polarity of the voltage applied to the sample and is scaled by C_{sample}/C_s. The process of determining this scale factor is called *balancing the bridge*. Since C_s is known and we apply V_{sample}, we balance the bridge by choosing V_s such that V_B decays to the DC value. With the correctly determined V_s we can measure the low frequency capacitance of the sample using the relation:

$$C_{low} = \frac{-V_s}{V_{sample}} \times C_s \tag{2.4}$$

Also the profile of typical input wave from shown in Figure 2-7 is not accidental, as is it is chosen to have a zero mean to avoid DC biases across the sample, and allows one to see positive and negative step responses of the sample.

Measurements of C_{low} relate to the DOS of the 2DEG. Ashoori[1] has calculated the relation between C_{low} and the thermodynamic DOS of the 2DEG. The basic picture is described as follows. If the DOS is zero, then the low frequency capacitor

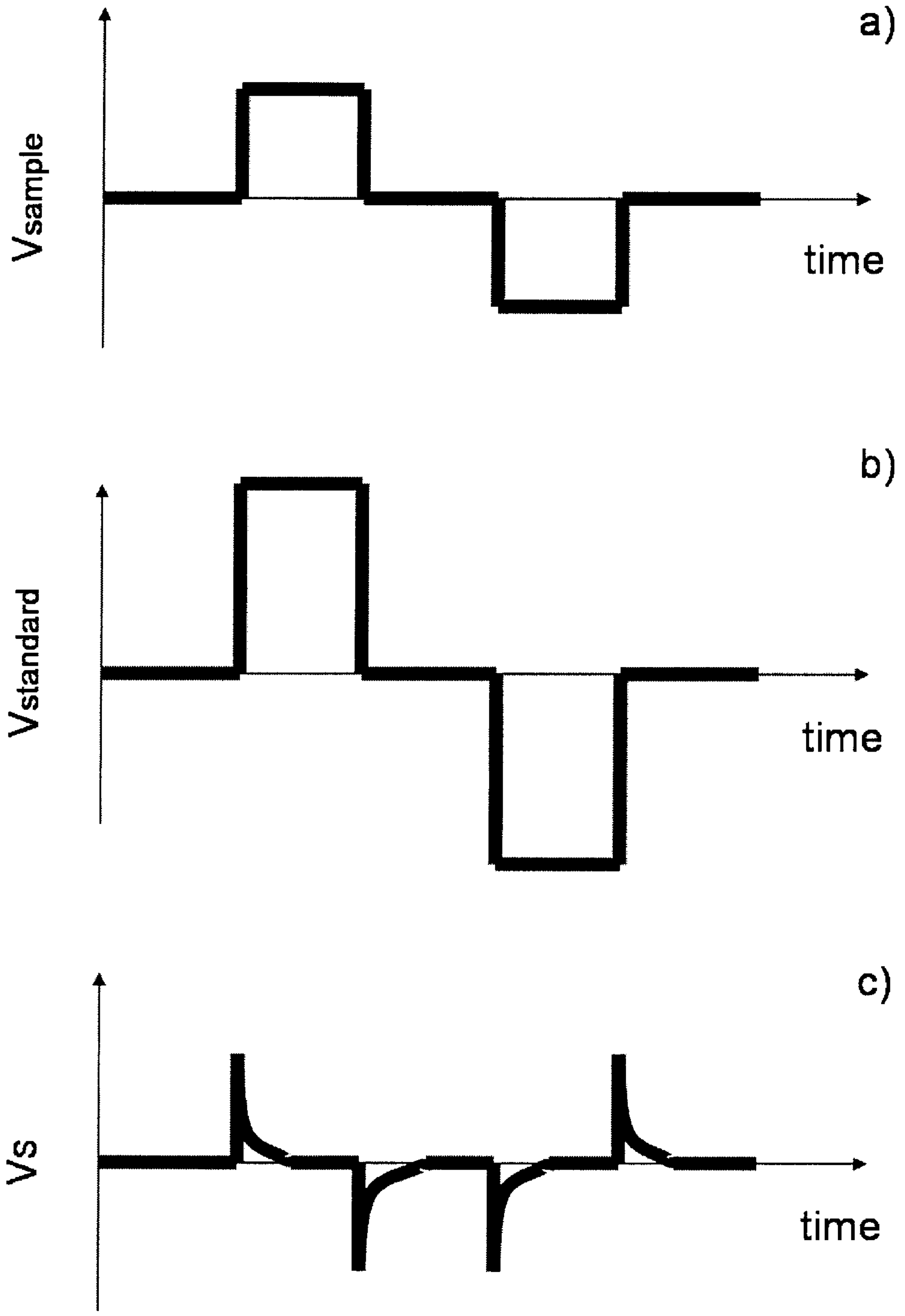

Figure 2-7: Typical input and output wave forms of the sensing circuit.

is formed between the top gate and the bottom contact. In this case $C_{low} = \frac{\kappa A}{X_b + X_w}$ where κ is the dielectric constant, A is the sample area, X_b is the blocking barrier width, and X_w is the well width. If the DOS is infinite, then the electrons can easily reside in the quantum well and the low frequency capacitor is formed between the top gate and the quantum well. In this case $C_{low} = \frac{\kappa A}{X_b}$. Thus we see that by measuring C_{low} we can determine the thermodynamic DOS of the 2DEG.

In typical experiments we apply a magnetic field perpendicular to the quantum, and we control the chemical potential of the quantum well by applying a DC bias to the sample via the contact. By measuring C_{low} verses sample bias we are able to produce plots like Figure 2-8 which reflect the Landau levels in the DOS for a 2DEG in a perpendicular magnetic field. Thus by setting the sample bias to $-375mV$ we can set the filling factor $\nu = 2$. In the experiment of this thesis, however, the field is parallel to the sample.

2.3.3 Experimental Setup

The full experimental setup is shown in Figure 2-9. A computer is used to trigger the sample and record the data. The pulse sequence fed by channel 1 and channel 2 are repeated occurrences of the wave forms shown in Figure 2-7. Extensive averaging had to be performed to recover the signal from noise. Typically 262,144 averages were made for a clean trace. A computerized signal averager was used rather than a standard oscilloscope. This was done since oscilloscopes typically don't have the data throughput to recover the signal. After digitizing one trace the oscilloscope needs $10ms$ to $100ms$ to reset to take another trace. But the transient times of the sample are usually around $200\mu s$. Thus if a standard oscilloscope was used most of the time would be spent in waiting for the oscilloscope to reset, and the required averaging would not be possible.

To solve this problem the EG&G model 9826 signal average was used instead of an oscilloscope. The 9826 averager plugs into two adjacent ISA slots on a personal computer. It is capable of adding 8 bits of a newly digitized signal to a 16 bit sum every $2ns$ and accepts a new trigger within $600ns$ of completion of the preceding

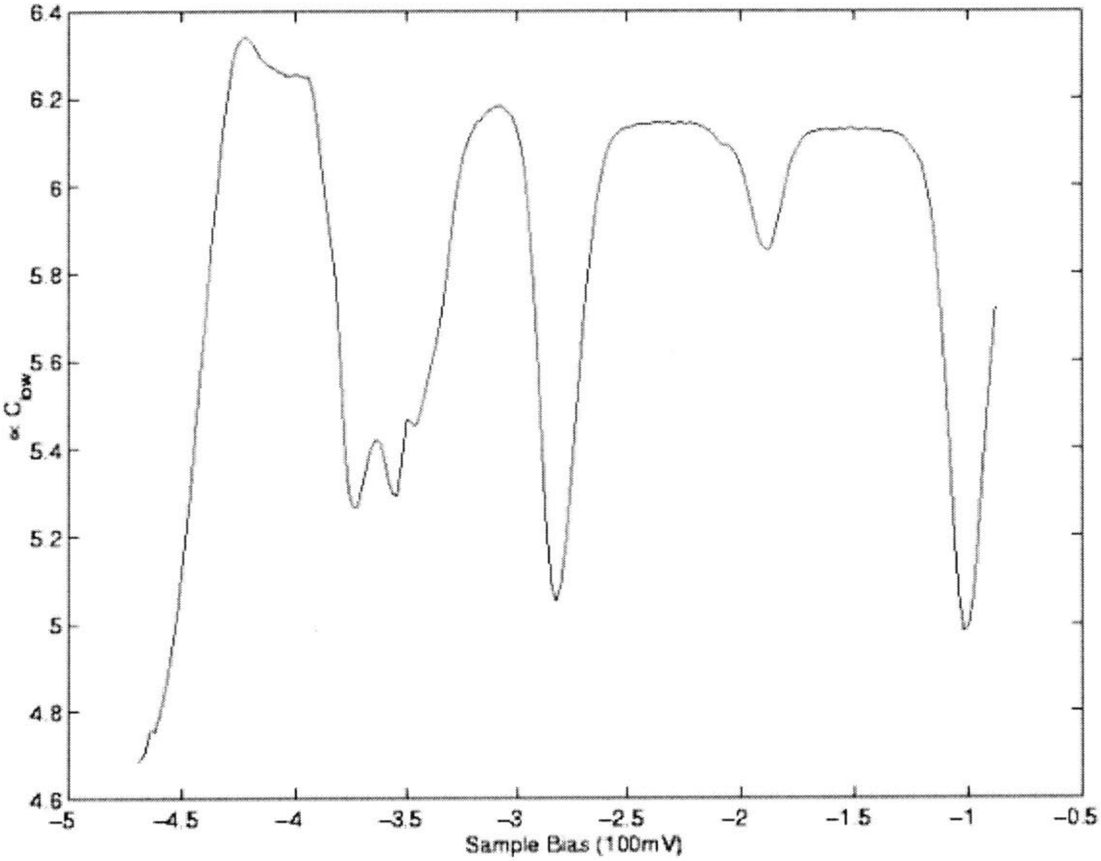

Figure 2-8: Data for the low frequency capacitance of the sample revealing the Landau levels in the DOS for a 2DEG in a perpendicular magnetic field.

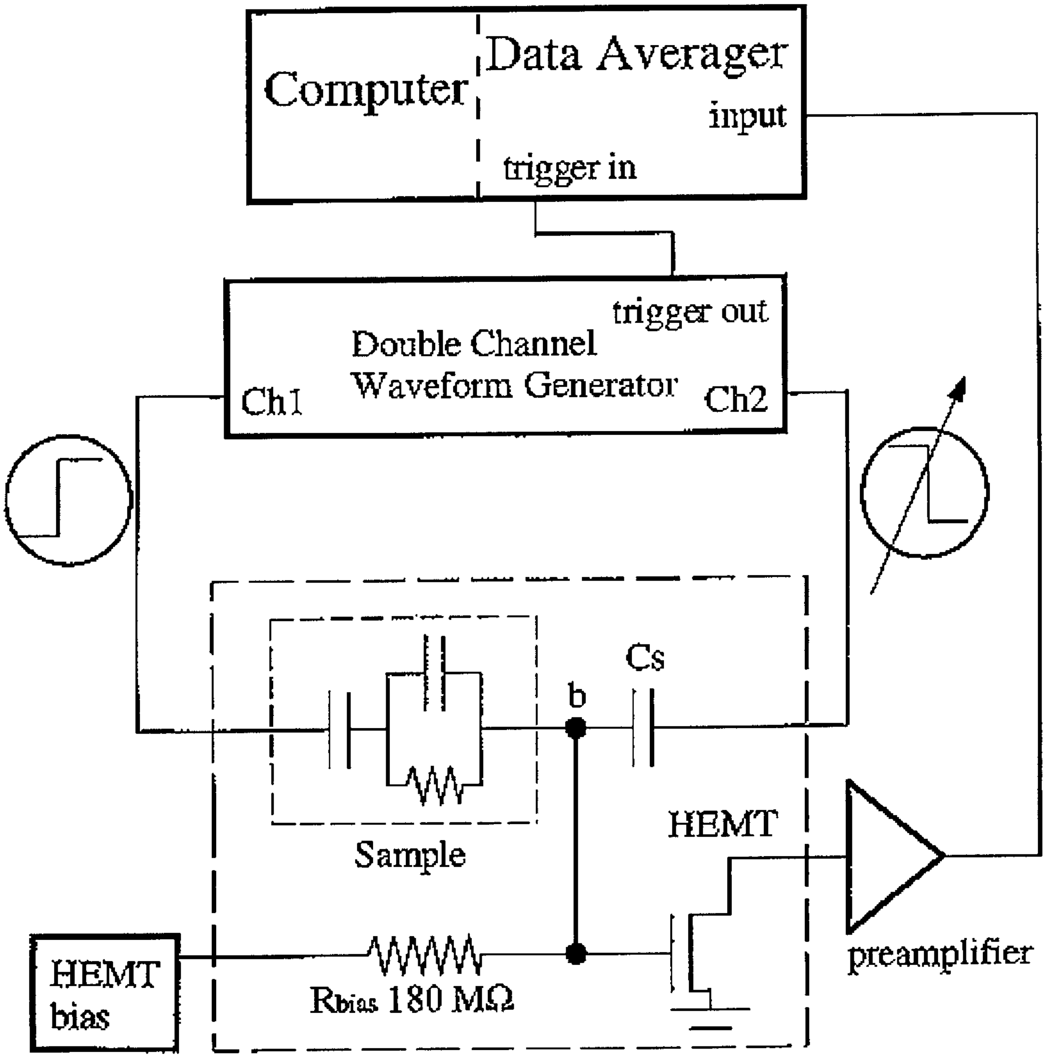
Computer
Data Averager
input
trigger in
trigger out
Double Channel
Waveform Generator
Ch1
Ch2
Cs
b
Sample
HEMT
preamplifier
HEMT bias
Rbias 180 MΩ

Figure 2-9: Complete experimental setup. (Figure taken from Chan [2].)

sweep. With this averager we are able to take data 1000 times faster than with an oscilloscope. In addition we use a *dithering* technique to increase the resolution of the average from 8 bits to 16 bits. Without the speed and resolution of the averager, this experiment would not be possible.

2.4 Sample Holder

The above mentioned circuit along with additional components are enclosed on a rotating sample mount shown in Figure 2-10. The space was quite limited so great care needed to be employed in properly mounting the elements. As shown in Figure 2-11 the elements included the sample, a hall sensor, a perpendicularly mounted transistor, a reference capacitor, and a $100M\Omega$ biasing resistor.

The stage to which all the elements are mounted rotates in a fixed plane in order to vary the angle of the applied field which is fixed to be oriented in the vertical direction. The hall sensor and the sample are mounted flat against the stage. Thus, for a given field we can measure the component of the field perpendicular to the stage via the hall sensor and the hall effect. We can then rotate the stage to minimize this component and thus position the field parallel to the stage.

In addition care needs to be employed in the mounting of the transistor. The gain of the transistor is affected by the amount of field perpendicular to its gate. This can lead to important undesirable effect as measurements are taken while the field is swept continuously. We thus position the field as indicated in Figure 2-12 so that the gate of the transistor is in the plane of the field at all points of rotation and the effect of the field on the gain of the transistor is minimized.

2.5 Typical Results: Shubnakov De Haas Oscillations

We conclude this chapter by presenting the results for a typical result measurement of Shubnakov De Haas Oscillations to indicate the validity of the Time Domain Capac-

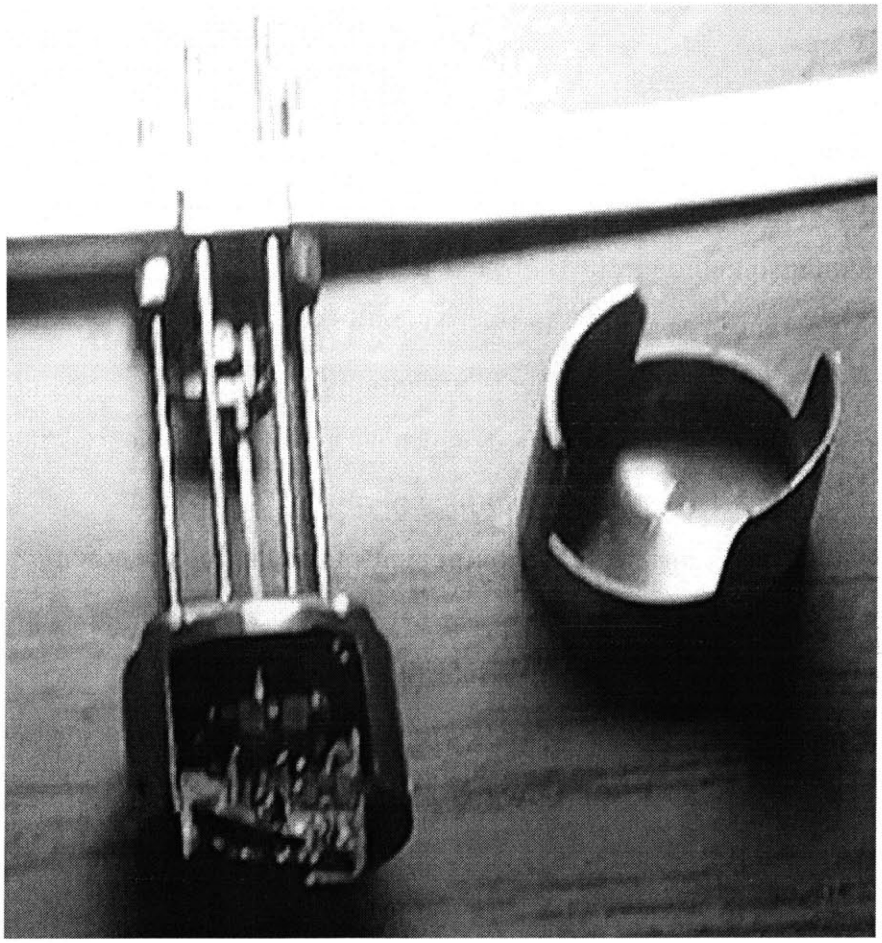

Figure 2-10: Photograph of the sample, sensing circuit, and hall sensor in the sample space mount.

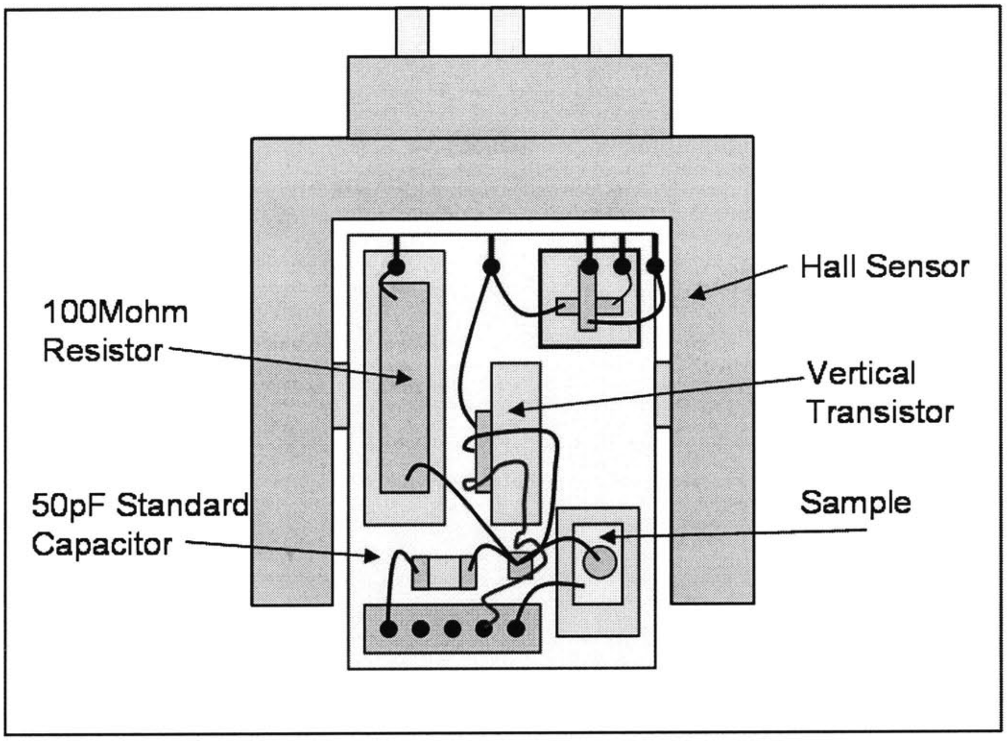
Hall Sensor
100Mohm
Resistor
Vertical
Transistor
50pF Standard
Capacitor
Sample

Figure 2-11: Explanatory diagram of the elements in the sample mount.

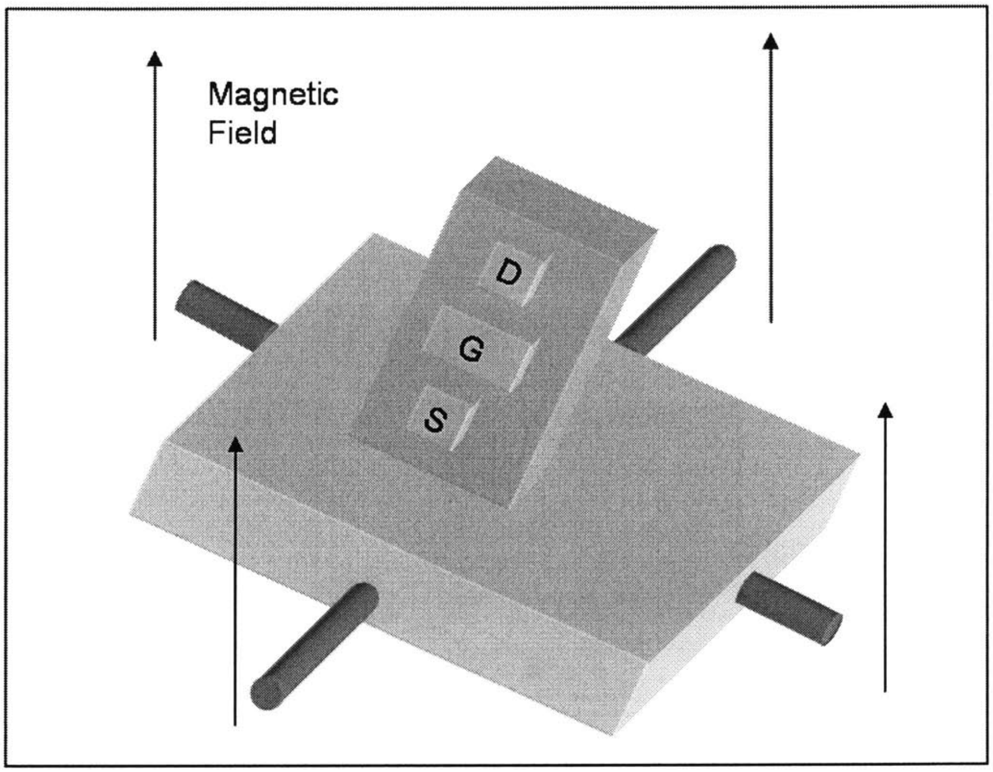
Magnetic
Field
D
G
S

Figure 2-12: The gate of the transistor must be aligned in the plane of the field so that gain of the transistor remains independent of the field.

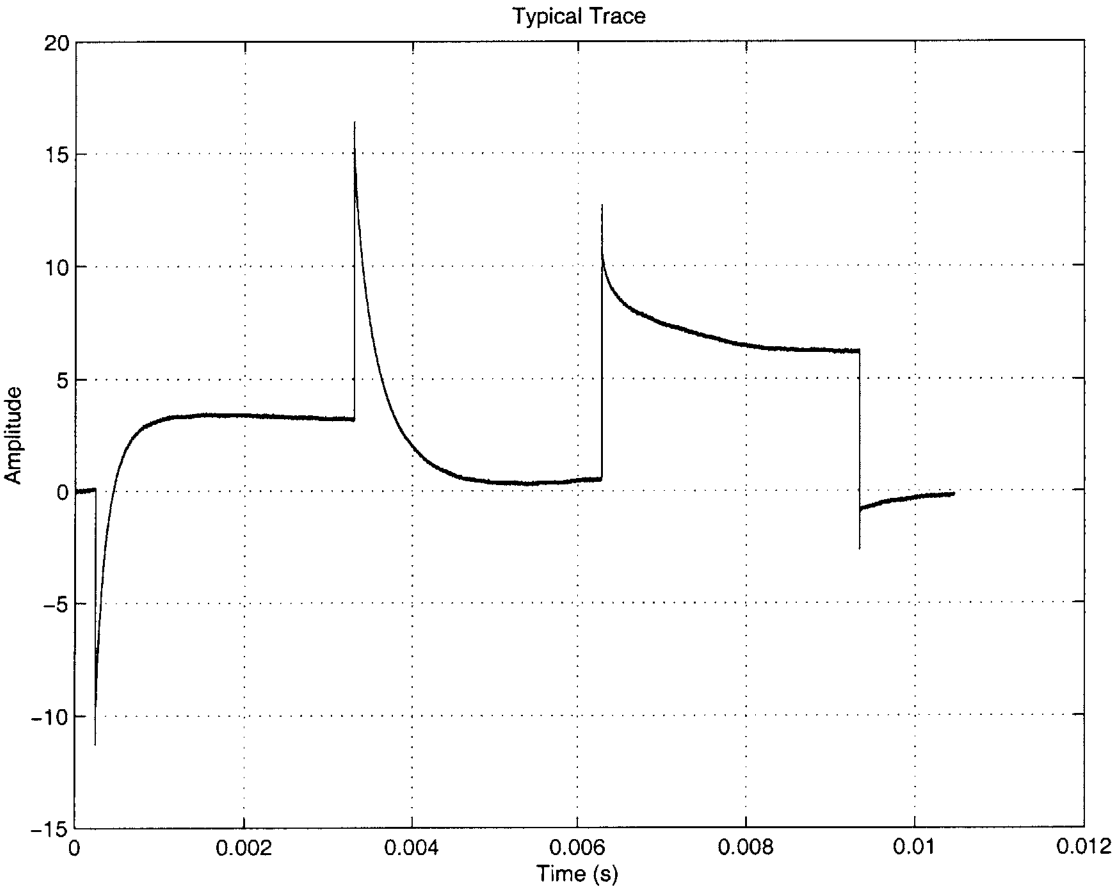

Figure 2-13: Typical output waveform.

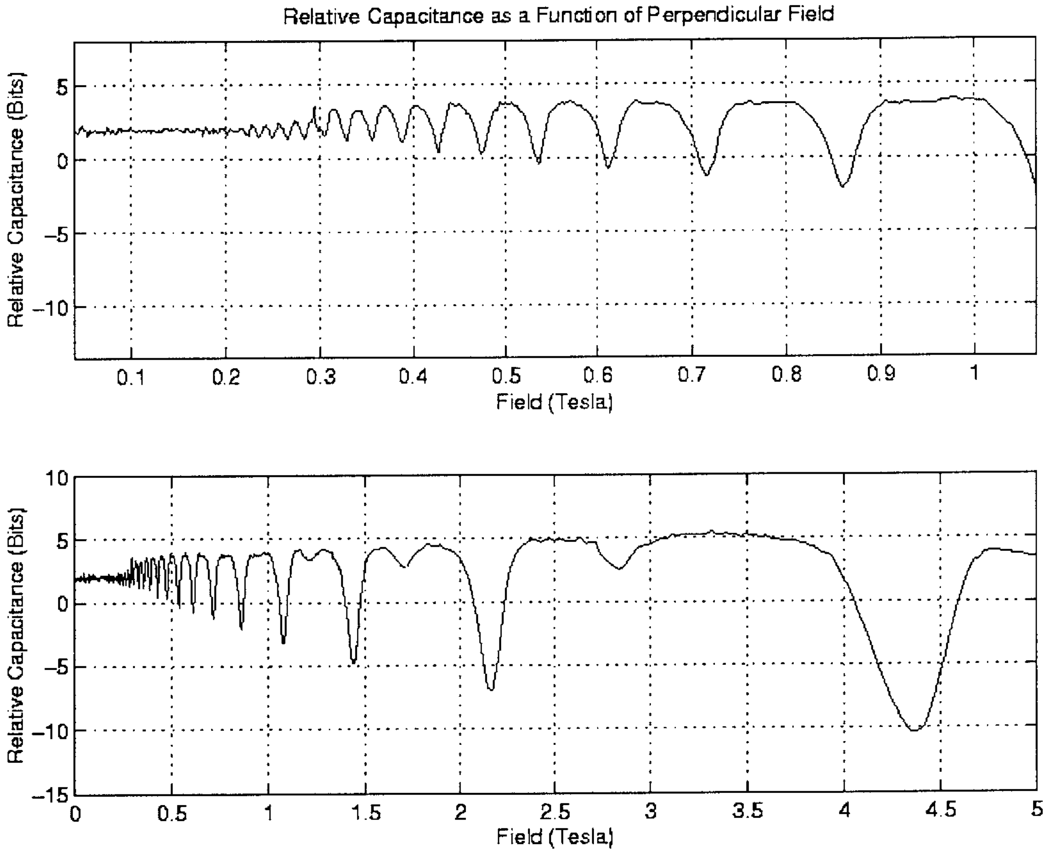

Figure 2-14: Low frequency capacitance as a function of perpendicular field.

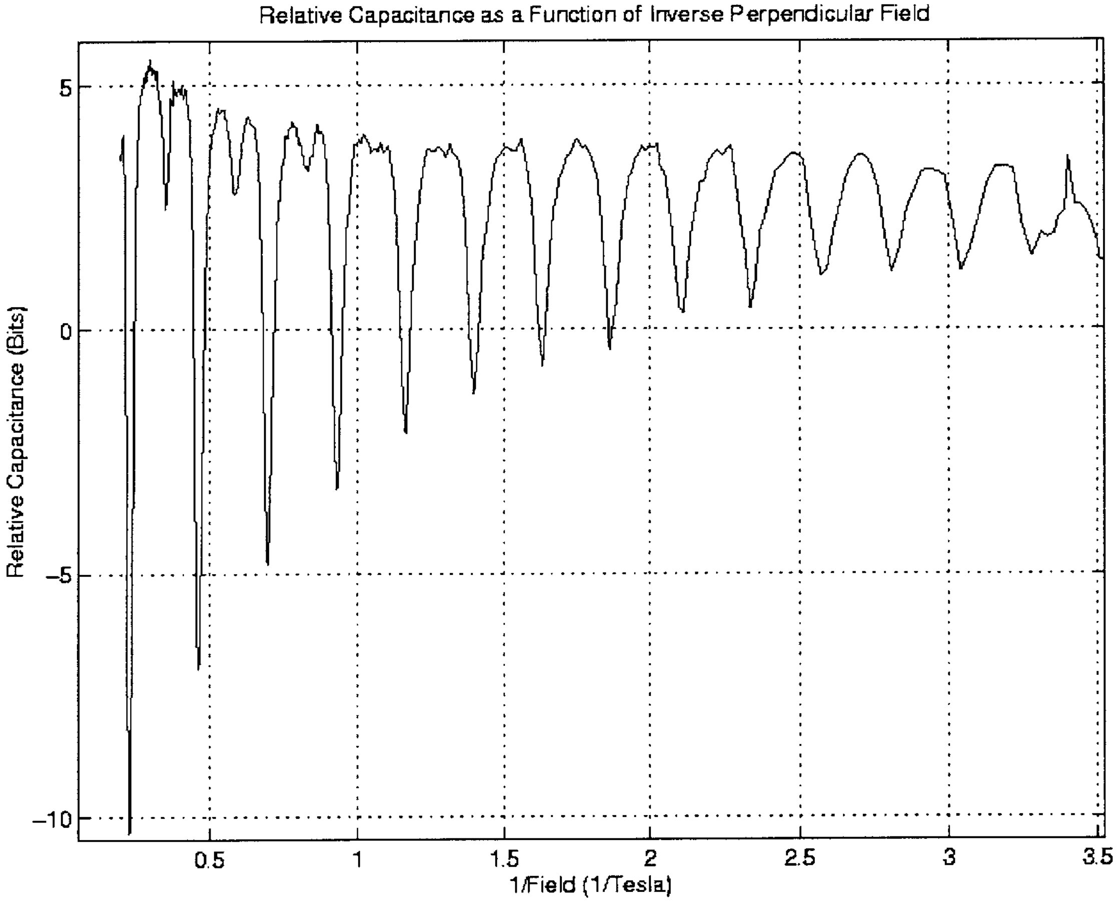

Figure 2-15: Low frequency capacitance as a function of 1/B indicating the conductivity is periodic in 1/B. This is a signature of Shubnakov De Hass oscillations.

itance Spectroscopy Technique. The waveforms applied to the sample and standard capacitor have the forms indicated in Figure 2-7. A typical output waveform is shown in Figure 2-13. As discussed above, we can use the balancing bridge to measure the low frequency capacitance of the sample. As we sweep a perpendicular magnetic field and measure the change in the low frequency capacitance we expect to see Shubnakov De Haas Oscillations. The oscillation in the sample low frequency capacitance as a function of magnetic field is shown in Figure 2-14. Figure 2-15 plots the same data as a function of the inverse field. The periodic result is a signature of the Shubnakov De Haas oscillation.

Chapter 3

Results for Zero-Field Tunneing

The main focus of this experiment is to understand the physics of tunneling from a two-dimensional electronic system into a three dimensional contact in the presence of an in-plane magnetic field. This process and tunneling processes in general are constrained by energy conservation and momentum selection rules. Thus, when considering how tunneling currents depend on various parameters, we must provide a physical picture in terms of band diagrams and also in terms of momentum space.

In this chapter we present a theoretical framework which will give insight into our experimental results. In particular, we first discuss the physics and results for tunneling in zero field. This introduces the basic concepts employed in understanding the tunneling events. The next chapter discusses tunneling in an in-plane field.

3.1 Zero Field Momentum Selection

Although ultimately we wish to consider the effects of an in-plane field, it is quite pedantic to first investigate the degenerate case of tunneling with zero field. In this case, electrons tunnel between a Fermi disc in the 2DEG and a Fermi sphere in the 3D contact as is shown in Figure 3-1. Within the scope of this picture, zero field tunneling can be viewed in an equilibrium and out of equilibrium context. Equilibrium tunneling is associated with AC measurements of tunneling conductivity and involves tunneling between the Fermi surface of the 2DEG and that of the contact. Tunneling

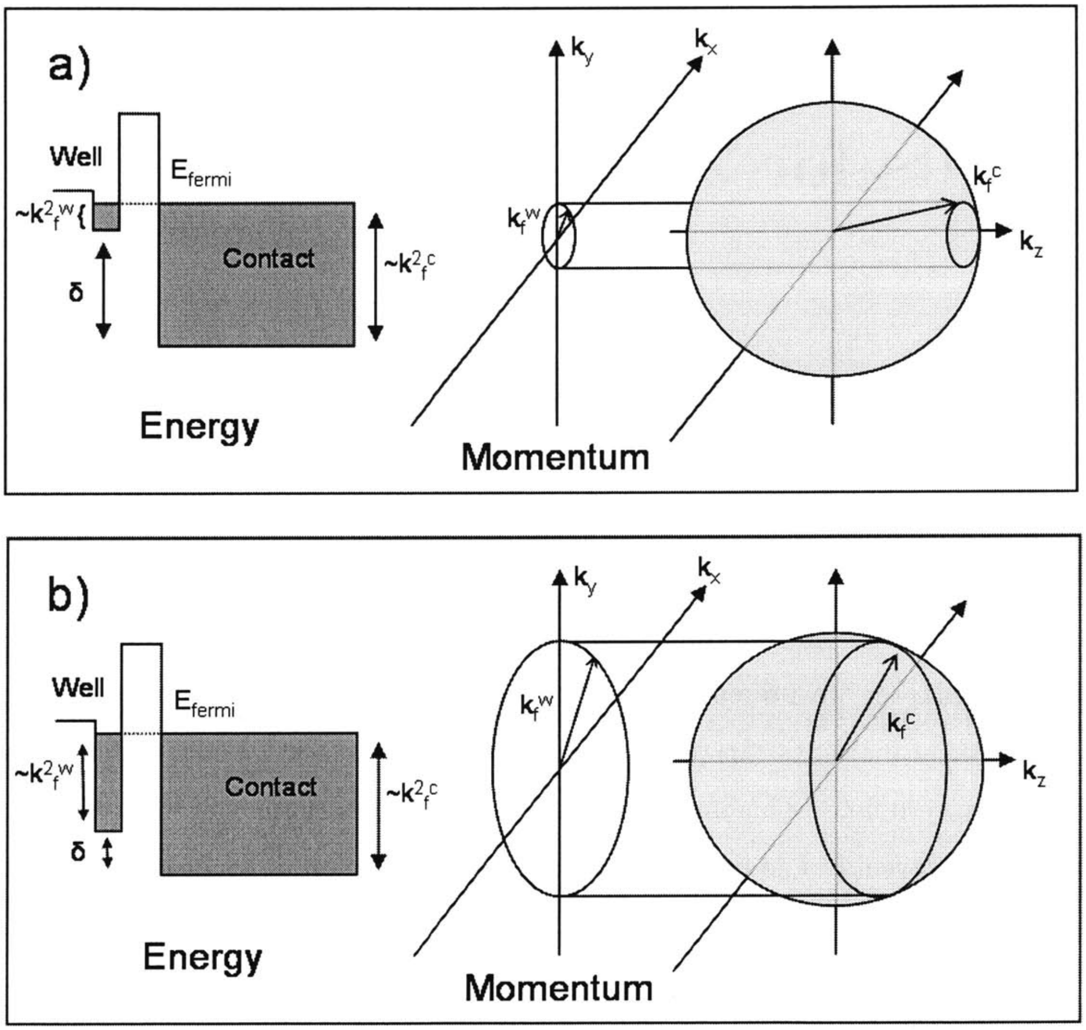
a)
Well
E_{fermi}
$\sim k^2{}_f{}^w$
δ
Contact
$\sim k^2{}_f{}^c$
Energy
k_y
k_x
$k_f{}^w$
$k_f{}^c$
k_z
Momentum
b)
Well
E_{fermi}
$\sim k^2{}_f{}^w$
δ
Contact
$\sim k^2{}_f{}^c$
Energy
k_y
k_x
$k_f{}^w$
$k_f{}^c$
k_z
Momentum

Figure 3-1: Zero field tunneling process in energy and momentum spaces. The insets show that as the bias is increased the tunneling circle in the contact is drawn toward the origin.

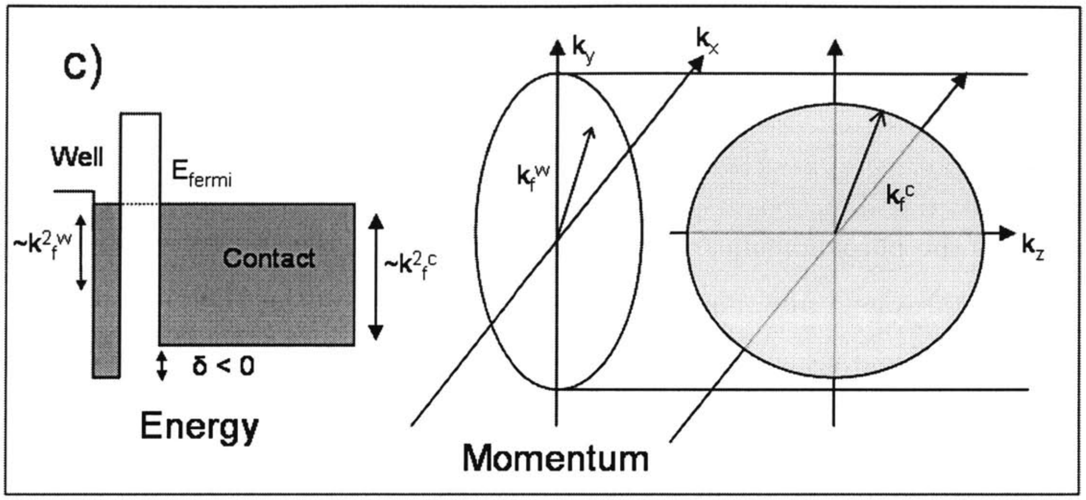

Figure 3-2: Beyond the critical bias momentum conservation no longer holds. Tunneling occurs via scattering off impurities and the tunneling conductance falls off as bias is increased.

out of equilibrium, however, considers the effect of step excitations on the tunneling conductivity and tunneling events are not necessarily confined to the Fermi surface. With this in mind we will now proceed to discuss equilibrium tunneling.

3.2 Equilibrium Tunneling

Our aim in this section is to explain how the zero-field equilibrium tunneling current depends on voltage bias. Figure 3-1 depicts zero-field tunneling in both the energy and momentum spaces for the cases where the band offset for the 2DEG is higher than the contact and vice versa. For the first case, electrons tunnel between a disc and a sphere with the constraints of momentum and energy conservation. The constraint of energy conservation can be introduced by only considering tunneling form the edge of the Fermi disc and the shell of the Fermi sphere. Momentum conservation can be seen by considering only those states in the sphere that intersect the cylindrical projection of the edge of the disk. Thus we can see in Figure 3-1 that tunneling occurs from the edge of the Fermi disk to the edge of an annular cross-section of the Fermi sphere parallel to the 2DEG Fermi edge.

The tunneling current is determined by the integral of the following product, over states that conserve energy and the k_x, k_y momentum vectors.

$$\frac{1}{\tau(k_z)} n_1(k_x, k_y) n_2(k_x, k_y, k_z) dk'_x dk'_y \tag{3.1}$$

Here, k_z is the perpendicular momentum component of the sphere, $n_1(k_x, k_y)$ is the density of states as a function of transverse momentum in the 2DEG, and $n_2(k_x, k_y)$ is that for the contact. We can also assume that $\tau(k_z)$ is an increasing function of k_z [5]. The integral is not easily expressed, but we can see that there are two factors affecting the tunneling current, the perpendicular momentum of the contact state and the product of the tunneling areas in k-space.

Thus, when the density in the 2DEG is zero the tunneling current is zero since there are no electrons. As show in Figure 3-1, increasing the density from zero causes the position of the center of the circular cross section in the contact to retract toward the origin and the radius dilates along the surface of the sphere. This represents the two competing factors. The k_z final is decreasing while the product of the tunneling areas is increasing. Thus the tunneling conductance increases from zero and then decreases [4].

Once the radius of the disk exceeds the radius of the sphere, then we are at a point where the band edge of the contact is greater that that of the 2DEG. We are, thus, in the second situation show in Figure 3-1. In this situation momentum cannot be directly conserved and so tunneling occurs via impurity scattering sites. The tunneling conductance falls sharply after that point is reached.

Since the density of electrons in the 2DEG is one to one with the voltage bias, we can understand how the tunneling current is effected by voltage bias. That is, when the well is biased in depletion, the tunneling current is zero since there are no electrons in the well. However as we increase the bias, drawing more electrons in the well, the tunneling current first increases and then decreases due to a decrease in k_z and an increase in the tunneling area products. As we increase the bias further, the tunneling conductance fall off as we enter the impurity assisted scattering regime.

Data reflecting this behavior is shown in Figure 3-6 below.

3.3 Out of Equilibrium Tunneling

The effect of step excitations on the tunneling conductance can more clearly be seen by considering the constraints of momentum and energy conservation more quantitatively. Analytically, momentum conservation can be depicted as:

$$k_{x,Fermi} = k'_{x,Fermi} \tag{3.2}$$

$$k_{y,Fermi} = k'_{y,Fermi} \tag{3.3}$$

where $k_{x,Fermi}$ and $k_{y,Fermi}$ are the momentum components for the 2DEG, and $k'_{x,Fermi}$ and $k'_{y,Fermi}$ are that for the contact. In addition m would indicate the effective mass which, for simplicity, is assumed to be the same for all directions in the 2DEG and contact.

Energy conservation can then be depicted as:

$$\frac{\hbar^2 k^2_{x,Fermi}}{2m} + \frac{\hbar^2 k^2_{y,Fermi}}{2m} + E_o^{2DEG} = \frac{\hbar^2 k'^2_{x,Fermi}}{2m} + \frac{\hbar^2 k'^2_{y,Fermi}}{2m} + \frac{\hbar^2 k'^2_{z,Fermi}}{2m} + E_o^{contact} \tag{3.4}$$

In addition to the previously mentioned variables, $k'_{z,Fermi}$ is the momentum component for the contact, E_o^{2DEG} is the band offset for the 2DEG, and $E_o^{contact}$ is the band offset for the contact.

Canceling equivalent terms in equation 3.4 we are left with:

$$k'_z = \frac{\sqrt{2m(E_o^{2DEG} - E_o^{contact})}}{\hbar} = \sqrt{2m\delta} \tag{3.5}$$

Thus, equilibrium tunneling occurs between states on the edge of the Fermi ring of the 2DEG and states on the Fermi surface of the contact with $k'_z = \sqrt{2m\delta}$, i.e. a ring in k-space centered at k'_z. This is the result that we geometrically discussed in the previous section.

3.3.1 Positive Excitations

We are now in a position to discuss positive excitations, that is excitations that increase δ the band offset of the well with respect to the contact. This corresponds to positive excitations in voltage applied to the bottom electrode of the sample which contacts the substrate as shown in Figure 2-3. Figure 3-3 indicates what is happening in momentum and energy space during a positive excitation. We see that during a positive excitation the center of the circular cross section of interest in the Fermi sphere is pushed outward and the radius contracts. Electrons in the Fermi disk of the well outside this radius then can tunnel into the plane of the circular cross section and above the Fermi level of the sphere. Scattering processes then distribute the electrons around the Fermi sphere.

We can look at this more carefully to gain further insight by considering certain states as they tunnel. In particular consider the states that tunnel directly at the Fermi level of the contact as indicated in Figure 3-3 in the band diagram figure. These are the lowest energy states in the well that can tunnel into the contact as the states lower in energy are occupied in both the well and contact. These states correspond to the inner radius of the Fermi disk indicated in Figure 3-3. Because these states tunnel directly at the Fermi level of the contact we know they tunnel onto the surface of the Fermi sphere. Thus as we project the denoted circle onto the sphere indicating momentum conservation, we see that these states tunnel into the edge of the circular cross section at the outwardly shifted kz'. The more energetic states in the well are those that in momentum space corresponding to larger radii in the Fermi disc. These states tunnel beyond the circular cross section but in the same plane. We know they tunnel into higher energy states as the distance from the origin is larger for these states. Thus tunneling can be seen as the projection of the annulus in the sphere onto the plane at k_z' and subsequent scattering occurs to bring the configuration into an equilibrium sphere.

We can see that as the δ increases with larger positive excitations, kz' shifts

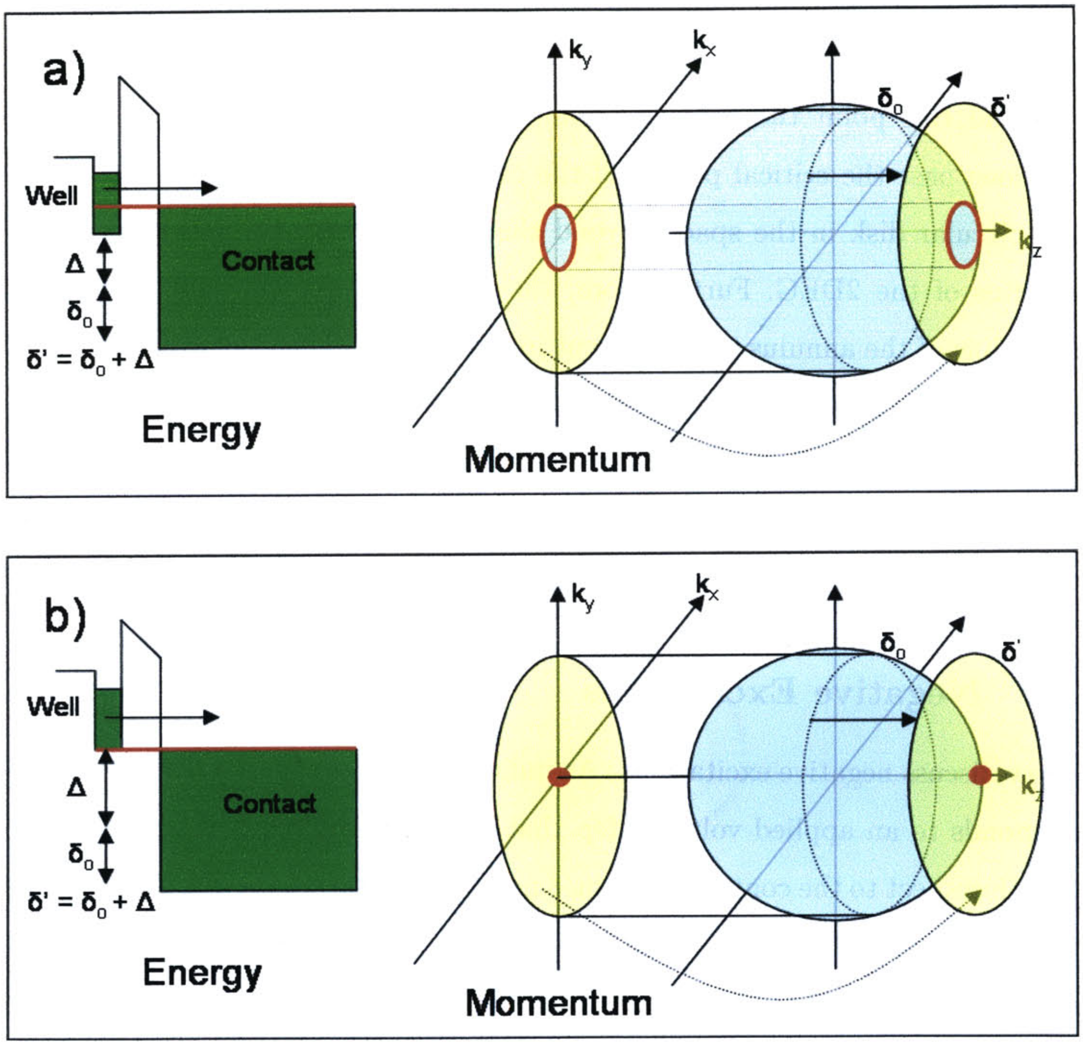
a)
Well
Δ
δ0
δ' = δ0 + Δ
Contact
Energy
ky
kx
δ0
δ'
kz
Momentum
b)
Well
Δ
δ0
δ' = δ0 + Δ
Contact
Energy
ky
kx
δ0
δ'
kz
Momentum

Figure 3-3: Inset a) shows how the cross section of interest in the 3D momentum space of the contact shits out during a positive excitation. Tunneling then proceeds from the well to the contact as indicated in the diagram. Inset b) shows the critical point where momentum is still able to be conserved.

further outward and the inner radius of the annular region contracts, thus allowing more tunneling. This happens up until the critical point indicated in Figure 3-3. This point happens when δ equals the bandwidth of the contact, and at this point the annular region becomes a circle tangential to the Fermi sphere, allowing the greatest area for tunneling. We expect the tunneling conductance to be the largest at this point.

Beyond this point the tunneling plane k' shifts off the sphere. Thus for large excitations past the critical point, all the electrons in the 2DEG are able to tunnel into a circular disk in the space beyond the sphere, where the radius is defined by the radius of the 2DEG. Furthermore, the effect of the Fermi sphere defining the inner radius of the annulus is not present in this regime. Thus the available tunneling area constituted by the disk is constant as excitation height is increased. One would expect the tunneling that conductance would then becomes more or less independent of excitation height and levels off. However, since the tunneling matrix element increases with k_z the tunneling conductance increases.

3.3.2 Negative Excitations

We now discuss negative excitations. As indicated in Figure 3-4, a negative excitation corresponds to an applied voltage step that decreases the relative band offset of the well with respect to the contact. During a negative excitation the circular cross section in the Fermi sphere is drawn closer to the origin. The relevant electrons at this point are in an annulus in the plane of the circular cross section defined by an outer edge on the Fermi sphere and an inner edge of the radius of the Fermi disk. These electrons tunnel into the empty states in the well. The electrons then rearrange in the Fermi sphere via scattering. Again we can draw insight by considering the electrons from the sphere that tunnel at the Fermi level of the Fermi disk. These electrons correspond to the inner edge of the annulus and greater radii correspond to higher energy electrons and tunnel above Fermi level in the disk.

As the negative excitations increase the outer radius of the tunneling annulus increases, thus the tunneling conductance increases. This happens until the critical

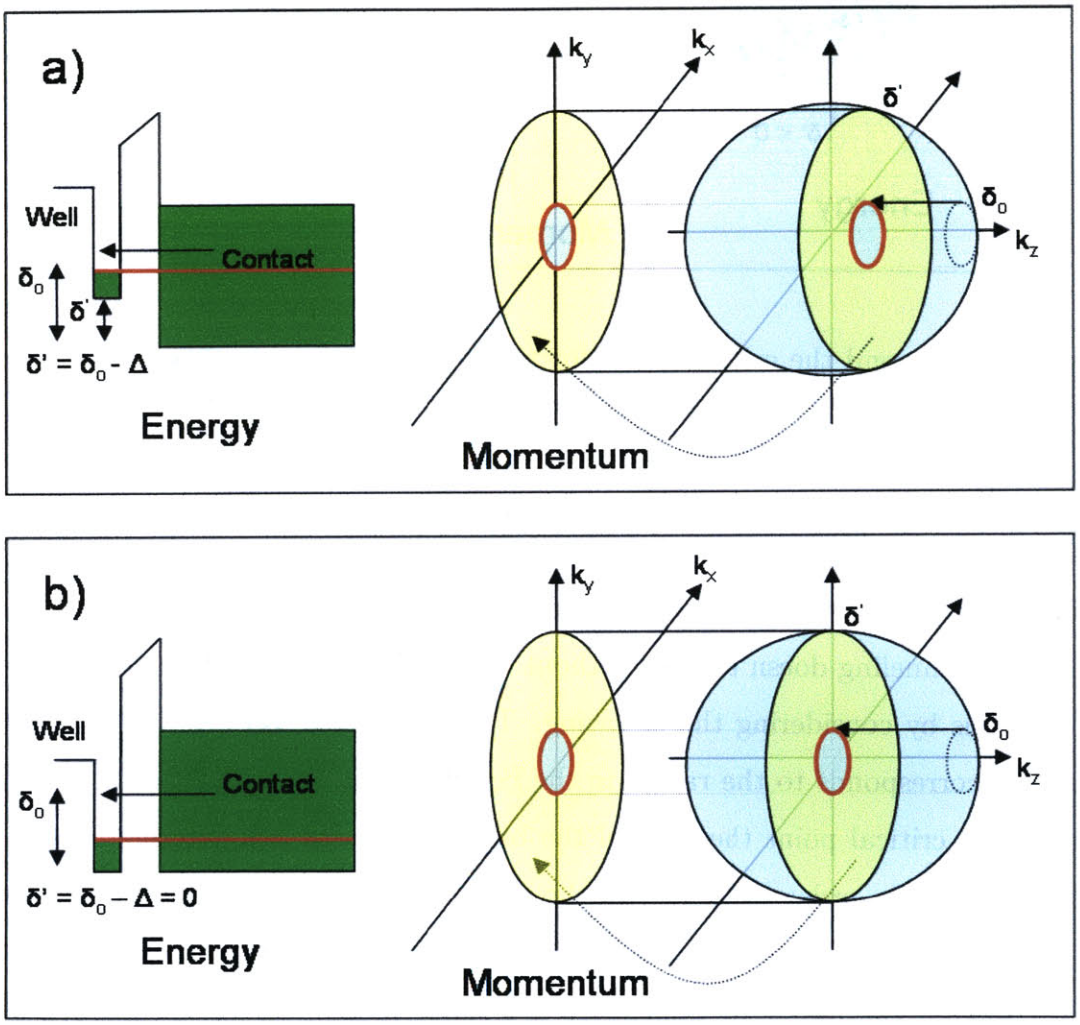
a)
Well
Contact
δ_0
δ'
$\delta' = \delta_0 - \Delta$
Energy
k_y
k_x
δ'
δ_0
k_z
Momentum
b)
Well
Contact
δ_0
$\delta' = \delta_0 - \Delta = 0$
Energy
k_y
k_x
δ'
δ_0
k_z
Momentum

Figure 3-4: Inset a) shows how the cross section of interest in the 3D momentum space of the contact shits inward during a negative excitation. Tunneling then proceeds from the contact to the well as indicated in the diagram. Inset b) shows the critical point where momentum is still able to be conserved.

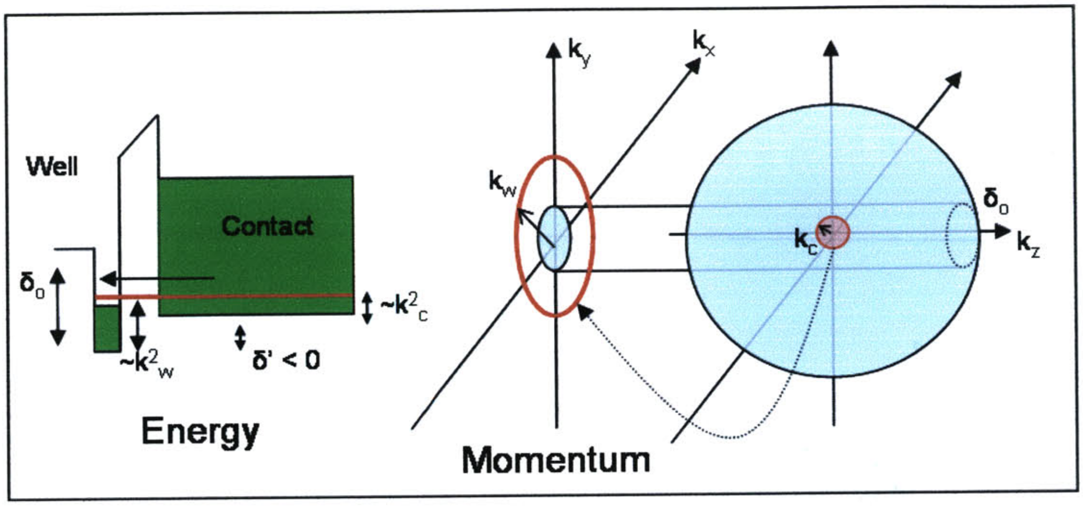

Figure 3-5: Beyond the critical point for negative excitation, tunneling process cannot conserve momentum. As indicated in the figure, processes that conserve energy require tunneling from a sphere of smaller radius in the contact to a circle of larger radius in the well. Thus no projection of the k-vector on the sphere can overlap with a k-vector on the disk and momentum cannot be conserved.

point shown in Figure 3-4 where the annular region is centered at the origin. Beyond this point tunneling doesn't occur without scattering as indicated in Figure 3-5. We can see this by considering the following. The bandwidth from the bottom edge of the band corresponds to the radius in the Fermi disk or Fermi sphere. When we are beyond the critical point the edge of the band in the well is lower than that of the contact. Thus in order to tunnel at the same energy we have to be in a situation where we are tunneling from a smaller radius in the sphere to a larger radius in the well. Because the radius of the sphere is smaller than the wheel it is not possible to conserve momentum. Thus any tunneling process happens via scattering and the tunneling conductance drops off.

3.4 Data and Interpretation

The data in Figures 3-6 and 3-7 indicate the observations discussed above for both equilibrium and out of equilibrium tunneling. For equilibrium tunneling in Figure 3-6

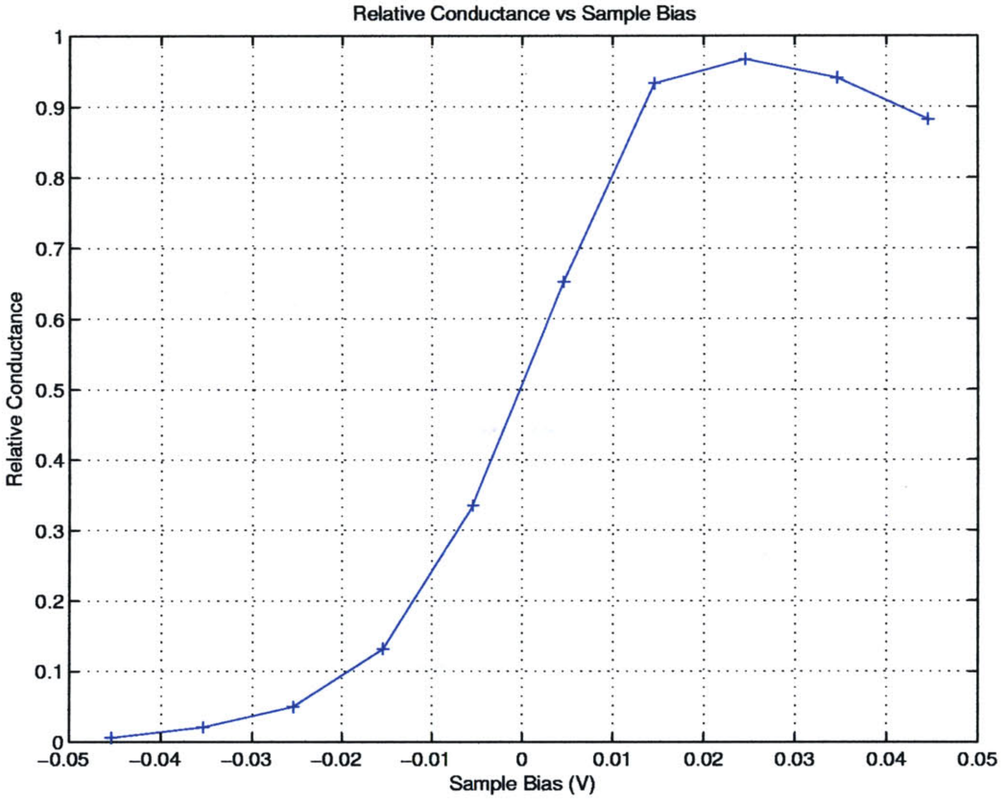

Figure 3-6: Equilibrium tunneling data.

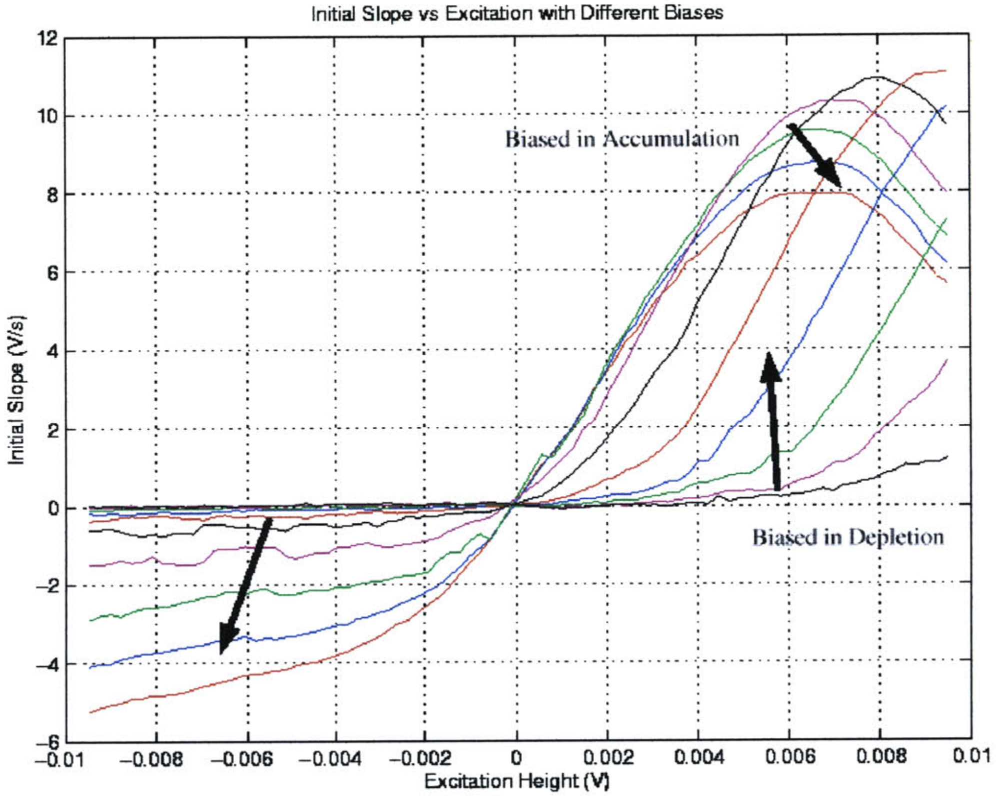

Figure 3-7: Tunneling out of equilibrium data. The excitation is applied to the substrate of the sample and the excitation is applied across the entire sample structure. The curve at the base of the two arrows pointing away from the horizontal axis correspond to the sample biased in depletion. The arrows indicate curves corresponding to increasing well densities.

we see that the tunneling conductance rises and then falls off as the bias is increased. In the figure an increasing bias corresponds to increasing the well density.

Figure 3-7 presents the data for out of equilibrium tunneling. The arrows indicate curves corresponding to increasing well density. When the sample is biased in accumulation we see that the tunneling conductance for negative excitations (positive voltages) increases and the drops off and for positive excitations it increases negatively. As the bias is increased and more electrons accumulate under the well the negative excitation bulge slowly creeps in toward lower excitations. This makes sense since as the Fermi disc increases in radius, k_z draws closer to the origin making the drop off point reachable at lower excitations. Also notice that the conductance for positive excitations (negative voltages) increases as density is increased as one would expect. Also the conductance increases slightly for high negative excitation as discussed above.

Chapter 4

Results for In-Plane Field Tunneling

While the effect of an in-plane field has little effect on the shape of the wave function in the well, the effect on the tunneling conductance can be quite dramatic as shown in Figures 4-1, 4-2, and 4-3. Figure 4-1 show that the conductance peak as a function of density shifts to higher densities and broadens as the applied magnetic field is increased. Also Figures 4-2 taken from Snell [6] shows the interesting effects of oscillations in the tunneling conductance as the field is swept. These oscillations are periodic in 1/B and Figure 4-3 indicates that the frequency of these oscillations increases monotonically with bias.

It is our aim in this section to present a theoretical picture biased on the works of Lebens [3] and Snell [6] that accounts for these previous findings. We also extend the model through the use of simulations to incorporate the effect of out of equilibrium tunneling. At the end of the section we present some preliminary experimental findings.

4.1 Basic Theoretical Picture

We wish to provide a theoretical model for the 2D quantum well in the vicinity of a 2D contact with an applied in-plane magnetic field as shown for the coordinates in

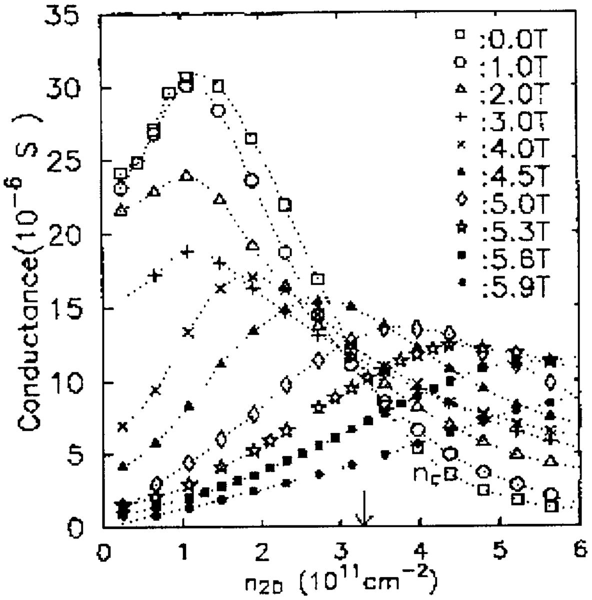

FIG. 2. Measured ac tunneling conductance vs well density for various magnetic fields. The zero-field cutoff density (n_c) is marked by an arrow.

Figure 4-1: Effect of an in-plane field on tunneling conductance as a function of well density. (Figure taken from Lebens [3].)

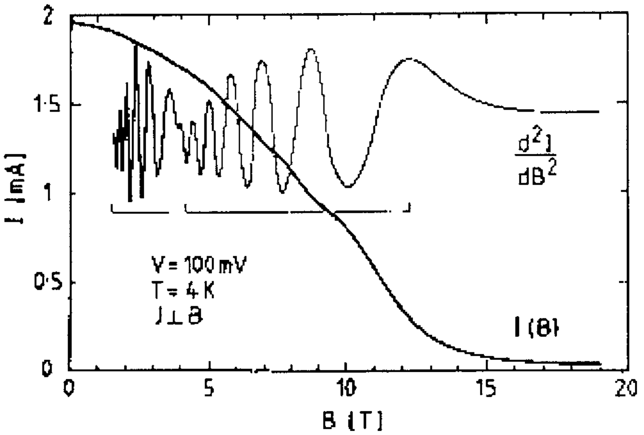

FIG. 2. Variation of current I and $\partial^2 I/\partial B^2$ with B for forward-bias voltage $V = 100$ mV. Mesa diameter $= 200$ μm. The two series are distinguished by horizontal brackets.

Figure 4-2: Effect of an in-plane field on tunneling conductance. Oscillations are seen. (Figure taken from Snell [6].)

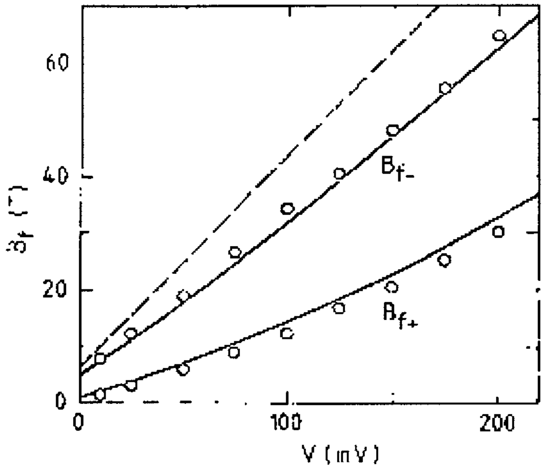

FIG. 3. Variation of B_f with bias voltage V for each series. Experiment: circles. Theory: bulk Landau states, dashed line; interfacial Landau states, solid lines.

Figure 4-3: Dependence of the frequency of the two sets of oscillations on well density. (Figure taken from Snell [6].)

Figure 4-4.In order to accomplish this we first consider the effect of the field in the gauge,$\vec{A} = (0, Bx, 0)$.

The vector potential is incorporated into Schrödinger's equation in the usual manner, and solutions of the from $\psi(\vec{r}) = exp(ik_y y + ik_z z)\phi(x)$ are sought out. So, proceeding we write Shrödinger's equation as:

$$\frac{1}{2m^*}(-i\hbar\nabla + e\vec{A})^2\psi(\vec{r}) + U(\vec{r})\psi(\vec{r}) = E\psi(\vec{r}) \tag{4.1}$$

Solving this for $\phi(x)$, we arrive at the following differential equation:

$$-\frac{\hbar^2}{2m^*}\phi''(x) + [\frac{m^*\omega_c^2}{2}(x - x_0)^2 + U(x)]\phi(x) = (E - E_z)\phi(x) \tag{4.2}$$

where $\omega_c = eB/m^*$ is the cyclotron frequency, $E_z = \hbar^2 k_z/2m^*$ is the energy for motion in the direction of the field, and $x_o = -l_b^2 k_y$ corresponds to orbit centers with $l_b = (\hbar/eB)^{\frac{1}{2}}$ as the magnetic length. Also $U(x)$ is the underlying potential profile which would correspond to the well, tunneling barrier, and contact in our case.

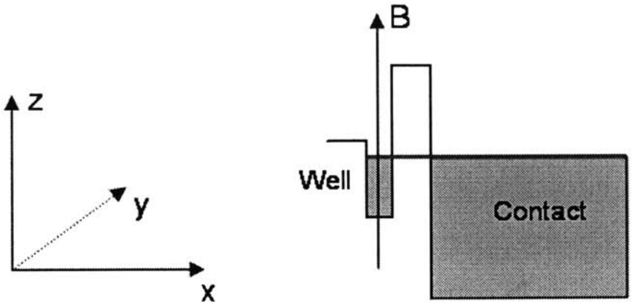

Figure 4-4: Coordinate system used. z is in the direction of the field, x is along the growth direction of the sample, and y is in the sample plane but perpendicular to the field.

We see from equation 4.2 that the effect of the field on the motion of the particle is to introduce a parabolic gauge potential, $m^*\omega_c^2(x-x_o)^2$, in addition to $U(x)$. However, $x_o = -l_b^2 k_y$, so x_o corresponds to k_y as well as orbit center. Thus, if we take k_z to be zero and plot E vs. x_o, we obtain a plot of energy and momentum. The procedure for carrying out such a calculation is graphically shown in Figure 4-6. In the figure, to compute the energy of the well at the orbit center position x_o' we consider the total potential of the well plus the corresponding gauge potential and solve for the eign-energy. The gauge potential can then be shifted along x_o to compute the energy of the well as a function of x_o. A similar procedure can be applied to the contact. Figure 4-5 from Lebens [3] shows the result when this operation is carried out in full for the well and contact.

Thus, for the well we see that the energy increases as the orbit center departs from the center of the well. We can see this as follows. At the origin we imagine the parabolic gauge potential on the well, and we see that the effect on the well is minimal. As we shift the gauge potential away from the well center, however, the total potential of the well and gauge rises to a higher offset and the composite basin is increasingly angled. This is shown in Figure 4-6. Thus we see that the effect of the gauge potential on the electrons in the well is to squeeze the electrons to the walls of the well. Since x_o corresponds to k_y, we intuitively imagine electrons in the well

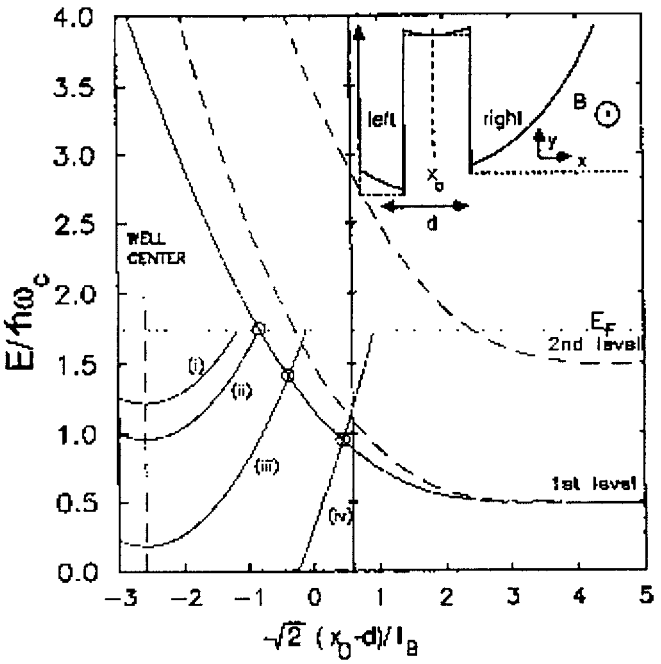

FIG. 3. Energies of electron located on right- and left-hand sides of the barrier as a function of $x_0(k_y)$. The potential profile that determines these energies is shown in the inset for a particular x_0 and field directed in the z direction. Dashed lines for first and second levels show the energy on the right-hand side for an infinite barrier and no band bending. The first level with corrections for these approximations is shown by the solid line. Four well densities, (i) 1×10^{11} cm^{-2}, (ii) 1.5×10^{11} cm^{-2}, (iii) 3×10^{11} cm^{-2}, and (iv) 6×10^{11} cm^{-2}, are depicted.

Figure 4-5: Energy vs. orbit center,x_o, dispersion relation. (Figure taken from Lebens [3].)

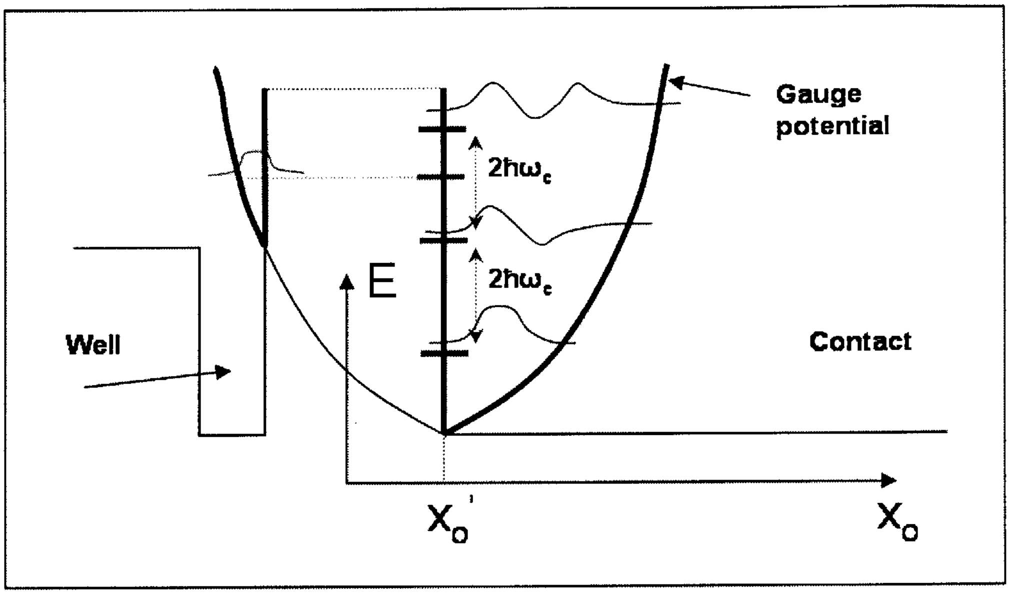

Figure 4-6: Calculations for the energy of the well and contact at x_o'. Only the first sub-band in the well is occupied so there is only one relevant energy for the well while there may be multiple levels for the contact.

with higher momentum perpendicular to the field being pressed harder against the well walls. Thus the energy rises as we depart from the well center as indicated in Figure 4-5.

A similar effect occurs in the contact. Deep within the contact the electrons only feel the effect of the gauge potential and they occupy landau levels. Thus the spacing in energy is given by $\hbar\omega_c$. As we consider orbit centers closer to the contact boundary with the tunneling barrier, the electrons begin to feel the effect of the boundary and the energy increases as shown in 4-5. Exactly at the boundary the effect of the gauge potential and the boundary edge is similar to half of a harmonic oscillator, where only the odd states of the total harmonic oscillator are solutions. Thus the spacing of the energy levels is $2\hbar\omega_c$ at the edge as shown in Figure 4-6. As we move further past the edge, the energy increases as interfacial electrons are squeezed into the edge. States which sufficiently effected by the edge correspond to classical skipping orbitals while those in the bulk correspond to classically orbiting electrons.

With the above considerations we are able to generate the energy vs. orbit center plots shown in Figure 4-5 [3]. Points of intersection correspond to states in the well and at the edge of the contact that have the same energy and momentum. If we were to draw a gauge potential at the orbit centers of the intersection points as was done in Figure 4-6,then the energy of the wave functions on the left and right would be the same. Because energy and momentum is conserved at the intersection points, tunneling can potentially occur at the Fermi level.

Figure 4-5 from Lebens [3] shows four different biases for the well. For the first case (i) the curves for the well and contact do not intersect below the Fermi level so tunneling does not occur. For the second case (ii) the curves intersect at the Fermi level so tunneling can occur. For the (iii) and (iv) case correspond to states below the Fermi level that are already occupied. Figure 4-5, however, only represents what is happening at $k_z = 0$. Thus, tunneling can occur for cases (iii) and (iv) with an orbit center indicated in the figure and a k_z that brings the energy up to the Fermi level. For each case (iii) and (iv) there are two such tunneling states, one of positive and one of negative k_z.

We are know in a position to interpret the data in Figure 4-1. Low densities correspond to situation (i) in Figure 4-5 where tunneling is not favorable. As we increase the density we arrive at a peak corresponding to case (ii) which falls off as we relay on states with greater k_z corresponding to case (iii) and (iv). As the field increases the curves in Figure 4-5 bend upward with greater concavity. We thus need a greater density to arrive at case (ii) and so the conductance peak shifts toward higher densities.

4.2 Analytical Presentation: Dispersion Relations

We now proceed to present the analytical equations or dispersion relations which approximate the tunneling problem. We begin by considering the expression for the total energy of electrons in the contact. This is given by the sum of the kinetic energy in the z-direction, which is unaffected by the field, and the component corresponding to the gauge potential and the contact edge.:

$$E(k_y, k_z)_{3D} = \frac{\hbar^2 k_z^2}{2m^*} + E_n(k_y) \tag{4.3}$$

To establish analytical equations for this problem, we need approximate solutions for the $E_n(k_y)$. For large x_o or a large k_y we know that then effect of the contact edge is not felt and then energy is given by $E_n(k_y) = \hbar\omega_c(n + \frac{1}{2})$. As x_o is reduced the effect of the contact edge is felt and the electrons occupy interfacial states. Interfacial electrons are those that correspond to classical skipping orbitals. The condition for an interfacial electron is that the orbit center is less than the orbit radius. If v is the orbital speed, then the kinetic energy of the electron is given by $E_n = \frac{1}{2}m^*v^2$ and the orbital radius is given by $r = v/\omega_c = (2E_n/m^*\omega_c^2)^{\frac{1}{2}}$. The condition for a interfacial state is then $X \leq r$, or:

$$X \leq \left(\frac{2E_n}{m^*w_c^2}\right)^{\frac{1}{2}}, or - \hbar k_y \leq (2m^*E_n)^{\frac{1}{2}}. \tag{4.4}$$

The above equation represents the boundary between interfacial states and bulk states. And is indicated in Figure 4-7 from Snell [6] by the dashed line.

An expression for the energy of an electron in the contact which conforms to the expected of bulk energies and interfacial energies as a function of k_y or orbit center position was calculated by Snell [6] using WKB. This expression was reported to be accurate to within 10% of the exact values. This expression is give by:

$$\frac{1}{2}\left[1 - \frac{\hbar k_y}{(2m^*E_n(k_y))^{\frac{1}{2}}}\right] E_n(k_y) = (n + \frac{3}{4})\hbar\omega_c, \tag{4.5}$$

$$n = 0, 1, 2, ...$$

Equation 4.3 and 4.5 are the main expression for calculating the energy and momentum dependence of electrons in the well. For simplicity we wish to express these

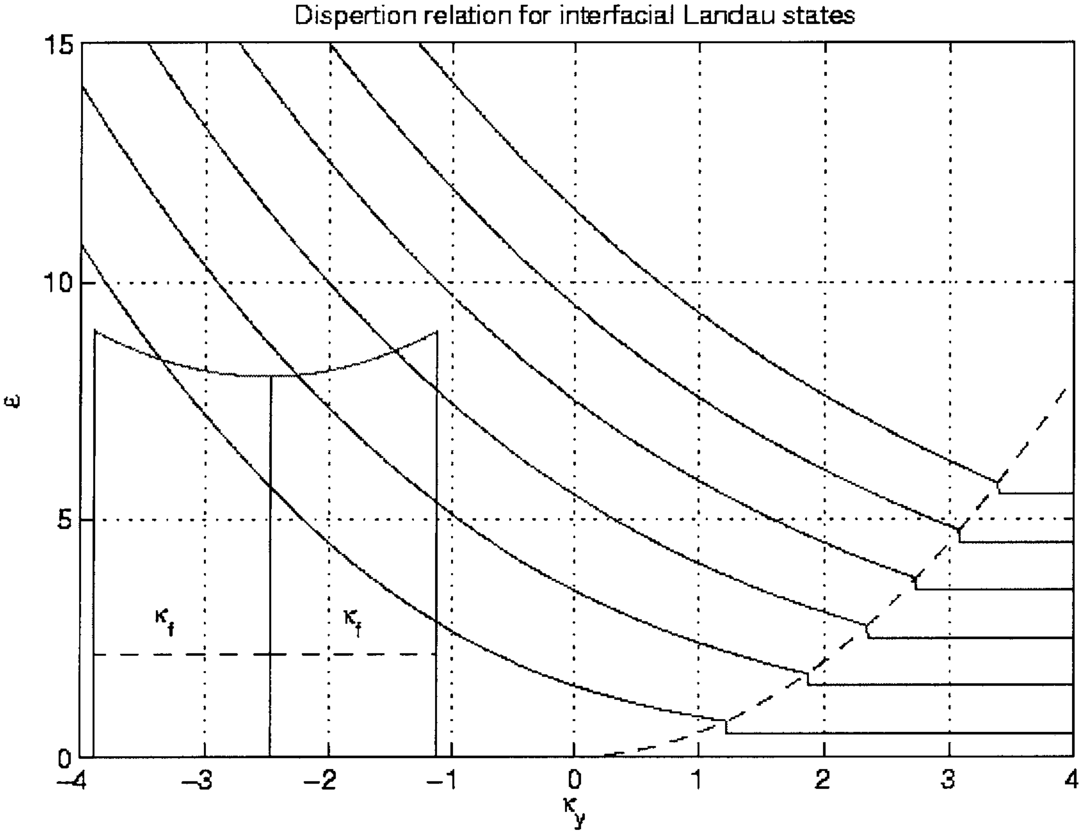

Figure 4-7: Analytical solution presented in normalize coordinates. The vertical axis is normalized energy ϵ, and the horizontal axis is κ_y, which is proportional to orbit center x_o. (Figure taken from Snell [6].)

equations in normalized coordinates as follows, respectively:

$$\epsilon(\kappa_y, \kappa_z)_{3D} = \frac{\kappa_z^2}{2} + \epsilon_n(\kappa_y) \tag{4.6}$$

$$\frac{1}{2}\left[1 - \frac{\kappa_y}{(2\epsilon_n(\kappa_y))^{\frac{1}{2}}}\right]\epsilon_n(\kappa_y) \;=\; (n + \frac{3}{4}), \tag{4.7}$$

$$n = 0, 1, 2, ...$$

In the above equations, we have $\kappa_z = l_b k_z$, $\kappa_y = l_b k_y$, $\epsilon(\kappa_y, \kappa_z)_{3D} = E(k_y, k_z)_{3D}/\hbar\omega_c$, and $\epsilon(\kappa_y)_n = E(k_y)_n$.

Equation 4.7 is plotted in Figure 4-7. For κ_y far to the left, which is negative in the chosen coordinates of the figure, the energy spacing in normalized units is approximately unity. However, close to the contact edge at zero we see that the spacing nearly doubles. We expect this doubling since, as stated earlier, then energies near the contact edge correspond to odd states of the harmonic oscillator. Thus we have reasonable expression for the contact electrons and we now turn to the electrons in the well.

The effect of the field on the electron in the well can be treated in perturbation theory to give the following result [6]:

$$E_{2D}(k_y, k_z) = \frac{\hbar^2 k_z^2}{2m^*} + \frac{\hbar^2(k_y - k_o)^2}{2m^*} + eV \tag{4.8}$$

where $k_o = eB(b + a_o)/\hbar$, b is the barrier width, and a_o is the mean distance of a bound electron from the contact edge. Also V is the applied bias. One thing to note is that $\hbar k_0$ is just the momentum shift due to the Lorentz force as an electron traverses the barrier. The above equation can be expressed in normalized units as follows:

$$\epsilon_{2D}(\kappa_y, \kappa_z) = \frac{\kappa_z^2}{2} + v\frac{(\kappa_y - \kappa_o)^2}{2} \tag{4.9}$$

where $\kappa_o = (b + a_o)/l_b$, $\epsilon_o = E/\hbar\omega_c$, $v = eV/\hbar\omega_c$ and the other quantities are as previously defined.

The above dispersion relation, equation 4.9, is plotted in Figure 4-7. The states of transverse momentum are occupied up to the Fermi energy $E_{FL} = \hbar^2 k^2/2m^*$. Thus only a curve is shown extending by κ_{KL} in both directions from the base of the well. The point of intersection with the curves for the contact are denoted as circles and are of interest as they conserve both energy and momentum. Tunneling occurs at the Fermi level with $k_z = 0$ whenever the contact curves intersect the end points on the segment. Each intersection below the segment correspond to two tunneling events with a positive and negative momentum, k_z.

As the field or the density of the well changes the curves shift past over one another and the contact curves enter end exit the end points of the well curve. These two processes of entering the well and exiting correspond to the sets of oscillations noted in Figure 4-2 and 4-3.

4.3 Energy Contours in Momentum Space

Equations 4.6, 4.7, and 4.9 constitute the dispersion relations for the electrons in the well and the electrons in the contact. These equations are functions of momentum ($\kappa_x - \kappa_y$) and energy (ϵ_{3D} and ϵ_{2D})). Thus we are able to plot constant energy contours of the two systems in a two-dimensional momentum space as indicated in Figure 4-8. Intersection of constant energy contours in the momentum space correspond to intersections in the plots of the dispersion relations as was done in the previous section, however the momentum contour plot provide a clearer description of in-plane field tunneling.

Figure 4-8 is an example of a constant energy momentum contour plot corresponding to the dispersion plot 4-5. The constant energy contours for the electrons in the well satisfy the equation:

$$\epsilon_{2D}(\kappa_y, \kappa_z) - v = \frac{\kappa_z^2}{2} + v\frac{(\kappa_y - \kappa_o)^2}{2} \tag{4.10}$$

And are thus circles in the momentum plane centered at κ_o and with a radius of

$\sqrt{2(\epsilon_{2D} - v)}$. Thus for various biases we expect concentric circles at κ_o as shown in the Figure 4-8.

The contours for the contact are slightly more complicated to produce. For orbit centers deep within the contact the electrons are not significantly effected by the contact edge and thus occupy Landau levels with constant energy and level spacing. A particular low level Landau level can, thus, be brought to the Fermi level by adding energy from the $+/-\kappa_z$ component. The lowest level would require the greatest $\kappa_z^2/2$ contribution to be brought to the Fermi level and subsequent levels of higher energy would require less. Landau levels of energy greater than the Fermi energy would entirely be unoccupied as no amount of κ_z^2 could bring the energy to the Fermi level.

As shown in Figure 4-8, the above is reflected in the momentum contour plot since κ_y is proportional to orbit center position. Thus for large κ_y where electrons occupy the Landau energies, $(n+\frac{1}{2})$[1], κ_z is independent of κ_y. Furthermore the outer horizontal curves corresponds to the lowest Landau levels, and unoccupied landau levels of energy greater than the Fermi level are not shown.

As κ_y is shifted to the left, the effect of the edge on the energy of the Landau levels comes into effect. In the dispersion relation of Figure 4-5 the effect of the edge causes the Landau level energies to rise as the orbit center runs into the contact edge. The overall effect is that as the effective offset energy of the Landau levels increases, the required κ_z momentum contribution required to be at the Fermi level decreases. Thus in momentum space the constant energy at $+/-\kappa_z$ bend toward the horizontal axis until they meet. Thus, the formed U shaped curves in Figure 4-8 correspond to different Landau levels of the contact.

---

[1] The Landau energies in normalize units are $(n+\frac{1}{2})$.

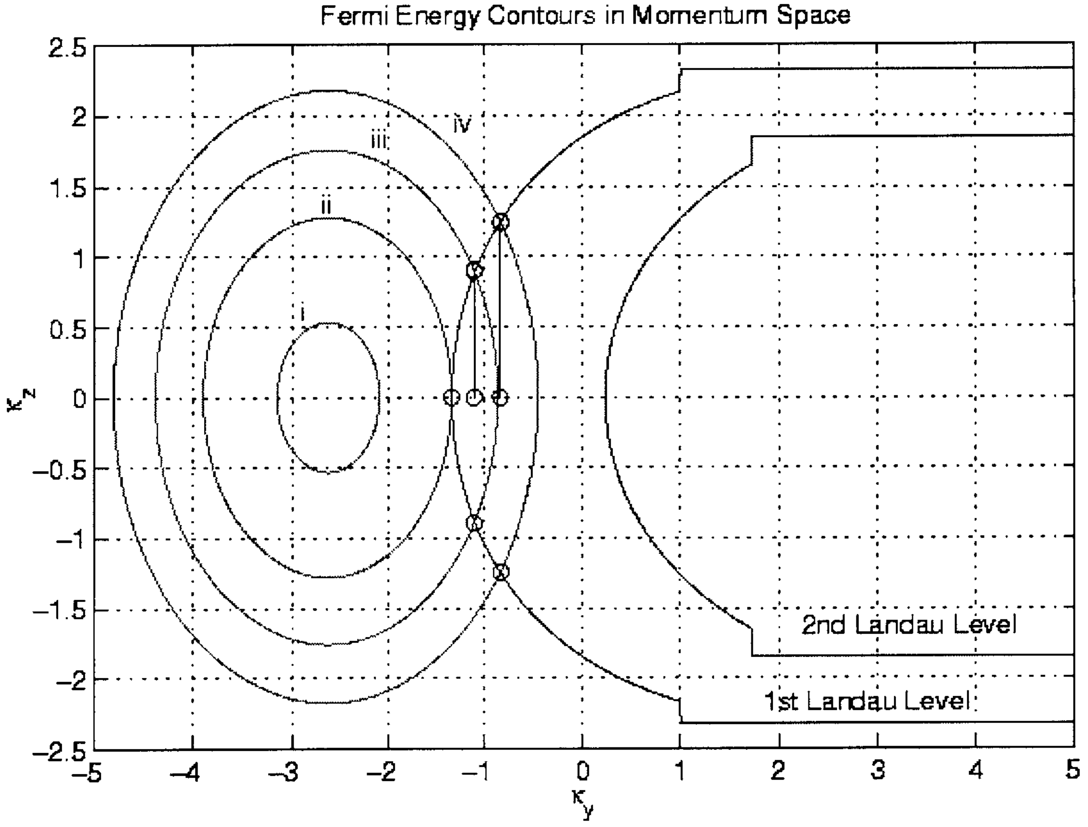

Figure 4-8: Constant energy contours for the electrons in the well for different biases, and for the electrons in the contact for different Landau levels. The horizontal axis κ_y is proportional to orbit center position, x_o, and the vertical is κ_z, where z is along the field direction.

4.4 Effect of varying field and density on tunneling conductance

Intersection in the momentum contours correspond to intersections in the dispersion contours and thereby reflect increases in the tunneling conductance. Figure 4-8 shows the effect of varying the density on the tunneling conductance. The four cases shown correspond to the four cases in Figure 4-5. In the first case no tunneling is allowed at the Fermi energy. The second case corresponds to tunneling at kz=0. For the next two cases we have tunneling event at positive and negative κ_z. We can see that for case three and four that while the dispersion intersection in Figure 4-5 indicated tunneling events of positive and negative momentum, the momentum contour plot shows all the events. Thus the momentum contour plot is useful to identify all tunneling events.

The effect of sweeping the field is shown in Figure 4-9. The arrows indicate that as the field is swept the circle shrinks and shifts to the left while the Landau levels are drawn to the right and eventually vanish consecutively as the field is increased. This motion can be understood from how the increasing field effect the dispersion curves for the well and the contact. For the well the parabolic dispersion curve increases in curvature and shifts to the right. The increase in curvature causes the extent of κ_f, the well Fermi vector, to reduced. Thus in momentum space, the ellipse contracts and shifts as indicated in the figure.

For the contact, as the field is increased, the Landau level energy separation is increased and the curvature for the interfacial energies increases. The increased curvature causes less penetration of electrons into the contact edge and therefore causes the vertical edge of the U-curves to fall at shallower $kappa_y$ points. Also the increased Landau level separation, causes the vertical portions to contract to the horizontal axis as less κ_z^2 is required to bring the landau level to the Fermi level. Higher Landau levels eventually vanish as the energy of the corresponding Landau levels begin to exceed the Fermi level. The overall effect indicated by the arrows is achieved. Furthermore entry of and departure of the U portions onto the ellipse correspond to the oscillation in Figure 4-2 and 4-3 discussed previously.

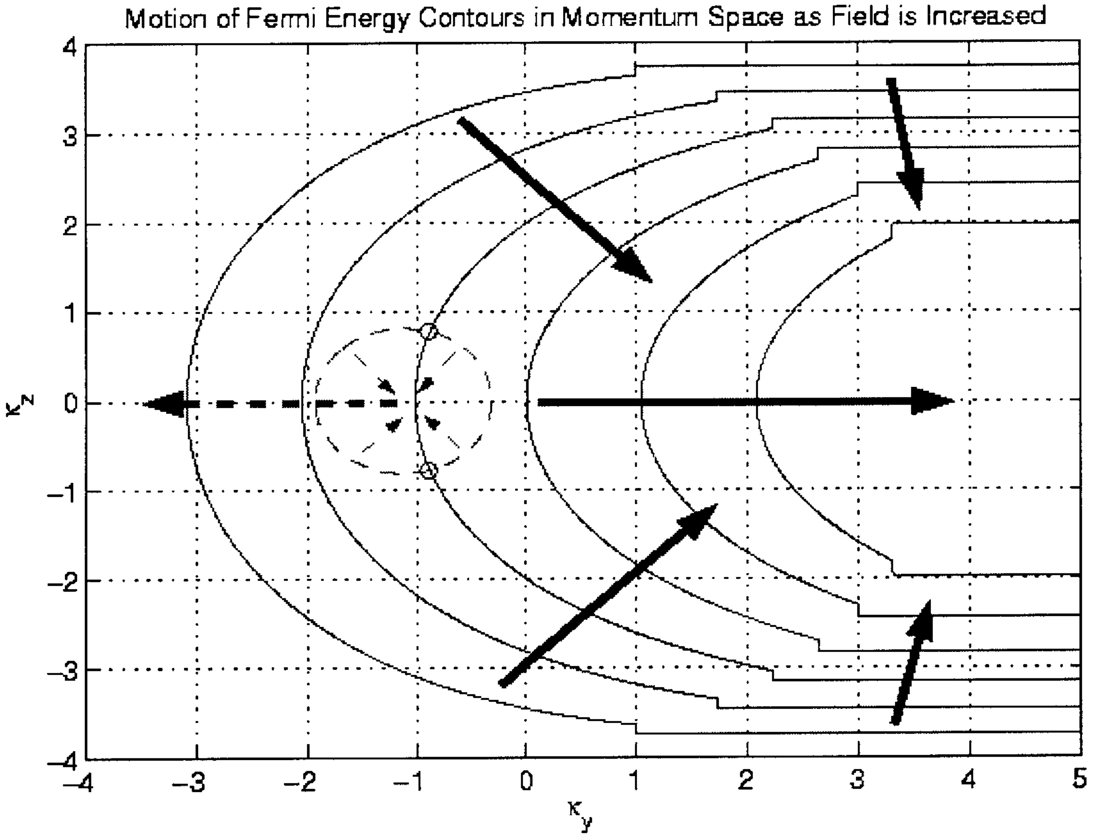

Figure 4-9: The arrows indicate the effect of sweeping the in-plane field in the momentum contour space. The horizontal axis κ_y is proportional to orbit center position, x_o, and the vertical is κ_z, where z is along the field direction.

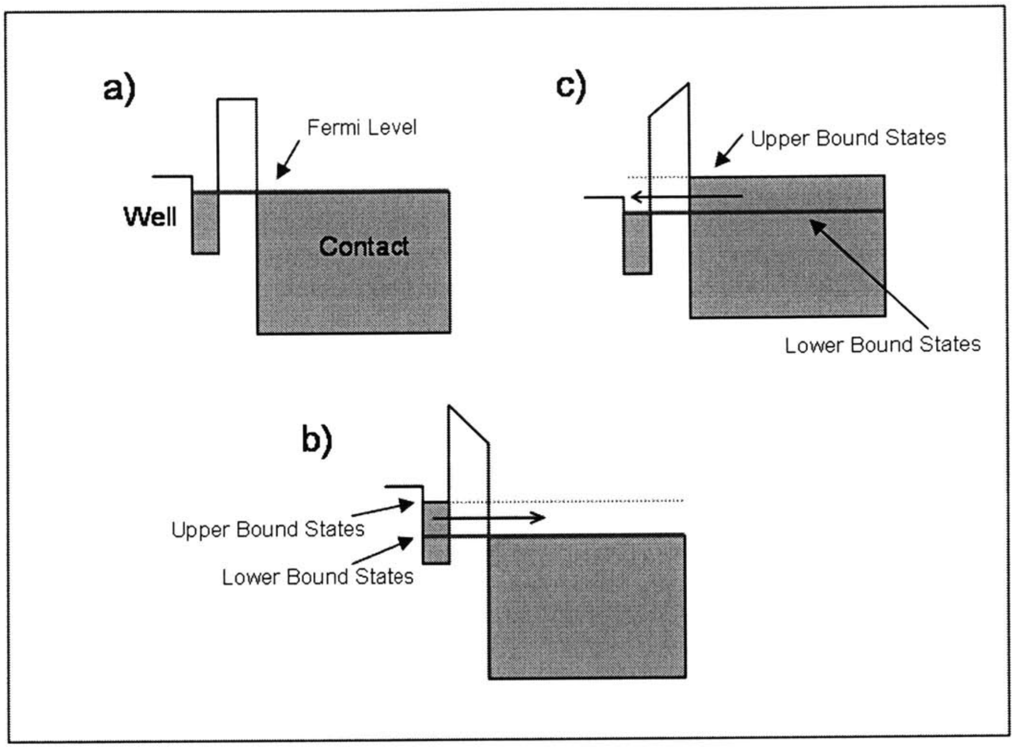

Figure 4-10: Inset a) indicates the band structure of the sample at equilibrium, inset b) shows the sample after a positive excitation, and inset b) shows the sample after a negative excitation. The upper bound and lower bound states of interest are shown.

4.5 Effects of Tunneling out of Equilibrium

One of the advantages of the tunneling experiment is that it allows us to study out of equilibrium effect and therefore we wish to discuss such effect regarding in-plane tunneling. The momentum contours provide the most accessible means of discussing the out of equilibrium response of a sample to a step excitations. Figure 4-10 depicts the sample response to positive and a negative excitation in terms of the energy diagrams, and Figure 4-11 and 4.5 show the corresponding events in momentum space. To identify tunneling points in momentum space we first draw constant energy contours in momentum space, and then find their intersection. By sweeping constant energy contours and tracing out the points of intersection, we can identify all the tunneling events. We first discuss the response to a positive excitation.

Before the excitation we are at equilibrium as indicated in Figure 4-10 a. The solid curves alone in Figure 4-11 indicate the appropriate energy contour in momentum space. After the excitation we are interested in how electrons in the well tunnel into available states in the contact. As shown in Figure 4-10 b, the excitation causes a band of occupied states to tunnel into the well. Thus the excitation makes available a band of energies in the contact into which tunneling is possible. In particular we focus on the upper bound states and the lower bound states indicated in Figure 4-10 b. The electrons in the upper bound states in the well tunnel into unoccupied states above the Fermi level in the unperturbed contact. Electrons in the lower bound states in the well, however, tunnel at the Fermi level in the unperturbed contact. Electrons in the well with intermediate energies tunnel into empty states with intermediate energies in the well.

The contours for the lower bound and upper bound states in the well are drawn in Figure 4-11. The solid circular contour represents the upper bound states which are the highest occupied energy states in the well. These states were at the Fermi level of the contact before the excitation and now have an energy that exceeds the Fermi level of the contact. The dashed circular contour represents the lower bound states which are the lowest occupied energy levels of interest in the well. Before the excitations these states were below the Fermi level of the contact. The positive excitations, however, elevated their energy to match the Fermi energy of the contact.

The contours for the corresponding contact states are also drawn in Figure 4-11. The solid U-shaped contours corresponds to states in the contact at the Fermi level, while the dashed U-shaped contours corresponds to empty states in the contact at a higher energy level that matches the energy level of the upper bound in the well indicated in Figure 4-10 b. Thus, tunneling can occur at the intersection of the dashed circular contour and solid U-shaped ones, and at the intersections of the solid circular contour and the dashed U-shaped ones.

To identify tunneling at energies between the lower and the upper bound states, we need to draw the appropriate contours for the well and contact and identify the points of intersection. In other words, tunneling at intermediate energies can be visualized by tracing out the intersections as we increase the contour energy from that of the

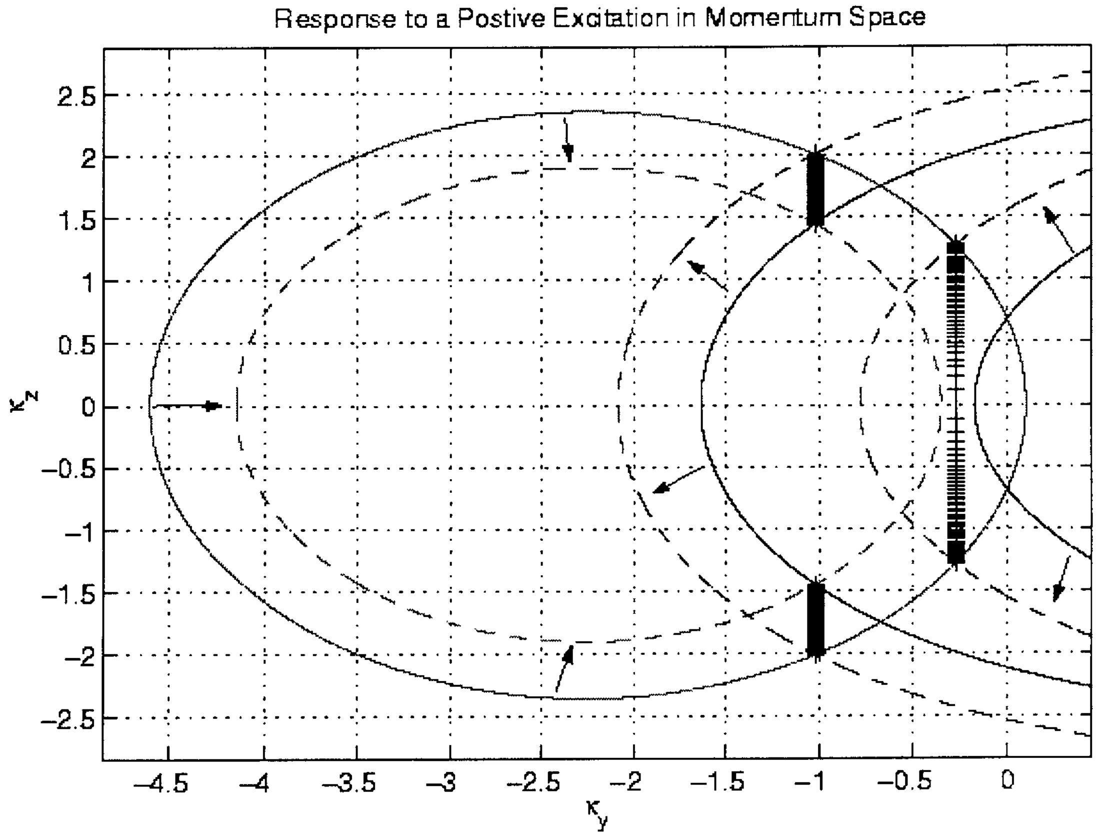

Figure 4-11: Response to a positive excitation in momentum space. The lines formed by the + signs were generated by simulation and indicated the momentum of electrons that tunnel from the well to the contact with the band of energies made available by the excitation. In other words, electrons in states located on the vertical line represent all the allowed tunneling transitions between the well and the contact. Each point indicated by a + was computed by finding the intersection between a circular contour (well) and a set of U-shaped contours (contact) for the energies between the lower bound and upper bound states indicated in Figure 4-10 b. See text for further explanation of the figure.

dashed circle and the solid U-shaped curves to that of the solid circle and the dashed U-shaped curves. In this view we can imagine the dashed circle dilating onto the solid one and the solid U-shaped curves expanding onto the dashed ones. If we were to keep track of the movement of the points of intersection during this process, we would find that they trace vertical lines as indicated in Figure 4-11[2]. These vertical stripes correspond to the momentum of allowed tunneling states with energies in the band opened up by the pulse. Electrons in states located on the vertical line represent all allowed tunneling transitions between the well and the contact.

Thus to summarize, the process of a positive excitation can be viewed as starting in equilibrium at the solid lines in Figure 4-11. After the excitation the energy of the solid circular contour changes and the dashed lines represent new curves of interest. The dashed circle is at the Fermi level of the contact while the dashed U-shaped curves are above the Fermi level of the contact. The dashed circle pushes in from the solid circle while the dashed U-shape curves push out from the solid ones. This motion is indicated by the arrows in Figure 4-11. We then can draw vertical lines from the intersection of the solid circle and the dashed U-shape curves to the intersection of the dashed circle and the solid U-shape curves. These represent the allowed tunneling transition states in the contact and well with the energies opened up by the positive pulse.

For negative pulses a discussion similar to the above can proceed. The main difference is now electrons tunnel from the contact to the well. Thus we are concerned with highest energy electron in the contact that can tunnel into the well, and the lowest energy electrons that can tunnel, which are at the Fermi level of the unperturbed well. These electrons are indicated in the band diagram in Figure 4-10 c. We can then draw corresponding contours and locate intersection points as was done above. The main difference, as shown in Figure 4.5, is that now we image the dashed circle pushing out from the solid one, and the dashed U-shape pulsing in from the solid on. This is indicated by the arrows in Figure 4.5. We can then determine the corresponding intersections and draw the appropriate stripes. These vertical lines represent the allowed tunneling transition states in the contact and well for the energies opened up by the negative pulse.

---

[2] The arrows in the figure refer to the application of the pulse as will be explained below and not the calculation of the vertical lines as discussed in the referred paragraph

4.6 Tunneling Conductance as a function of Excitation Height

On possible signature of in-plane field tunneling effects is the increase in tunneling conductivity as a function of excitation height. This is illustrated in Figures 4-13, 4-14, and 4-15. Here we see that for small excitation no tunneling occurs. Large excitations, however, enable tunneling into the first Landau level. This happens for both positive and negative excitations as indicated in the figures. If we were to increase the excitation height further the contributions from the next Landau level would then be seen. Thus, measuring the tunneling conductance as a function of excitation height can reveal the underlying Landau structure of the contact and the tunneling measurement can be used to probe the structure of the states in the contact.

4.7 Experimental Results

In this section we present some of our experimental findings. All of the data was taken at around $270mK$. Figure 4-16 and 4-17 show some preliminary results. Figure 4-16 show the relative conductance vs. in-plane field for various biases. Our aim in producing such a curve was to locate oscillation in 1/B. We were unable to observer them, however, since the level of noise masked any time of fine structure in the data. The plot of relative conductance vs. bias for different fields, however, in Figure 4-17 produced the expected results. Here we see the conductance shifting to higher densities and broadening as reported by Snell [3]

Figure 4-18 shows a highly resolved curves of conductance vs. bias for various applied fields. We were able to achieve such resolution by improving the grounding scheme of the setup and also the fitting algorithm. We are now doing a least squares

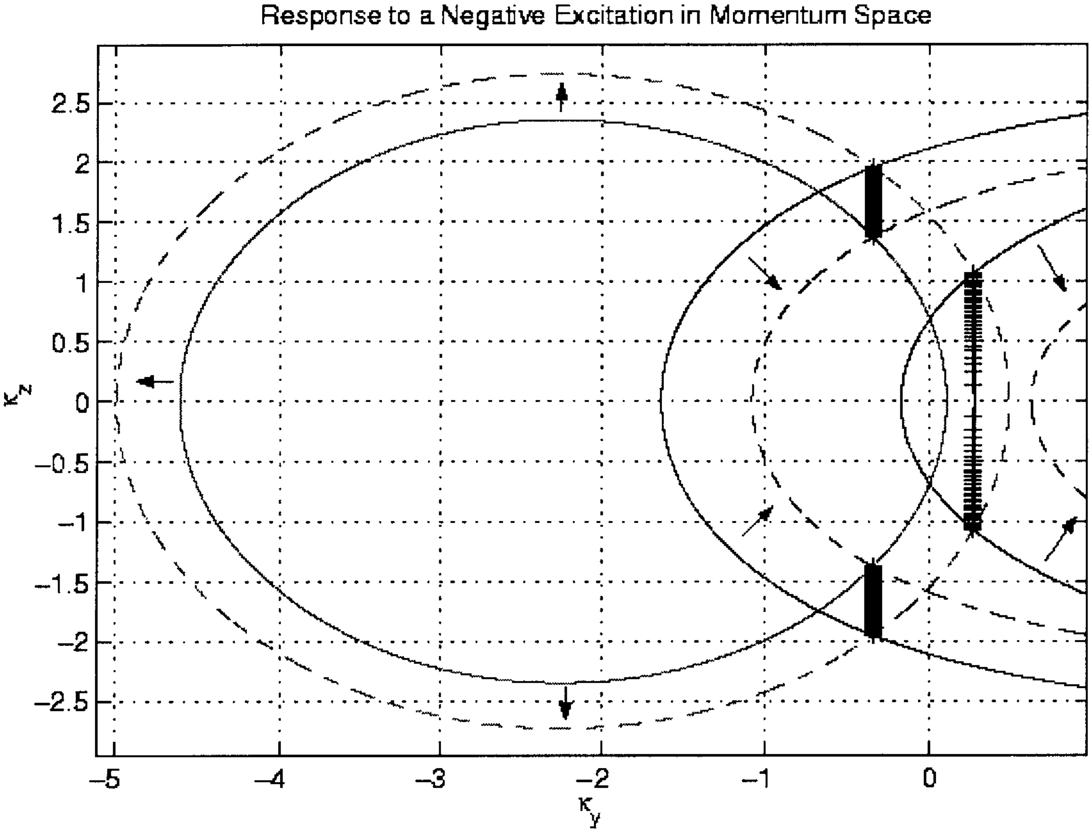

Figure 4-12: Response to a negative excitation in momentum space. The lines formed by the + signs where generated by simulation and indicated the momentum of electrons that tunnel from the contact to the well with the band of energies made available by the excitation. In other words, electrons in states located on the vertical line represent all the allowed tunneling transitions between the well and the contact. Each point indicated by a + was computed by finding the intersection between a circular contour (well) and a set of U-shaped contours (contact) for the energies between the lower bound and upper bound states indicated in Figure 4-10 c. See text for further explanation of the figure.

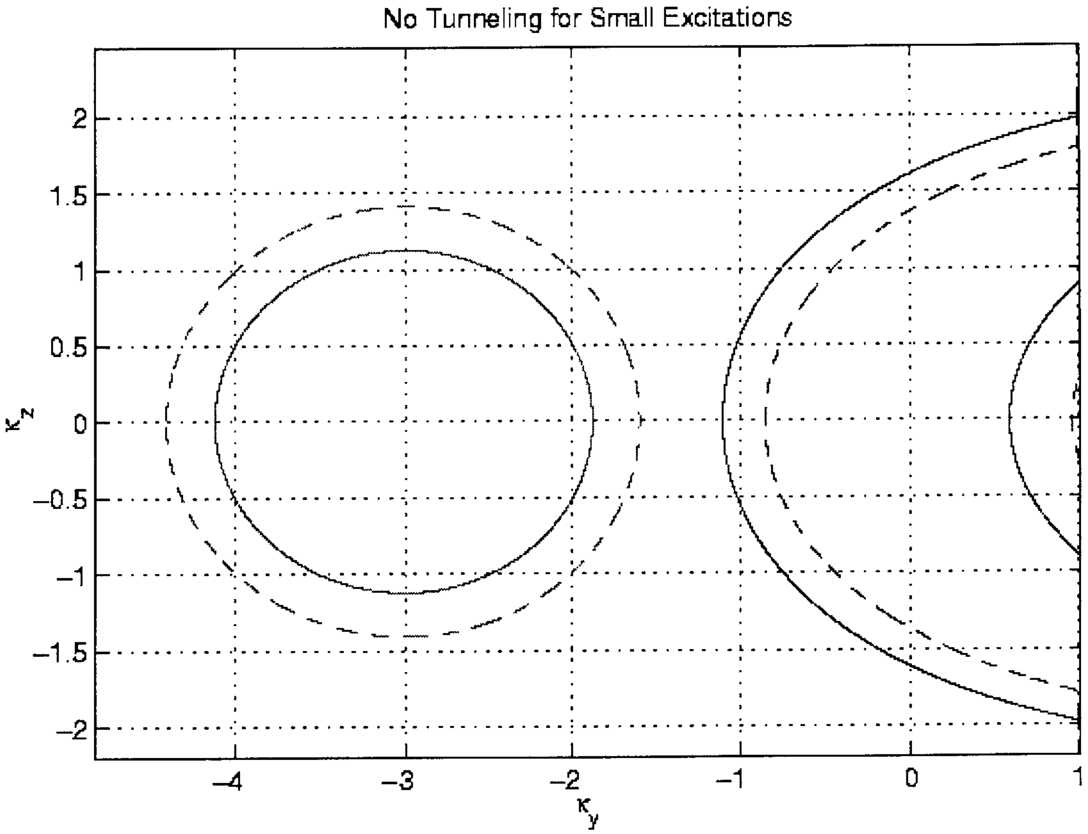

Figure 4-13: There is no overlap between contours of the well and contact as no tunneling occurs.

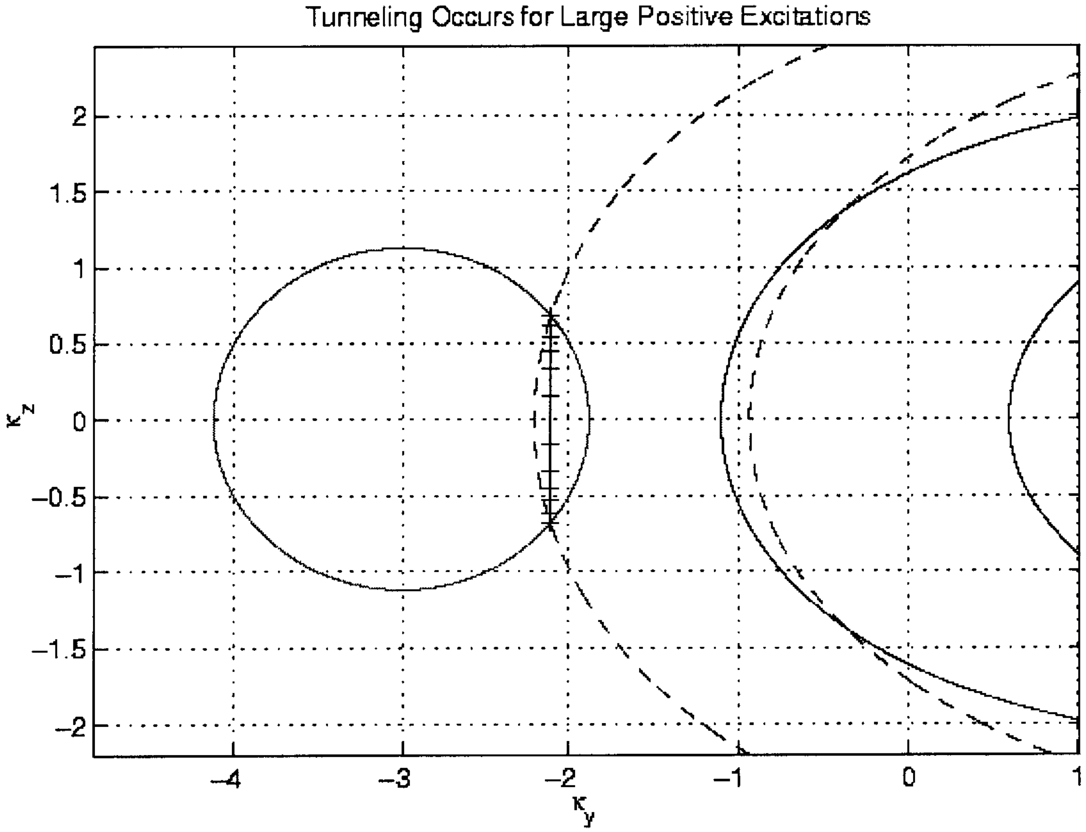

Figure 4-14: Large positive excitations open up overlap to allow tunneling to occur. Electrons in states located on the vertical line represent all allowed tunneling transitions between the well and the contact.

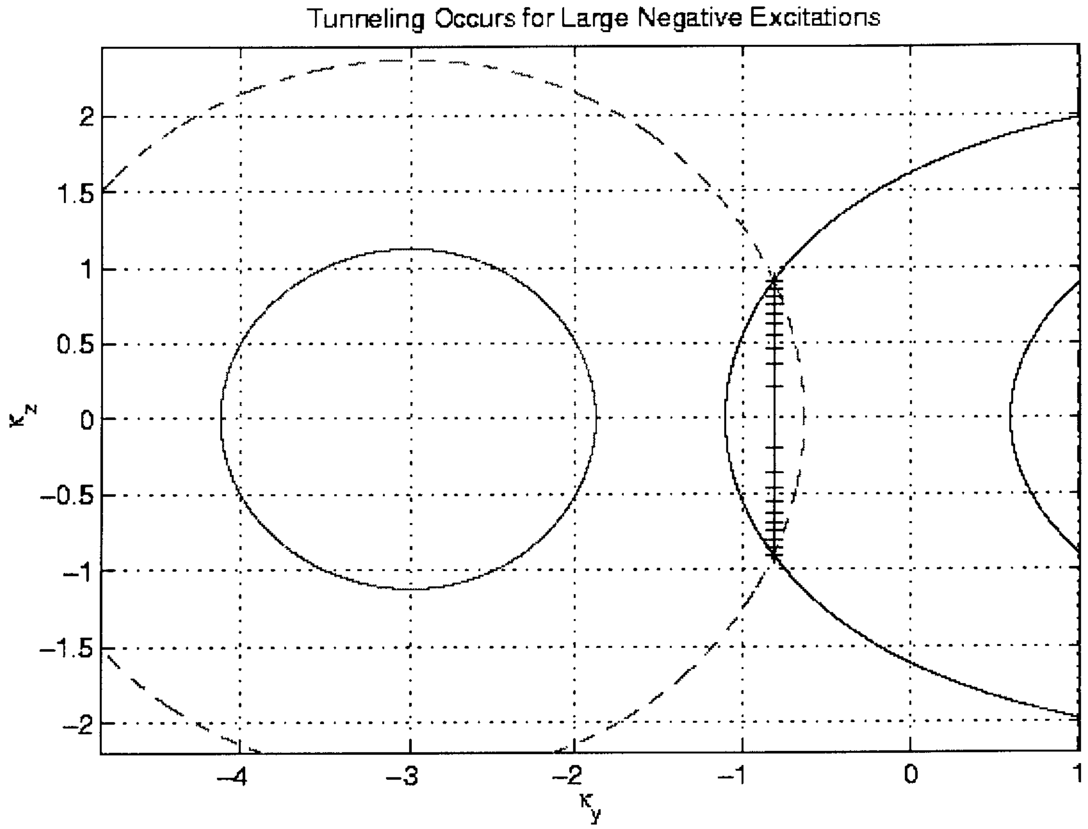

Figure 4-15: Large negative excitations open up overlap to allow tunneling to occur. Electrons in states located on the vertical line represent all allowed tunneling transitions between the well and the contact.

fit using an exponential as a fitting function. The dimples on the curves corresponded to a bit error in a bias box and was fixed on subsequent traces.

Figure 4-19 is again another curve of relative conductance vs. sample bias. However the range of sample biases has greatly increased in this data. For larger fields (4Tesla) and higher biases (500mV) we observe what could amount to the appearance of another landau level. It is not clear, however, if this second bulge is from in-field Landau level formation, or if it is due to an undesired perpendicular field that arose from a tilt in the rotation stage. One should not though that the stage was rotated to within the accuracy of the rotation mechanism and the hall sensor.

Figure 4-20 show the relative conductance vs. sample bias for different excitation heights. The excitation heights scale by factors 2 4 8 and 30, and the plots are normalized. The relative conductance for positive and negative excitations are shown. For small excitations no change in the curves are noticed. The curves corresponding to the largest excitation heights which are the largest in the plot only seem to smooth out the general shape for positive excitations and distorts the general shape for negative excitation. More analysis is required to understand what is happening.

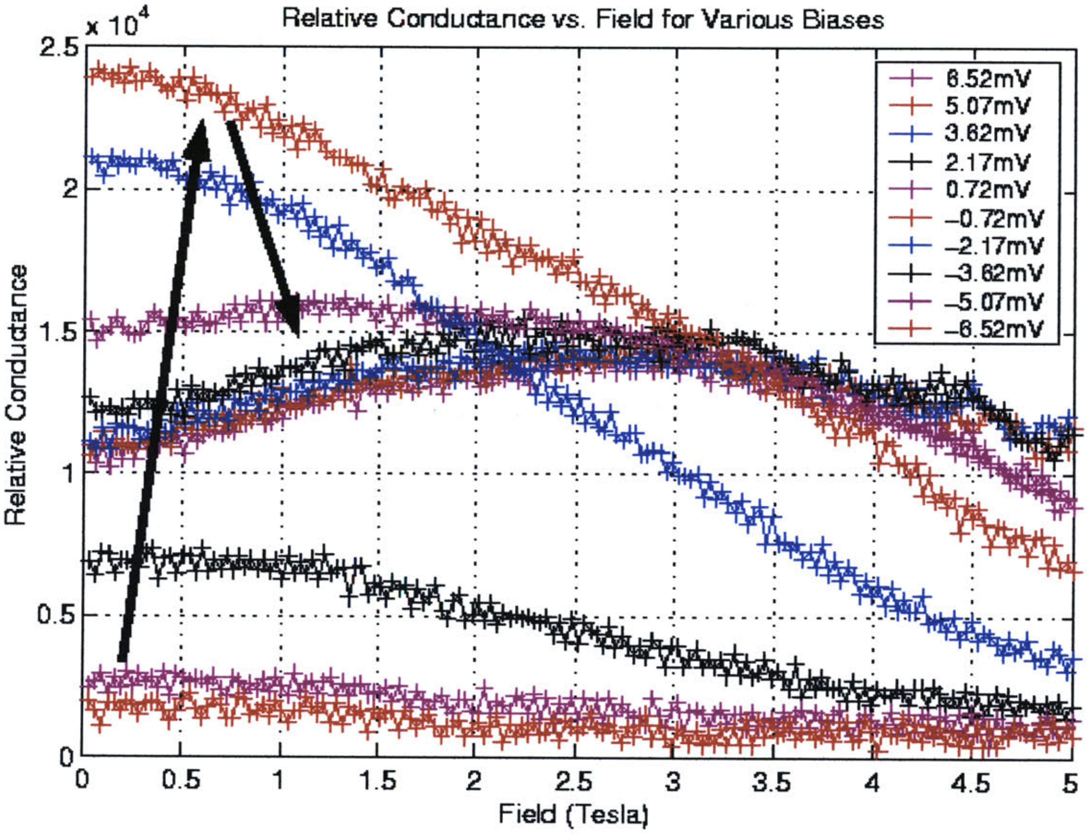

Figure 4-16: Relative conductance vs. field (Tesla) for different biases. The biases across the sample are shown in the legend. The excitation amplitude across the sample is 120mV. The arrow shows how the curve changes as we go from depletion (-6.52mV) to accumulation (6.52mV).

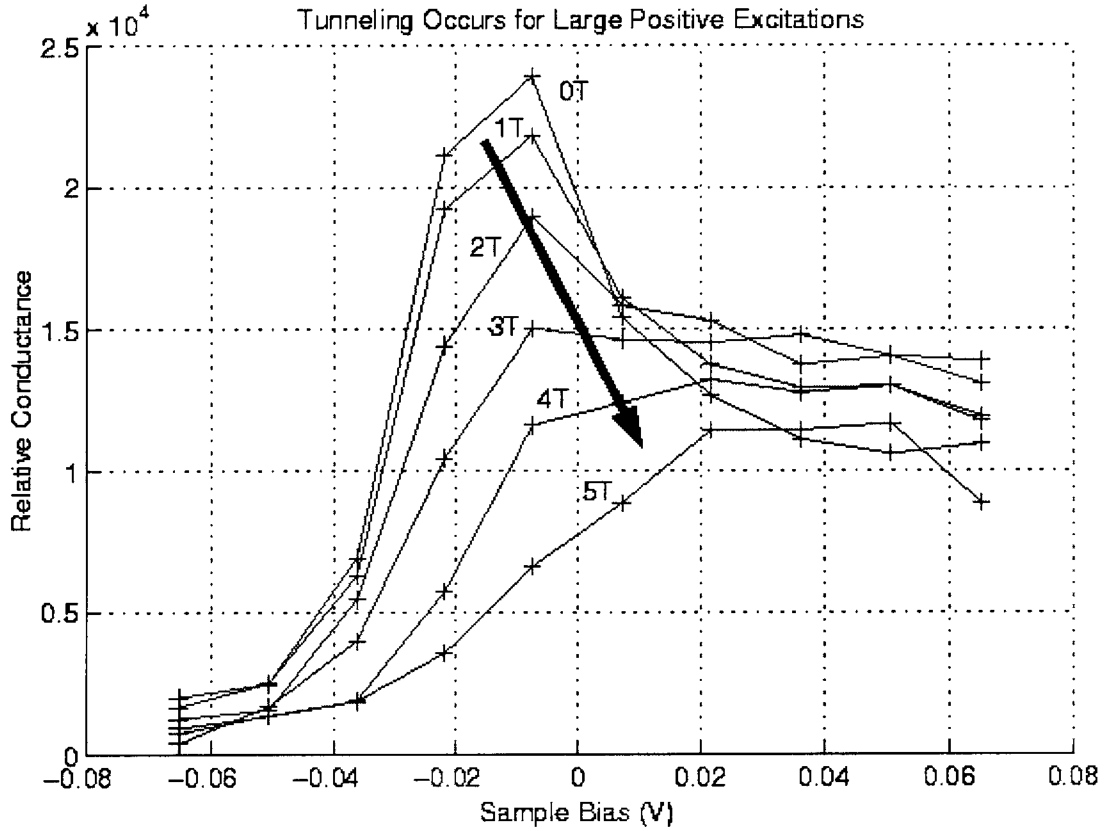

Figure 4-17: Relative conductance vs. bias (V) for different fields and from the data taken from Figure 4-16. The fields are indicated in the figure and are reported in Tesla. The excitation amplitude across the sample is 120mV. The arrow shows how the curve changes as we vary the field from 0 Tesla to 5 Tesla.

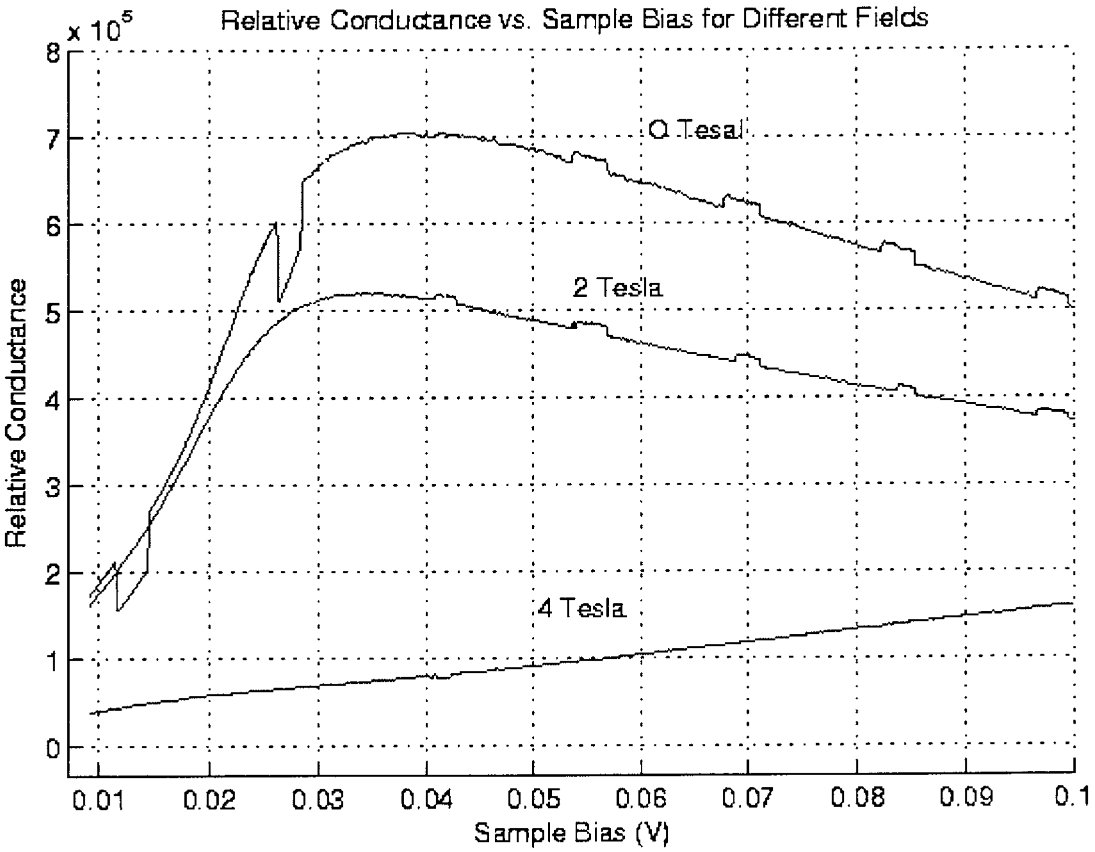

Figure 4-18: Relative conductance vs. bias (V) for different fields. The excitation height applied across the sample is 10mV. The steps in the above data are due to bit errors in the voltage box applying the bias voltage. The error was fixed immediately after this data was collected and so doesn't appear for subsequent data. In previous data we fitted a line to the initial points of the data to extract the initial slope. In this data we fitted least squared exponentials and thus greatly improved the fits as can be seen by comparing the noise in the above data to that of Figure 4-16.

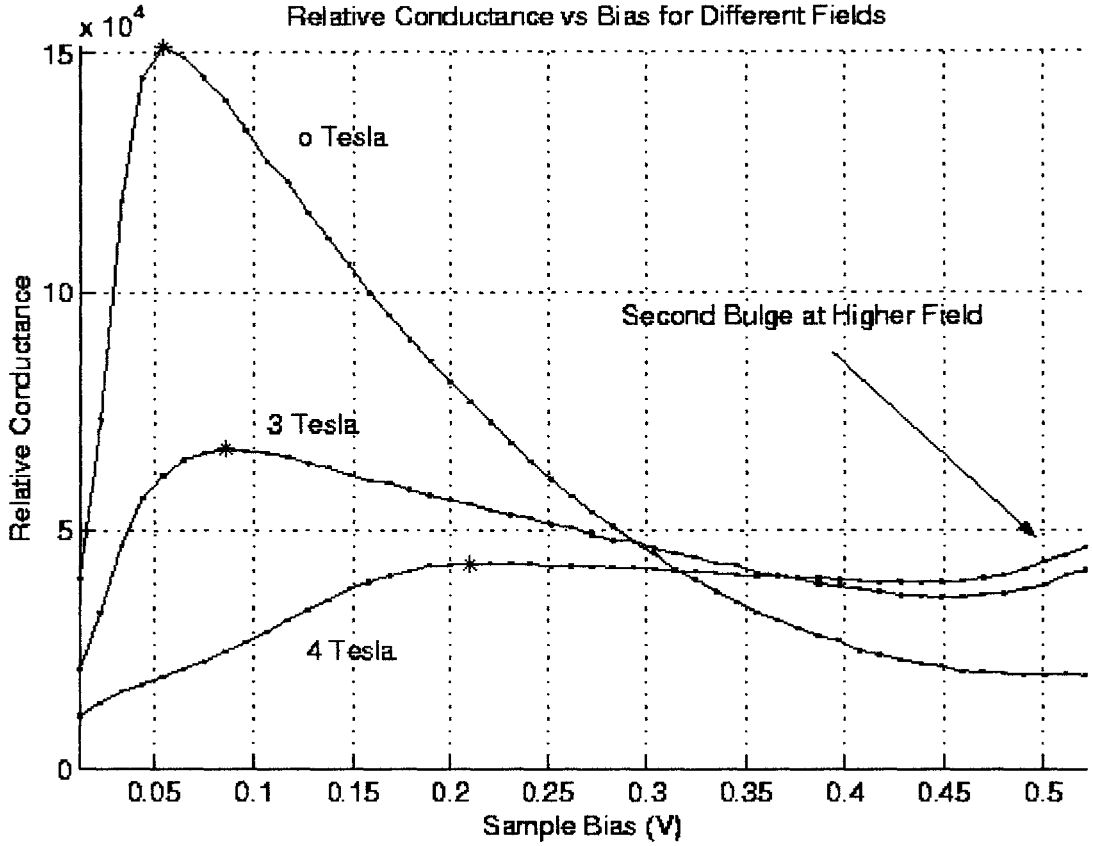

Figure 4-19: Relative conductance vs. bias (V) for different fields. The excitation height across the sample is 2mV. A second bulge is observed in the data.

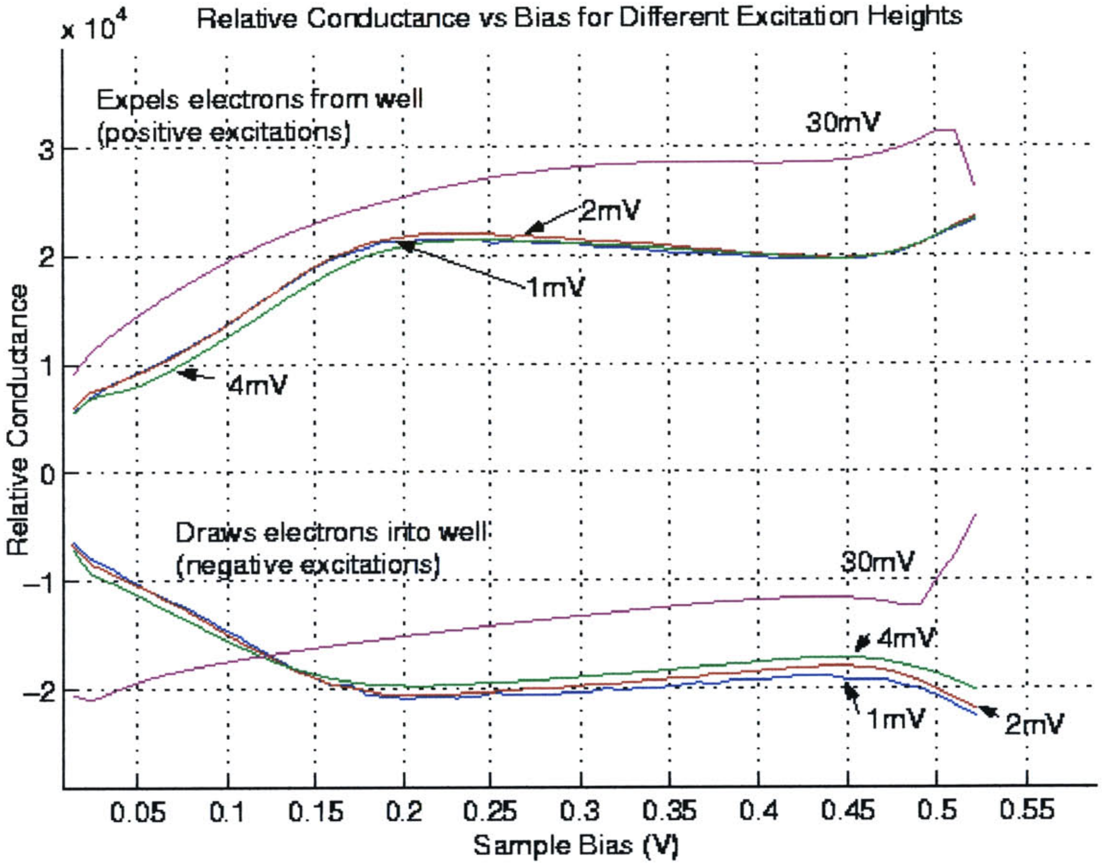

Figure 4-20: Relative conductance vs. bias (V) for different excitation heights. The excitation heights and pulse directions are indicated in the figure.

Chapter 5

Conclusion and Future Work

In conclusion, we have presented theoretical models and experimental data in this thesis to understand the tunneling process in the presence and absence of an in-plane field. We were able to successfully demonstrate that equilibrium and out of equilibrium data for the zero-field tunneling regime. However, more work needs to be done for the in field case.

Judging by the smoothness of the data presented in this chapter, it seems reasonable that the oscillator effects associated with in-plane tunneling would be within the experimental precision of the apparatus. The fact that such oscillations were not observed in a satisfactory manner suggests that the problem may lie with the sample itself.

In the sample construction, there is an doping spike in the blocking layer that provides electrons for the quantum well. This layer may create non-uniformities in the potential of the well or contact that act to broaden the Landau peaks. The net effect would be that the expected oscillatory behavior would be smoothed out and unobservable. It would be desirable in future experiments to use sample with a cleaner construction.

Appendix A

Pulse Shaper

A main technical challenge in increasing the resolution of the experiment is to produce sample and standard capacitor excitation signals of the forms indicated in Figures 2-7a and 2-7b of high fidelity over a broad dynamic range. The previous circuit implementations for generating these waveforms were limited by slow transient responses in the excitation output. In this section we discuss an innovative pulse generation scheme[1] which is able to circumvent the problems associated with the former circuit implementation.

A.1 Pulse-Shaper as the New Generator of Excitations

The original excitation waveforms were generated with an HP8131A amplifier and an analog multiplier to allow for precision control of the amplitude. The multiplier limited the precision of the measurement due to a slow $10\mu s$ transient responses in the output associated with step input excitations. In the new scheme a simple pull up output stage consisting of a high speed FLUMX10 transistor replaces the analog multiplier stage. This stage eliminates the slow step response and therefore increased

---

[1] Much thanks to Oliver Dial for coming up with the circuit concept discussed in section A.1 and A.2.

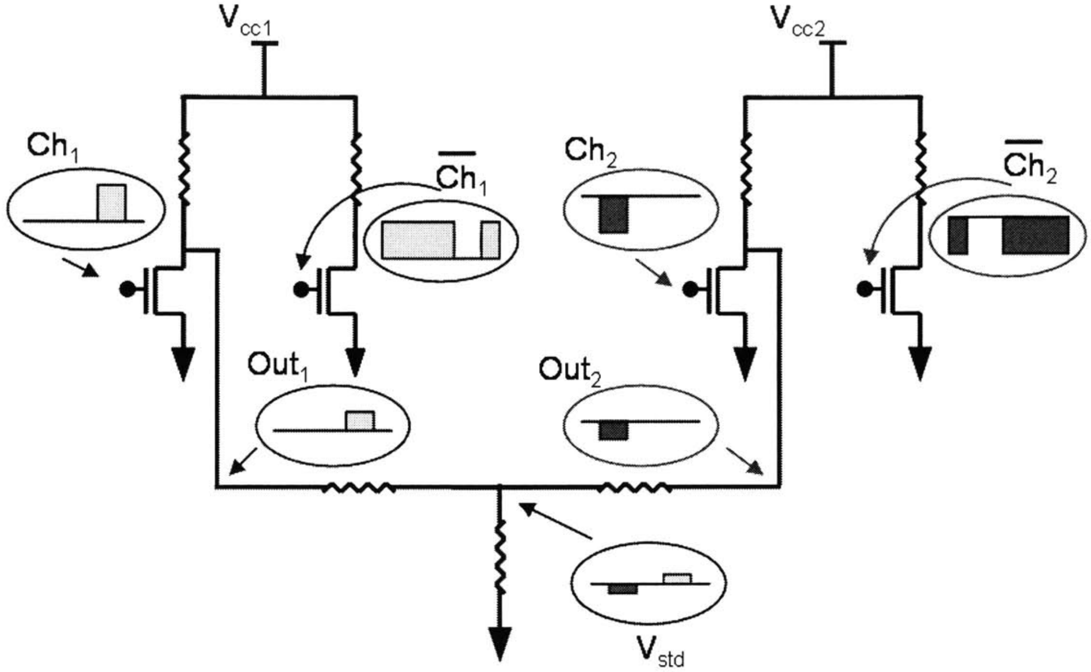
V_{cc1}
V_{cc2}
Ch_1
$\overline{Ch_1}$
Ch_2
$\overline{Ch_2}$
Out_1
Out_2
V_{std}

Figure A-1: Schematic for the pulse generation for the standard capacitor excitation.

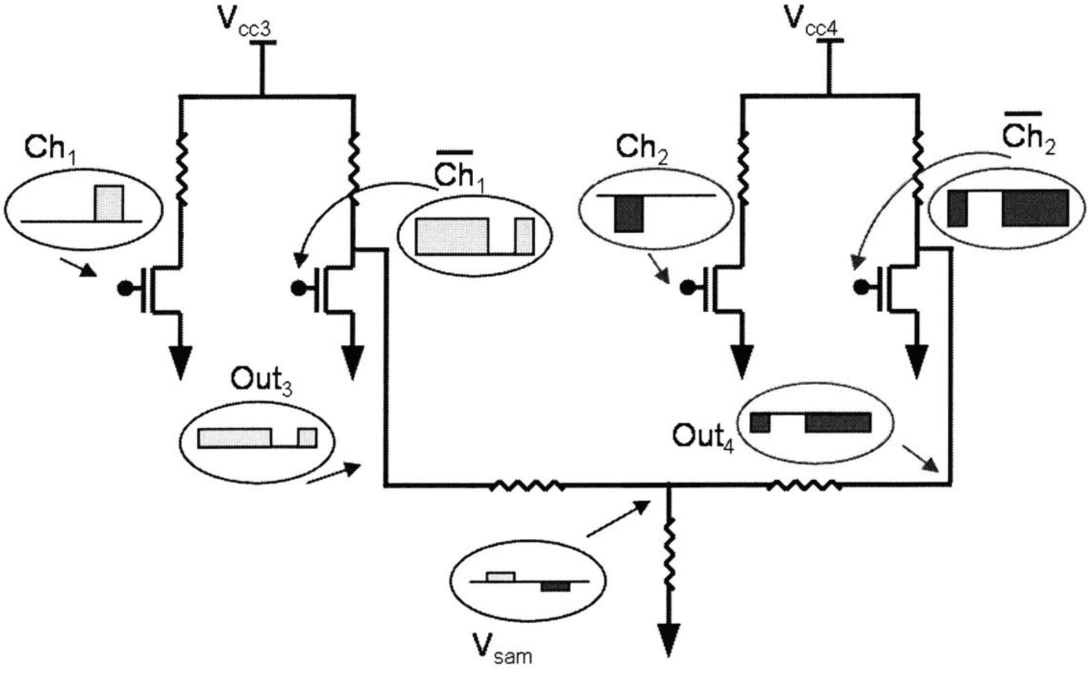
V_{cc3}
V_{cc4}
Ch_1
$\overline{Ch_1}$
Ch_2
$\overline{Ch_2}$
Out_3
Out_4
V_{sam}

Figure A-2: Schematic for the pulse generation for the sample excitation.

the resolution of the experiment.

A simplified schematic of the *pulse shaper* is show in Figure A-1 and A-2. The circuit is used in conjunction with the HP8131 pulse generator which is dual channel and has complementary outputs. In the figure, Ch_1 and $\overline{Ch_1}$ denote the output and complementary output of channel one. The waveforms are complementary in the sense that if summed the resulting waveform will be constant. Similarly Ch_2 and $\overline{Ch_2}$ denote the output and complementary output for channel two. The generator itself cannot be used for balancing as it doesn't have well resolved amplitude control of the output pulses. The pulse shaper provides the more accurate control of amplitude.

The basic circuit element is a pull up transistor that is run from both rail voltages, ground to the supply voltage. The HP8131 output is feed to the gate and the output is taken from the drain. Precision control of the amplitude is achieved by changing the upper supply voltage. In addition to the pull up transistor used to generate the signal, another pull up transistor is used as a compensation element. Compensation is achieved by feeding the complementary output to the gate. That way one of the two transistor will be on and the other will be off at any given time and the supply voltage will see a constant impedance.

Two transistors can produce a one pulse per period excitation in the sense that per period the output can only have one fall and one rise. The overall output waveform however has both a positive pulse and negative pulse which entail two falls and two rises. The total output waveform is then generated by summing two time shifted and reverse amplitude pulses generated by the above mentioned two transistor scheme. Thus a total of four transistors are used. In the next section we explain in more detail how the output waveforms are generated in Figures A-1 and A-2.

A.2 Explanation of the Circuit Implementation

As discussed above the total output waveform has one positive and one negative pulse per period. The total waveform is produce by summing two time delayed and opposite amplitude pulses. Each of these pulses is in turn generated from a circuit scheme which employs two pull up transistors. One functions as a compensation element and the output is taken from the drain of the other.

As previously mentioned, Figure A-1 shows how the excitation to the standard capacitor is generated. The two transistors on the left form half of the total output signal. We see that the fixed amplitude inputs of Ch_1 and $\overline{Ch_1}$ are feed to the gates. If Ch_1 and $\overline{Ch_1}$ were summed together then the total would be a constant voltage. This ensures that one of the two drains is on while the other is off at all times and we are able to achieve compensation. The half output, Out_1, is taken from the drain of the far left transistor whereas the other transistor serves as the compensation element. The pulse shape of Ch_1 is reflected in the drain output Out_1, but the overall amplitude is controlled by V_{cc1}. In a similar way the two transistors on the right, which are controlled by Ch_2 and $\overline{Ch_2}$, act together to as a compensated circuit to produce the other half output Out_2. V_{cc2} controls the output for Out_2

The total output, V_{std}, which has positive and negative pulse halves, is show in Figure A-1. Since Out_1 and Out_2 each have the correct pulse shape but with opposite amplitudes, and are time delayed, the proper form of the output waveform V_{std} is achieved by just summing the two through the resistive network. We are thus able to have a signal of the required shape excite the standard capacitor. The signal amplitude of the pulses in the output waveform are robustly controlled by V_{cc1} and V_{cc2} which are usually tied together to ensure a symmetric output waveform.

The sample excitation is similar to the standard capacitor excitation, except that its amplitude is inverted. This is reflect in the circuit implementation for the sample excitation in Figure A-2. The inputs to the gates of the four transistors (Ch_1, $\overline{Ch_1}$, Ch_2, $\overline{Ch_2}$) are the same as in the standard excitation circuit, but the drain voltages, V_{cc3} and V_{cc4} are different to ensure independent amplitude control for the sample excitation. These voltages are also typically tied together.

The main difference of the sample excitation circuit is that the outputs, Out_3 and Out_4, are taken from the transistors that are fed the complementary outputs at their gates. One can see how the waveforms combine to give the correct output shape for V_{sam}, by considering $\overline{Ch_1}$ to be negative of Ch_1 but with a DC offset, and similarly for $\overline{Ch_2}$. Out_3 and Out_4 have the same profiles as $\overline{Ch_1}$ and $\overline{Ch_2}$, so when they are summed the DC offsets vanish and we are left with an inverted version of the corresponding waveform at V_{sam}. Thus, with these two circuits we are able to achieve the two desired sample and standard capacitor wave forms.

A.3 Incorporation of the HP11713A Variable Attenuators

The above pulse shaper gives high fidelity pulses for a limited dynamic range, however. This is the case since if the drain voltage falls below 1V the transistor is unable to stabilize at a good pinch off point. The output signal the becomes distorted. This limit of dynamic range was overcome by incorporating two HP 1GHz variable step attenuators. The attenuator had 11 attenuation level evenly spaced from 0dB to 110dB. Thus, we used the computer controlled variable attenuators to broaden the dynamic range.

Using the variable pulse generators gave us two parameters to determine the output pulse height, attenuation factor and drain voltage. For the range of interest, the waveform amplitude is a linear function of drain voltages, and increases with drain voltage. A great deal of calibration data was collected to accurately describe this linear relation. Also the attenuation level accurately attenuate the amplitude without changing the dependence on drain voltage.

The optimal combination employed the criterion of achieving the target voltage height using largest possible drain voltage, with a maximum of 10V. Thus to achieve a given intermediate waveform amplitude, we could eliminate lower attenuation settings which would require too low of a drain voltage, and also higher attenuation settings which would require drain voltages in excess of 10V. The ideal setting would be the attenuation setting with the highest drain voltage not in excess of 10volts.

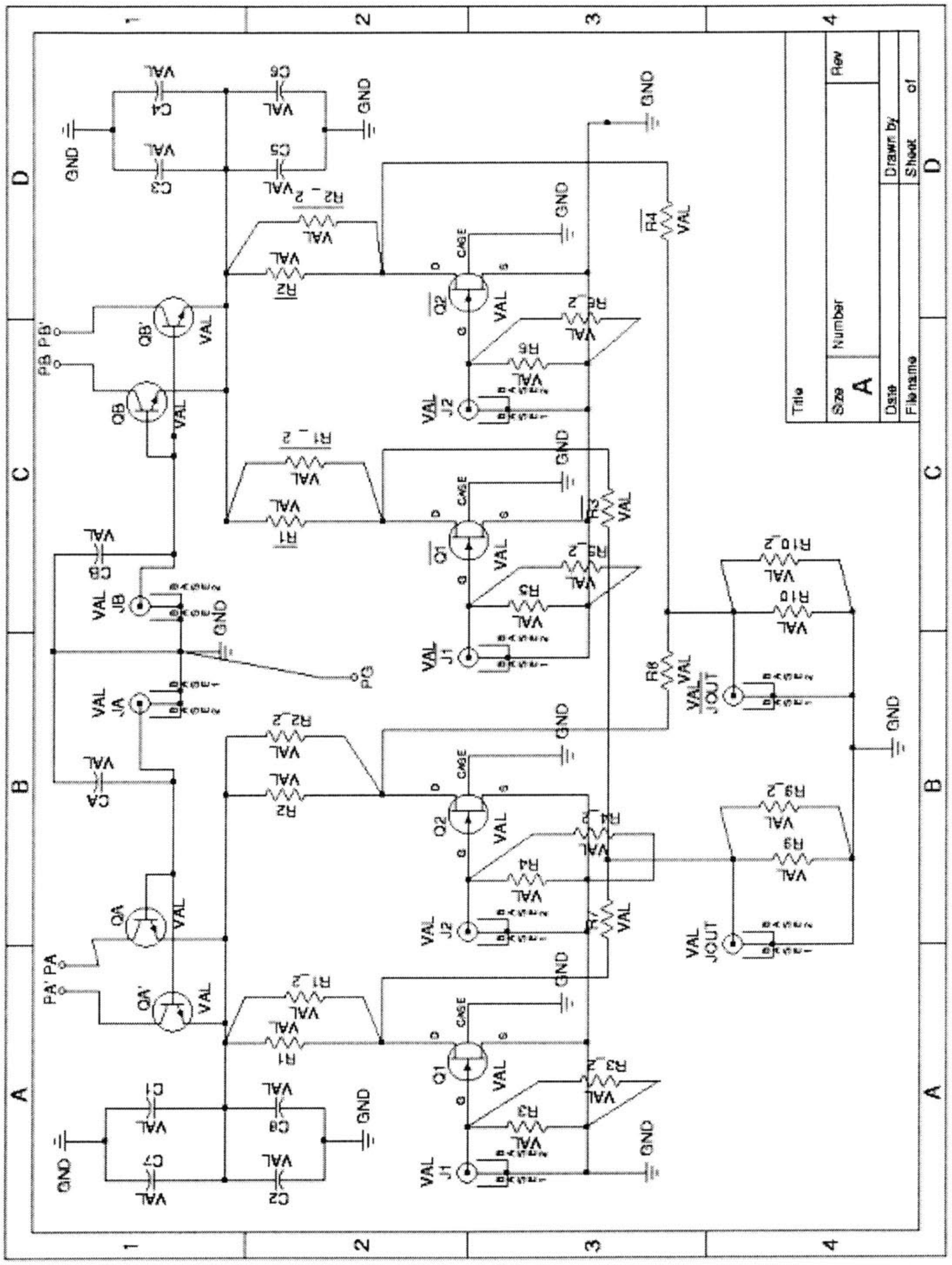
A
B
C
D
1
2
3
4
GND
VAL
C1
C2
C3
C4
C5
C6
C7
C8
CA
CB
QA
QA'
QB
QB'
PA' PA
PB PB'
JA
JB
PG
J1
J2
Q1
Q2
R1
R1_2
R2
R2_2
R3
R3_2
R4
R4_2
R5
R5_2
R6
R6_2
R7
R8
R9
R9_2
R10
R10_2
JOUT
D
G
S
CASE
Title
Size
A
Number
Rev
Date
Filename
Drawn by
Sheet
of

Figure A-3: Schematic for the Pulse Shaper circuit used to adjust pulse heights.

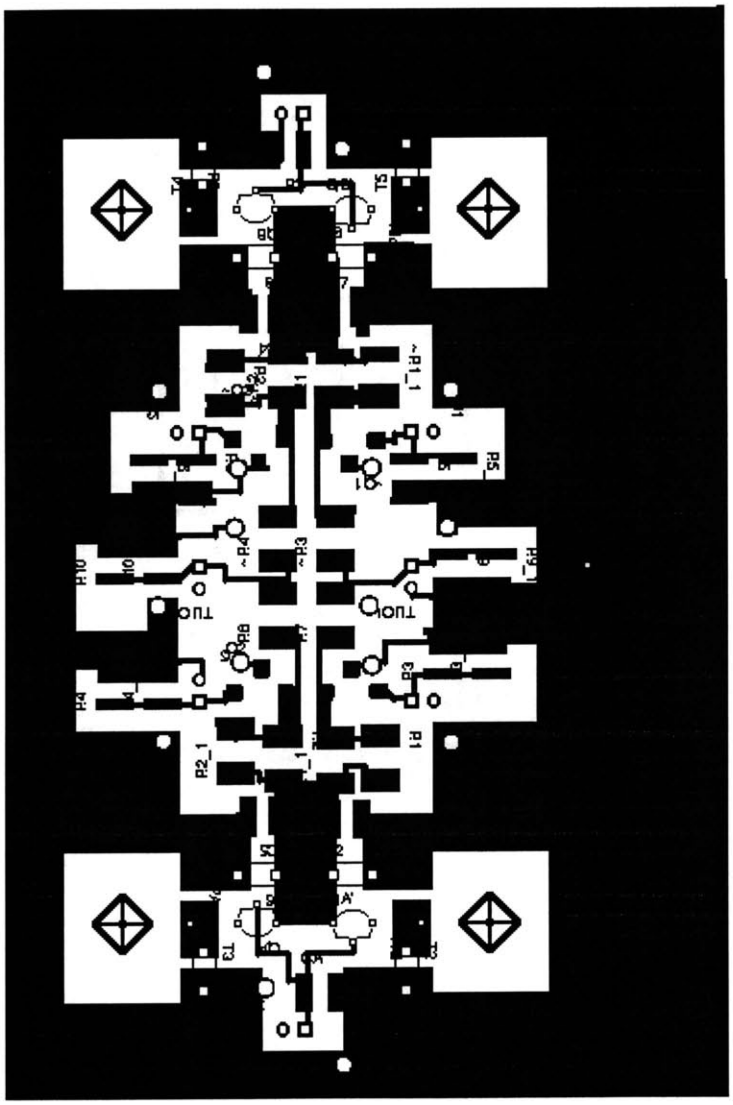

Figure A-4: Schematic for the printed circuit board of the pulse shaper.

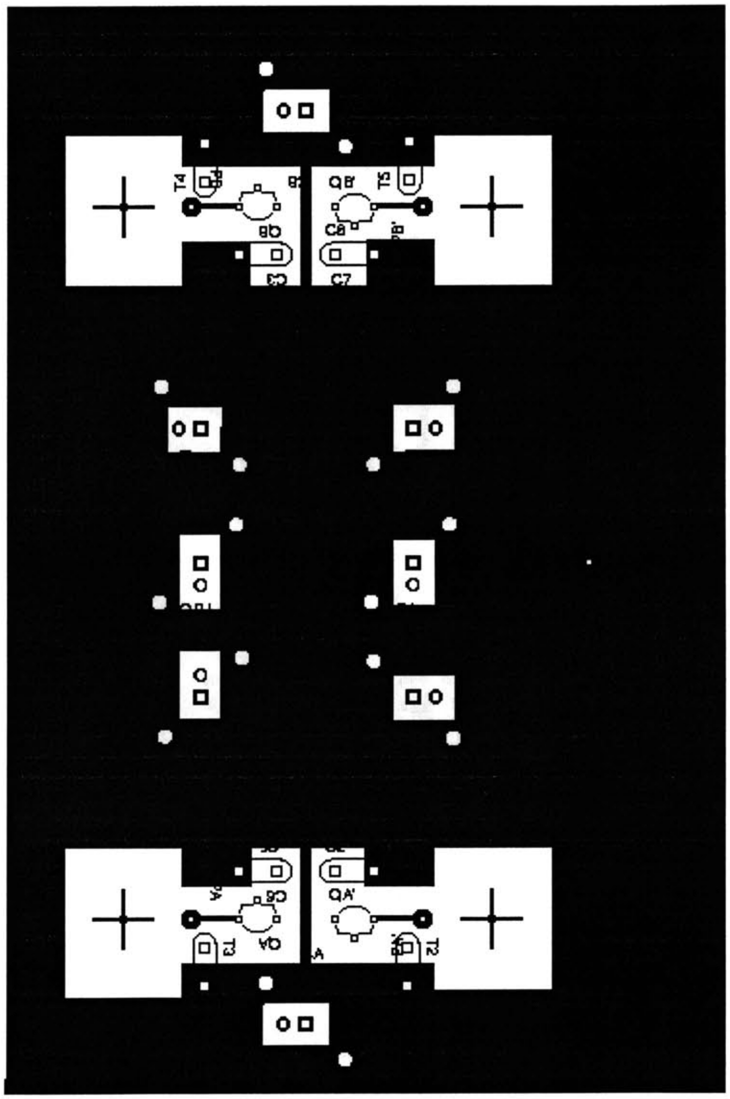
T4
QB'
T5
C8
C7
QA'
T2

Figure A-5: Schematic for the printed circuit board of the pulse shaper.

A.4 Printed Circuit Board

In order to optimize the pulse shaper performance, the circuit was implemented on a printed circuit board. The detailed schematic is shown in Figure A-3. There we can see that 50Ω resistors were placed on the gates of the transistors and at the output point to ensure proper termination. Also stabilizing capacitors are were placed at all DC voltage locations including the V_{cc} point, which indicates that after changing the excitation high one show wait for transients to settle.

Figures A-4 and A-5 show the printed circuit board implementation of the pulse shaper circuit. The board was laid out on two layers and was designed for compactness in order to minimize stray capacitance which could delay rise times and degrade the overall performance of the circuit. Also the board was designed to have nearly all the elements on one side of the board, allowing the other side to serve as a grounding plane. This ensures that the circuit has been designed to minimize stray capacitance and is well grounded.

Bibliography

[1] Raymond C. Ashoori. *The Density of States in the Two-Dimensional Electron Gas and Quantum Dots.* PhD thesis, Cornell University, 1991.

[2] Ho Bun Chan. *Tunneling Spectroscopy of the Two-Dimensional Electron Gas.* PhD thesis, Massachusetts Institute of Technology, 1999.

[3] John A. Lebens. Effect of a parrallel magnetic field on tunneling in GaAs/$\mathrm{Al}_x\mathrm{Ga}_{1-x}$As heterostructures. *Physical Review Letters*, 59:2806–2809, 1987.

[4] John A. Lebens. Tunneling and transverse wave vector conservation in gaas/algaas heterostructures. *Appl. Phys. Lett*, 51:840–842, 1987.

[5] John A. Lebens. *A Study of Tunneling Phenomena in Gallium Arsenide-Aluminum Gallium Arsenide Heterostructures.* PhD thesis, Cornell University, 1988.

[6] B. R. Snell. Observations of magnetoquantized interface states by electron tunneling in singe-barrier n^-(InGa)As-InP-n^+(InGa)As heterostructures. *Physical Review Letters*, 59:2806–2809, 1987.

[7] E E. Vdovin. Imaging the electron wave function in self-assembled quantum dots. *Science*, 290:122–124, 2000.